國立臺灣大學工學院機械工程學系

碩士論文

Department of Mechanical Engineering

College of Engineering

National Taiwan University

Master Thesis

以內埋式光纖光柵感測器監測碳纖維複合材料衝擊及

疲勞破壞之應用

Application of Investigating the Impact and Fatigue Damage in

Carbon Fiber Composite by Using Pre-embedded Fiber Bragg

Grating Sensors

楊仕偉

Yang, Shi-Wei

指導教授：單秋成 博士

Advisor: Shin, Chow-Shing, Ph.D.

中華民國 98 年 7 月

July, 2009

國立臺灣大學碩士學位論文
口試委員會審定書

以內埋式光纖光柵感測器監測碳纖維複合材料衝擊及疲勞破壞之應用

Application of Investigating the Impact and Fatigue Damage in Carbon Fiber Composite by Using Pre-embedded Fiber Bragg Grating Sensors

本論文係楊仕偉君（　R96522520　）在國立臺灣大學機械工程學所完成之碩士學位論文，於民國98年07月15日承下列考試委員審查通過及口試及格，特此證明。

口試委員：　單秋成　　　　　　　　　（指導教授）

　　　　　　吳文方

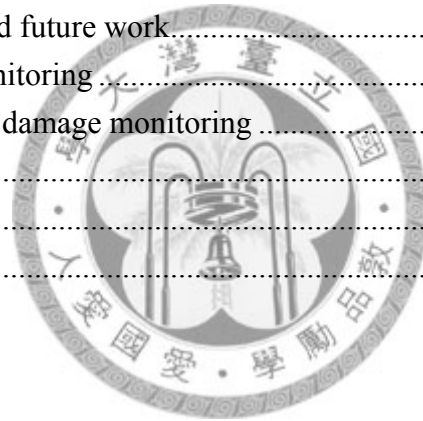　　　　　　廖顯奎

系主任、所長：

I

Acknowledgments

Abstract

Carbon Fiber Reinforced Plastic (CFRP) composites used today are at the leading edge of materials technology, with performance and fair costs to the applications. It is important to detect the impact fractures inside CFRP, preventing the structure from catastrophic failure. Due to its tiny size, Fiber Bragg Grating (FBG) sensors can be embedded inside the CFRP materials without significantly affecting its intensity. The purpose of this study was to discuss the feasibility of investigating impact damage by using pre-embedded FBGs in CFRP materials. Just after impact, the FBG sensor could detect the impact damage if it is in the vicinity of the impact source. For impact at a distance from the sensor, bending test was conducted to observe the relation between the peak wavelength shift and bending load charts to reveal any hysteresis phenomenon on the peak wavelength-bending load charts that could help us to infer the impact damage up to 50mm away from the sensors. For the post-impact fatigue test, it was found the characteristic Bragg wavelength gradually became buried in a wide band of wavelengths. In order words, the FBG lost its capability to act as a sensor. It was found that this phenomenon may be attributed to the highly non-uniform strain inside the CFRP specimen near the impact position induced by a combination of fatigue and impact damages. This revealed a previously undocumented phenomenon that may limit the application of FBG in damage monitoring inside composite material.

Key words: Fiber Bragg Grating, Carbon Fiber Reinforced Plastic, Impact damage, Post-impact fatigue damage.

Contents

List of Figure

List of Table

Chapter 1 Introduction

1.1 Background

Carbon fiber reinforced plastics (CFRP) are used in various fields such as aerospace, automotive, marine, wind power generator and the construction industry, due to their high specific strength and modulus. Many CFRP composites used today are at the leading edge of materials technology, with performance and costs appropriate to the applications. They are, however, prone to develop internal damage which is caused by bird-strike, hail-storm and cyclic loading. The damage mechanisms of a CFRP composite material subjected to impact can be classified as indentation, delamination, fiber-matrix debonding, matrix cracking and fiber breakage [22]. The interior damages may cause the structure to have a premature fatigue failure under subsequent loading. Thus, it is important to monitor the damage occurrence and development to make CFRP materials reliable and safe.

The influence of impact damage on CFRP materials has been the focus of several studies. The impact-induced delamination has been found to be important to all case of loadings [22]. The delamination inside the CFRP laminates would reduce the reliability and could be responsible for destruction of the entire structure. previous studies employed X-ray and Ultrasonic C-Scan to detect and assess the initiation and propagation of the impact damage was detected and assessed with X-ray radiography

and Ultrasonic C-Scan in previous studies [26][29]. In resent years, industrial concern has also focused on the problem of fatigue after impact damage. The progression of post-impact fatigue damage was monitored by Ultrasonic C-Scan, measurement of the changes in the coupon modulus and measurement of hysteresis in the impact damaged coupons [29]. However, these conventional methods for internal defect examination in CFRP composites cannot provide real time monitoring. To the later purpose, we try to interrogate the application of FBG for the possibility of monitoring the development of impact damage and post-impact fatigue damage.

1.2 Motivation

Fiber Bragg Grating (FBG) sensor have been used in sensor application for decades. These sensors have advantages such as small size, good sensitivity, good long-term stability, corrosion resistance and immune to magnetic and electromagnetic interferences. Due to their tiny sizes and compatibility with common polymeric materials, the FBG sensors are suitable for embedding in the fiber reinforced composite structure. By embedding the FBG sensors into composite structure, it might allow us to monitor the changes in strain distribution without deterioration of the mechanical properties. Thus, the aim of this research was to discuss the feasibility of using the embedded FBG sensors for detecting the impact damage and monitoring the development of impact damage under the cyclic loading in CFRP materials.

Several studies have reported the use of the embedded FBG sensors in various applications. One study reported used embedded FBG sensors for monitoring the development of impact-induced delamination [20]. A More recent one evaluated the impact damage by detecting the impact residual strain using FBG sensors [19]. These studies pointed out that on-line monitoring of the occurrence and development of interior defects in composite structure is an important technology for improving the safety and reliability of built-up composite structures. Hence, developing the embedded FBG sensor system to examine the interior defects in CFRP structure was the main object of this study.

1.3 Methodology

In the present study, we proposed to investigate the interior damage in CFRP structure by using the FBG sensors. The FBG sensors were embedded between laminates before curing process. The reflective spectra from the FBG sensors were measured with the Optical Spectrum Analyzer (OSA). The reflective spectrum of FBG sensor will reflect the alteration of strain field around it.

In the first part of this study, detection of the interior impact damage in carbon fiber reinforced composite plate by pre-embedded FBG sensors has been investigated. In the second part, we used the FBG sensors to monitor the development of impact damage during fatigue test. In addition, we also employed the Ultrasonic C-Scan to

help us observe the exact positions and scale of the impact damage.

1.4 Thesis layout

Chapter1: Orientation for readers of this thesis, giving them the general idea about this thesis.

Chapter2: Essentially organizing relevant references of FBG sensors and CFRP materials.

Chapter3: Introducing the experimental facilities, detailing the design of experimental set-up.

Chapter4: Presenting the results of the FBG embedded in CFRP specimen for investigating the impact damage and the development of impact damage during fatigue test.

Chapter5: Summarizing the main findings and achievements of this thesis and suggestions for possible future work.
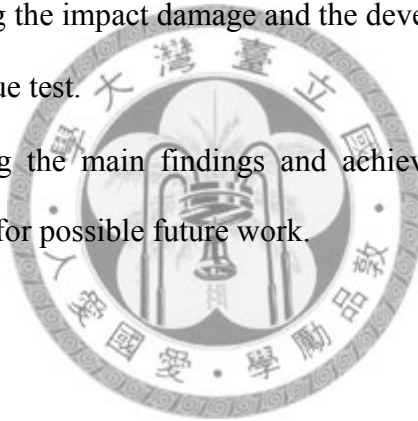
Chapter 2 Literature Review

2.1 Fiber grating sensors

2.1.1 Introduction of fiber grating sensors

The Fiber grating sensors have been widely researched in various fields of applications. Fiber grating sensors offer near-ideal advantages such as EMI immunity, high sensitivity, and multiplexing capability and so may be used in place of conventional electro-mechanical sensor systems resent years, which are well established, have proven reliability records and manufacturing costs. Their tiny size and compatibility make them able to be easily embedded in fiber reinforced composite structure without significant weakening of the material. Systems of multiplexed fiber optic Bragg grating sensors are currently used for the mechanical strain measurements.
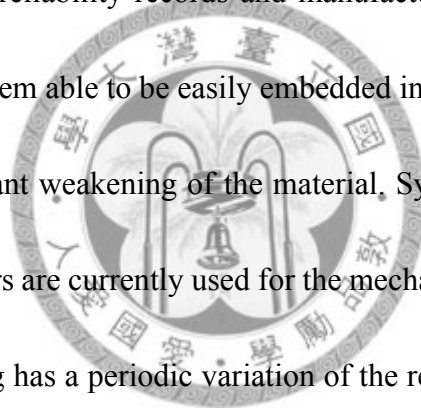
A fiber Bragg grating has a periodic variation of the refractive index [1] which is photo-inscribed by ultraviolet in a short segment along the core of fiber. This Distributed Bragg Reflector (DBR) reflects particular wavelengths of light and let others pass through the grating. The grating periodicity is small, typically on the order of 1μm. Fig. 2-1 [2] illustrates the reflected component and transmitted signal of the SM fiber Bragg Gratings when a broadband optical source encounters gratings. In this case, FBG acts a light filter which selectively reflects a particular wavelength, as known as Bragg Wavelength. The reflectivity of a strong grating can approach nearly

100% at the peak of Bragg wavelength on the refracted spectrum.

Bragg gratings in fiber optics are based on a phase-matching condition between propagating optical modes. Under this condition, interactions or disturbances for mode coupling occur due to periodic perturbation in the fiber. This condition can be represented in terms of propagation constants to a general form, which is given by:

$$\Delta\beta = \beta_1 - \beta_2 = \frac{2\pi}{\Lambda} \tag{2-6}$$

where $\Delta\beta$ is the difference in the propagation constants of two modes, β_n are the propagation constants, Λ is the spatial period of the grating. Here, for a Single-Mode fiber, β_1 and β_2 are the forward- and reverse- propagation constants with identical mode, that is to say, $\beta_1 = \beta$, $\beta_2 = -\beta$. Where β is the mode propagation constant, which is defined as:

$$\beta = \frac{2\pi}{\lambda} n_{eff} \tag{2-7}$$

where n_{eff} is the effective index of the fundamental mode, and λ is the free-space wavelength of source. Substitute it to Eq. 2-6, one can obtain:

$$\lambda_B = 2\Lambda n_{eff} \tag{2-8}$$

where λ_B is termed the Bragg wavelength. Physical quantity changes that lead to change in Λ or n_{eff}, such as strain, temperature, and vibration, will induce the changes of Bragg wavelength. The basic operation principle commonly used in FBG-based system is to monitor the changes of Bragg wavelength [3].

FBG sensor systems can be embedded into the materials to monitor the multiaxial strain and health of the structures on a real time basis [4]. These fibriform sensors are compatible with fiber reinforced composite structure. Hence, we proposed to employ the embedded FBG sensor system to detect the interior defects in this study.

2.1.2 The properties of fiber Bragg grating sensors

The spatial period of Bragg gratings will be changed by altering the geometric features of the fiber. As mentioned before, these changes can be simultaneously induced by temperature variation and uniaxial or multiaxial stresses. When the sensor is stressed or circumstantial temperature fluctuates, the grating pitch will be modified, and that change induces refractive index modulation. The sensitivity of FBG sensors with temperature and strain has to be taken into account for such applications as in bandpass filter. In the following we will discuss the relationship between Bragg wavelength shift and strain fields or temperature.

(1) Uniform strain fields

The reflective wavelength of the FBG can vary under strain fields. When the FBG sensor is under a uniform strain field, the grating period Λ of FBG changes and the Bragg wavelength λ_B shifts along center axis can be measured by differentiating and rearranging Eq. 2-8. [2]:

$$\frac{\Delta\lambda_B}{\lambda_B} = \varepsilon_Z + \frac{\Delta n_{eff}}{n_{eff}}$$ (2-9)

where $\varepsilon_Z = \Delta\Lambda / \Lambda$ is the strain in the fiber. Fig. 2-6 [2] shows the superscript x, y or z is relative to the coordinate axes of the fiber respectively. Eq. 2-9 indicates that change in refractive index also causes Bragg wavelength λ_B shifting. From the coupled-mode theory, the shift in Bragg wavelength is only influenced by the refractive changes which are normal to the fiber axis, so that is:

$$\left(\frac{\Delta\lambda_B}{\lambda_B}\right)_i = \varepsilon_Z + \left(\frac{\Delta n_{eff}}{n_{eff}}\right)_i, i = x, y$$ (2-10)

where $\left(\frac{\Delta\lambda_B}{\lambda_B}\right)_i$ represent the contribution to $\Delta\lambda_B$ from the refractive index changes in the axis which is normal to the axis of fiber core; for the above equation, it is x- or y-direction.
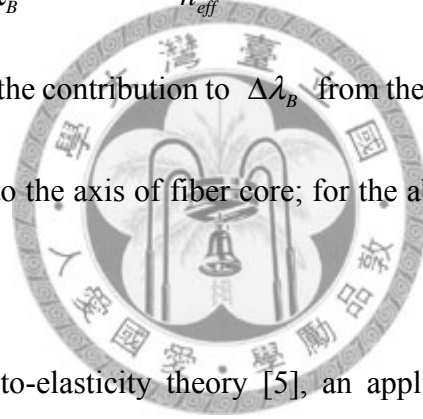
From the thermo-opto-elasticity theory [5], an applied strain and temperature result in variations in the refractive index. Assuming ideal axis symmetry, the strain component ε_j includes both mechanical and thermal strain of the fiber, which can be represented by following equation [2]:

$$\varepsilon_j = \varepsilon_j^* + \alpha\Delta T, j = x, y, z$$ (2-11)

where ε_j^* is the mechanical strain component, α is the thermal expansion coefficient of the glass fiber. Fig. 2-2 (a) shows the FBG sensor is under a uniaxial stress along its axis, then $\varepsilon_x^* = \varepsilon_y^* = -\nu\varepsilon_z^*$ (ν is the Poisson ratio of glass fiber). As a result, the

Bragg wavelength shift is related to the applied strain and temperature changes as:

$$\frac{\Delta\lambda_B}{\lambda_B} = K_\varepsilon \varepsilon^* + K_T \Delta T \tag{2-12}$$

in above equation, K_ε and K_T are the strain and temperature coefficients respectively, which can be obtained by following:

$$K_T = \frac{\xi}{n_{eff,0}} + \left[1 - \frac{n_{eff,0}^2}{2}(P_{11} + P_{12})\right]\alpha \tag{2-13}$$

$$K_\varepsilon = 1 - \frac{n_{eff,0}^2}{2}(P_{11} + P_{12})$$

where P_{11} and P_{12} are opto-elastic coefficients, ξ is the thermo-optic coefficient.

From the previous study [6], $P_{11} = 0.113$, $P_{11} = 0.252$, $n_{eff} \approx 1.458$, $\nu \approx 0.17$, $\alpha \approx 0.55 \times 10^{-6}$, $\xi \approx 8.3 \times 10^{-6}$ [7]. One can calculate that $K_T \approx 5.88 \times 10^{-6}$, $K_\varepsilon \approx 0.8$. Thus, the strain can be measured by the shift in reflective wavelength of FBGs.

Fig. 2-2 (b) shows the FBG sensor is under a general non-uniaxial stress, the original reflection spectrum from the FBG sensors splits into two peaks. This is due to the Bragg wavelength shift caused by the refractive index changes in the x- and y-directions which are not identical [8]. In practical applications, one often considers the plane strain condition so that the strains can be obtained by measuring the two wavelength shifts. By using Hooke's law, the relation between Bragg wavelength shifts and stresses can be obtained by [2]:

$$\begin{cases} (\dfrac{\Delta\lambda_B}{\lambda_B})_x \\ (\dfrac{\Delta\lambda_B}{\lambda_B})_y \end{cases} = \begin{bmatrix} K_1 & K_2 \\ K_1 & K_3 \end{bmatrix} \begin{Bmatrix} \sigma_z \\ \sigma_x \end{Bmatrix} + K_T \Delta T\{I\} \qquad (2\text{-}14)$$

where $K_1 = \dfrac{1}{E}\{1 + \dfrac{n_{eff,0}^2}{2}[\nu(P_{11}+P_{12})-P_{12}]\}$, $K_2 = \dfrac{1}{E}\{-\nu + \dfrac{n_{eff,0}^2}{2}[2\nu P_{12}-P_{11}]\}$,

$K_3 = \dfrac{1}{E}\{-\nu + \dfrac{n_{eff,0}^2}{2}[\nu(P_{11}+P_{12})-P_{12}]\}$, and $\{I\}$ is the unit matrix. From Eq. 2-14, we

can obtain transverse the stress σ_x:

$$\sigma_x = \frac{(\dfrac{\Delta\lambda_B}{\lambda_B})_x - (\dfrac{\Delta\lambda_B}{\lambda_B})_y}{K_2 - K_3} \qquad (2\text{-}15)$$

(2) Non-uniform strain fields

When a structure is subjected to impact, the damage caused by the impact often

induces non-uniform strain fields inside the structure. If the FBGs are under the

non-uniform strain fields, it causes each segment of the FBGs to have a differential shift

in wavelength. Depending on the span of each strain value over the grating length, the

reflective spectrum shows that the original wavelength peak broadens and separates

into several peaks, as Fig. 2-3 (a) shown [2]. In an extreme case, the spectrum gives a

chirp distribution if the grating is under a gradient strain field, see Fig. 2-3 (b).

Therefore, the shape of reflective spectrum depends on the strain distribution [9].

For a uniform grating, the reflectivity of a FBG R can be calculated from

following equation [10]:

$$R = \tanh^2(\kappa L) \qquad\qquad (2\text{-}16)$$

where κ is coupling coefficient, L is grating length. If the FBG is under a non-uniform strain field which varies with each different grating length, the grating length can be considered as a number of "partial-FBGs", each of them with a partial grating length, as Fig 2-4 illustrated [2]. In this situation, the peaks have different intensities due to the different lengths of strain distribution.

(3) Temperature effects

When the FBGs are applied in the measurement of mechanical parameters, such as stress, strain, curvature…etc, one must consider the issue that the sensing element is sensitive to both temperature and mechanical parameters. The temperature sensitivity of Bragg wavelength is about 10 pm/C°. Fig. 2-5 shows the relationship between Bragg wavelength and temperature. A previous study has reported that the temperature reduced shift of a fiber Bragg grating can be reduced from 10 pm/C° to below 1 pm/ C° [11].

2.1.3 Fabrication of fiber Bragg grating sensors

The first fiber Bragg grating was discovered in 1978 by Ken Hill *et al.* [12]. By exposure of the fiber to an intense optical interference pattern, they discovered a section of periodic variation in refractive index in the optical core. The fabricated techniques broadly fall into two methods: bulk interferometer and phase mask.

The bulk interferometer method for the side writing technique of FBG was first demonstrated by Meltz *et al* [13]. As Fig. 2-6 [10] shows, the UV beam divided into two at a beam splitter and then the two UV mirrors bring the two divided UV beam together at a mutual angle to the interference pattern, where the fiber is held. The interferometer is suitable for single-pulse writing of short gratings. However, a simpler component, phase mask, had been developed to fabricate FBG sensors more easily.

Another easier inscription of fiber gratings was made possible by the application of the phase mask as a component of the interferometer. A phase mask is a UV-transmitting silica plate etched grooves with a carefully controlled mark-space ratio. The gratings can be inscribed in the photosensitive fiber by exposing the fiber to UV beam through a phase mask, as Fig 2-7 [14] illustrates. Now this method has been regarded as a most common technique to fabricate FBGs.

2.2 Embedded FBG in composite materials

2.2.1 Thermal residual stress in composite materials

Due to the different thermal expansion coefficients of the graphite fiber and the epoxy, the residual stress will exist in Gr/Epoxy laminated composite. Fig. 2-8 [2] depicts the differential thermal expansion in fabrication. During the heating process, the epoxy expands but the carbon fiber contracts to different amounts. On the contrary, the epoxy contracts but the carbon fiber expands during cooling process. However,

epoxy cure and become solidify in the composite, locking the expansion/contraction together at some state. This phenomenon will induce the residual stress inside the composite structure.

Provided FBG sensors are embedded in composite laminates, it will be under a biaxial residual strain field caused by thermal residual stress, and the reflection spectrum from FBGs splits in to two distinct peaks. This is due to non-axisymmetric thermal residual stress which induces birefringence effect in the optical fiber [15]. Fig. 2-9 [16] illustrates the reflective spectra from uncoated normal FBG sensor embedded in CFRP laminates during the cure cycle. The Bragg wavelength just shifted but without significant deformation while the temperature was increasing. This is because the laminates are in a liquid state before solidification. But during the cooling process, the reflective spectra started deforming. In this stage, the laminates are solid state, and therefore the thermal residual stress appears in it. As the temperature drops from 185C° to room temperature, the form was disturbed, and finally split into two peaks.

FBGs are sensitive to non-uniform strain fields so they can be embedded in fiber reinforced composite materials to investigate the occurrence of cracks. The deformation of the spectrum induced by thermal residual stresses will lead to misreading in strain measurement. In this study, we will discuss the relation between the wavelength shifts and bending stress to infer if there are impact fractures inside the

structure of CFRP sheet.

2.2.2 Birefringence effect

The refractive index of an optical fiber depends not only on the applied UV light radiations but also on the applied perturbations. If the optical fiber is subject to a perturbation or disturbance such as stress or strain, temperature change, bending or micro-bending, a linear birefringence will be induced due to the geometrical modifications and or the anisotropy of the material of the fiber [17]. As a result of applied transverse load, the deformation of the dielectric waveguide will induce refractive index changes of the FBG by consequence a birefringence. The refractive index changes induced by applied load are called photoelastic phenomena. By the photoelasticity theory [5], the effective refractive index changes of the FBG can be derived as following:

$$\Delta\left(n_{eff}\right)_x = -\frac{(n_{eff,0})^3}{2E}\left\{(P_{11}-2\nu P_{12})\sigma_x + \left[(1-\nu)P_{12}-P_{11}\right]\left[\sigma_y+\sigma_z\right]\right\}$$

$$\Delta\left(n_{eff}\right)_y = -\frac{(n_{eff,0})^3}{2E}\left\{(P_{11}-2\nu P_{12})\sigma_y + \left[(1-\nu)P_{12}-P_{11}\right]\left[\sigma_x+\sigma_z\right]\right\}$$

(2-17)

where E is the Young's modulus of the optical fiber; σ_x, σ_y, and σ_z are the stress components in FBG in the x, y, z principle directions, respectively. The induced or accidental birefringence effect results in two different propagation constants for x-polarized and y-polarized guided modes. As these modes propagate, they will be coupling in or out of the fiber and energy exchange between the modes. In FBG sensors,

14

the birefringence induces bifurcation or a split of the peak at Bragg wavelength, and that is a disadvantage in most sensing applications.

2.2.3 Sensitivity of embedded FBG sensors

To reduce the birefringence effect caused by thermal residual stress, several researchers have studied the development of embedded FBG sensor systems. One previous study has focused on comparison between three types of FBG sensors: uncoated normal, polyimide-coated normal, and polyimide-coated small-diameter FBG sensors embedded in CFRP cross-ply laminates [16]. The results found that using small diameter polyimide coated optical fiber is beneficial to decreasing the thermal residual stress on the reflection spectrum. Further, the influence of coating and grating length in FBG sensors embedded in composites was addressed. Fig. 2-10 [18] illustrates the FBGs responses compared with traditional electrical strain gages along the tensile test and flexural test. The results showed the longer uncoated sensors had higher sensitivity to the strain, but the strain value measured by FBG sensors were lower than that measured by strain gages for all case.
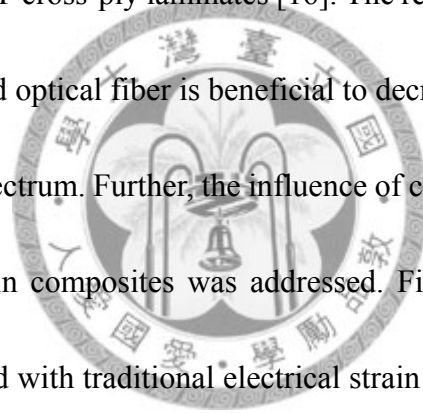
2.2.4 Damage monitoring by embedded FBG sensors in composite materials

Several researchers have studied the monitoring impact damage by embedded FBG sensors in composite materials. Chambers reported that if the FBG sensors were

located within a distance of 2~3 times of the damage radius can detect the strain

disturbance caused by the impact [19]. If an array of closely spaced sensors was

employed, it should be possible to locate the impact site, predict the maximum impact

energy and hence predict the area of damage.

Takeda examined the impact-induced delamination in CFRP laminates using

small-diameter FBG sensors [20]. He used FBG sensors to detect the effect caused by

a delamination as monotonic tension loading was applied. The change in reflection

spectra from the FBG sensor depends on the delamination size. When the form of the

spectrum was mainly characterized by two peaks, the intensities of the two peaks

could be good indicator of delamination size. The delamination length was evaluated

through the intensity ratio of the two peaks in the spectrum, as Fig 2-11 shows [20].

From the relationship between the delamination size and form of the spectrum, it

could effectively predict the delamination length in composite structure.
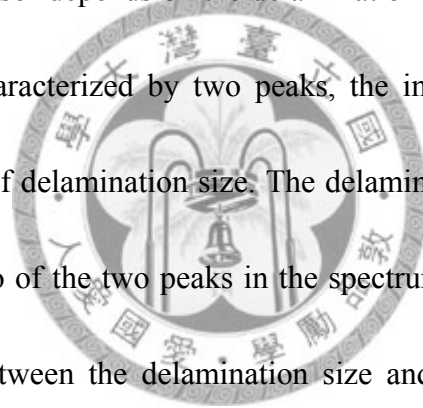
2.3 Impact and Fatigue damage in composite
materials

2.3.1 Impact damage in composite materials

Most composite materials are brittle and very susceptible to serious impact

damage. The basic impact failure modes of composite materials include: (a) matrix

cracking, (b) fiber breakage and fiber pull-out, (c) fiber-matrix interface debonding, and (d) delamination, as Fig. 2-12 [21] illustrated. As a composite material is subjected to subperforation impact, it could cause failure mechanisms such as surface indentation, fiber breakage, matrix cracking, fiber-matrix debonding and delamination simultaneously. Among these damage modes, delamination has been found to have important influence for all cases of loading [22], and it can cause premature failure under subsequent loading [23].

2.3.2 Fatigue damage in composite materials

Many composite structures are subjected to cyclic loading during their normal life expectancy. This can induce the propagation and development of insidious defects in the composite structure and eventually lead to destructive failures. The primary failure modes caused by fatigue testing include: matrix cracking, fiber splitting and breakage and delamination. The schematic diagram of fatigue damage is shown in Fig. 2-13 [21]. There has been some study on the effect of the fatigue after impact. Impact damage can decrease the fatigue strength [26] and damage grows inconsistently under cyclic loading [25] and it has been shown that. The fatigue damage analysis is usually empirical. The propagation of the damage can be assessed with X-Ray, Ultrasonic C-Scan and similar NDT techniques. In this work, the post-impact fatigue damage development will be assessed by using the pre-embedded FBG sensors.
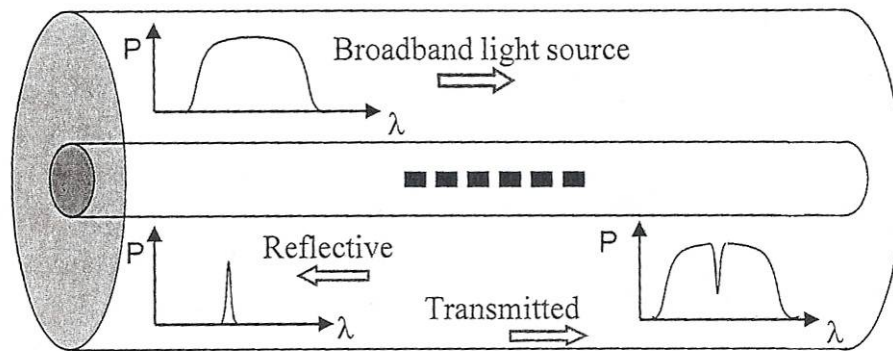
Fig. 2-1: Reflective and transmitted spectra of the Single-mode fiber Bragg gratings [2]
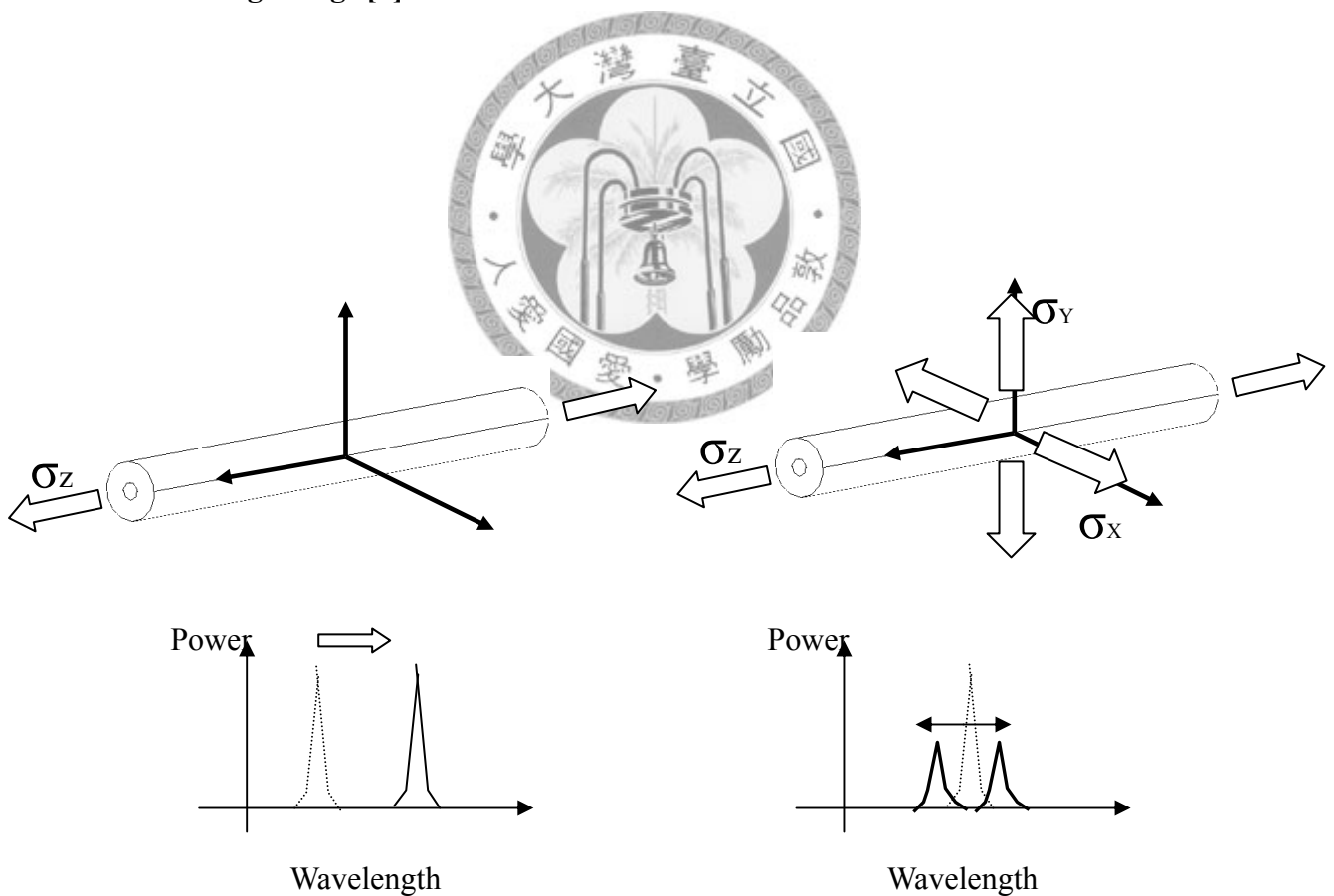
Fig. 2-2: (a) The fiber Bragg grating sensor is under a uniaxial stress, and (b) a general non-uniaxial stress. [2]
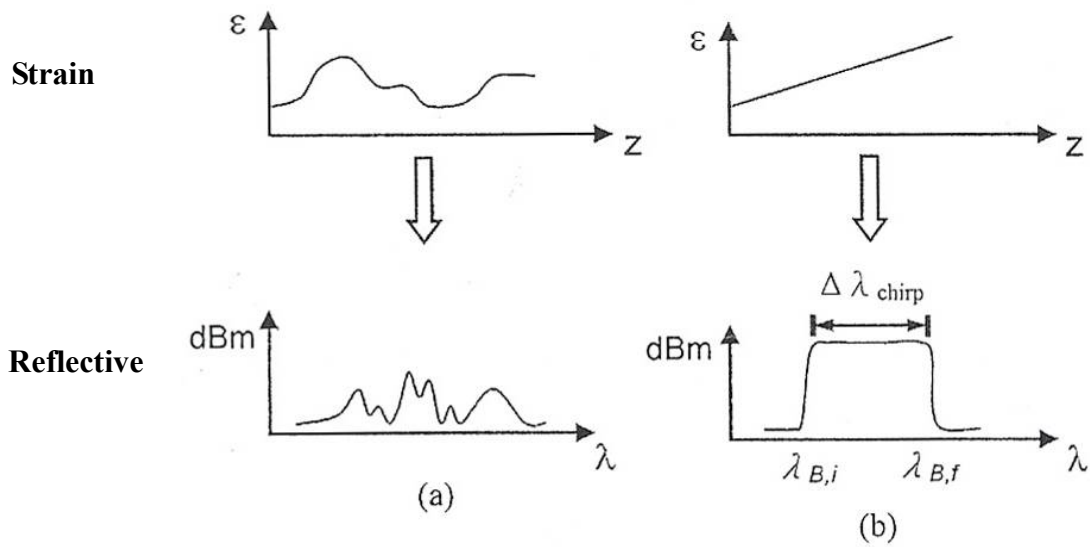
Strain

Reflective

Fig. 2-3: Reflective spectra of FBGs under non-uniform strain fields [2]
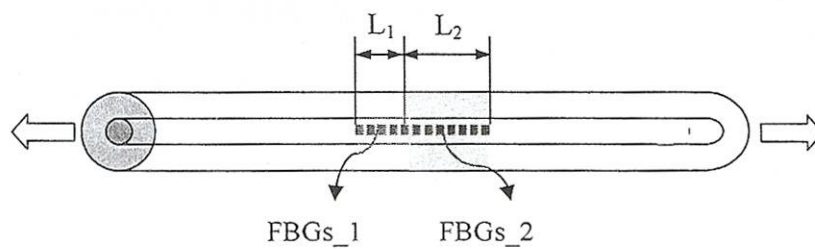
L1 and L2 are subjected under different piecewise-uniform strains

Reflective spectrum
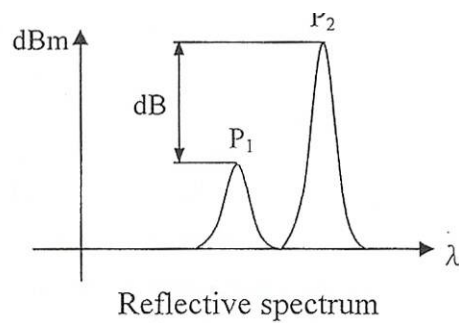
Fig. 2-4: A simple situation where the strain distribution is piecewise-uniform over the lengths L1 and L2 of the FBG sensors. [2]
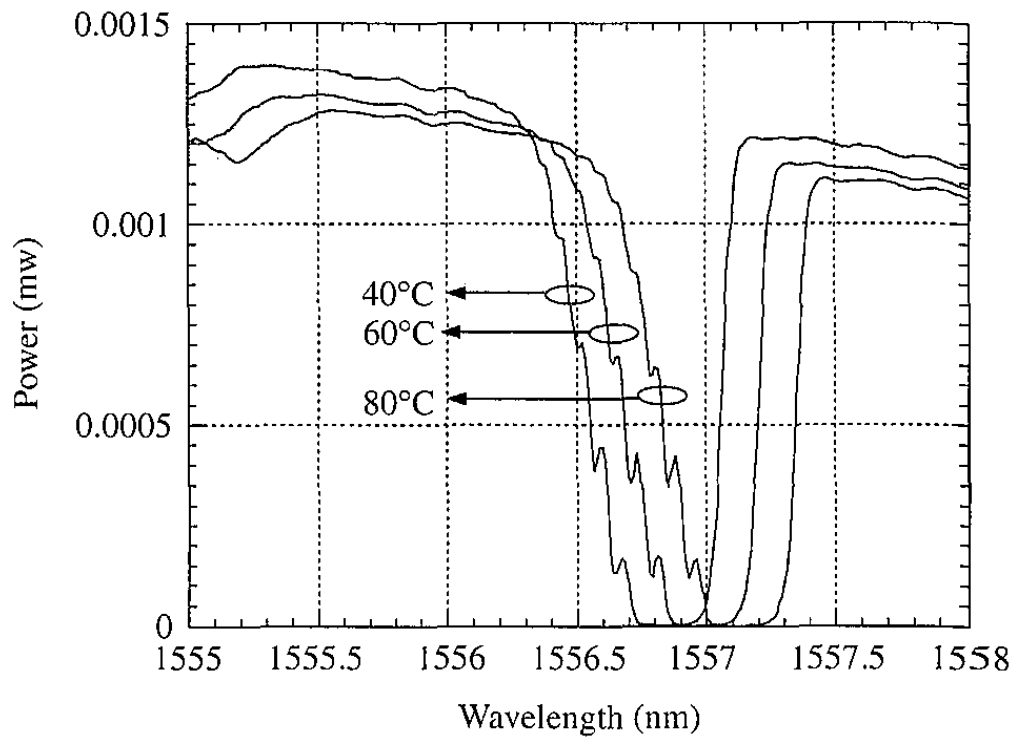
Fig. 2-5: Temperature variation induced Bragg wavelength shift [11]
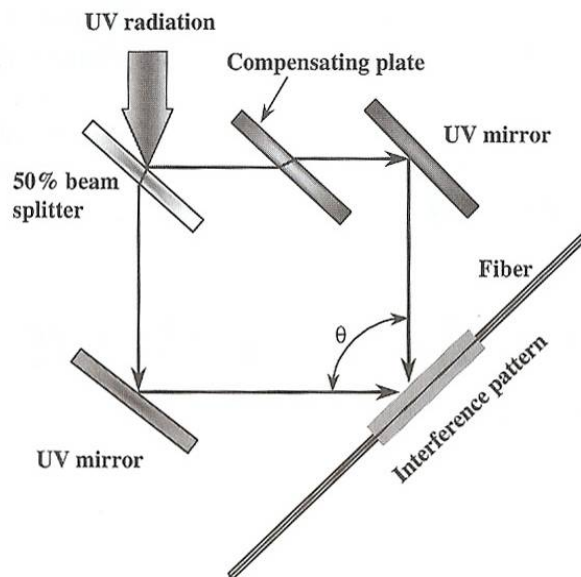
Fig. 2-6: Bulk interferometer method: UV interferometer for writing Bragg Gratings in optical fibers. [10]
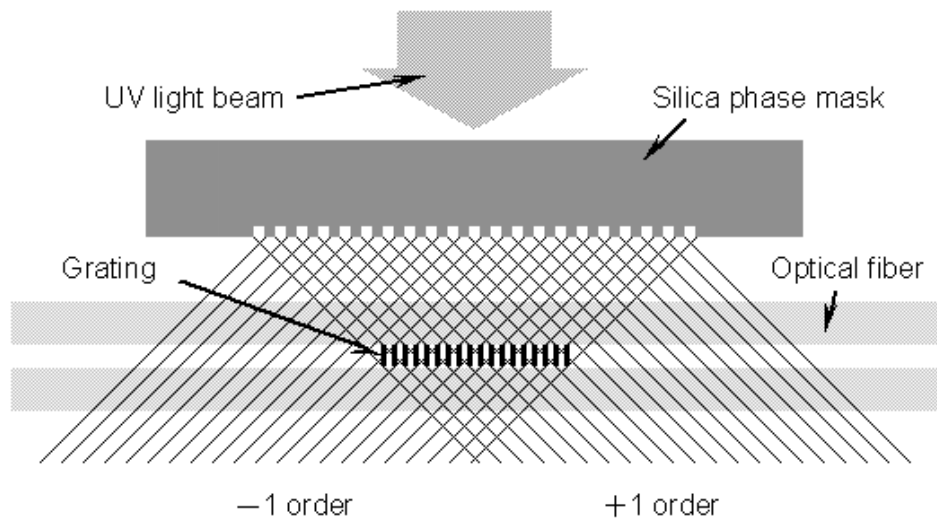
Fig. 2-7: Phase mask method to fabricate FBG [14]
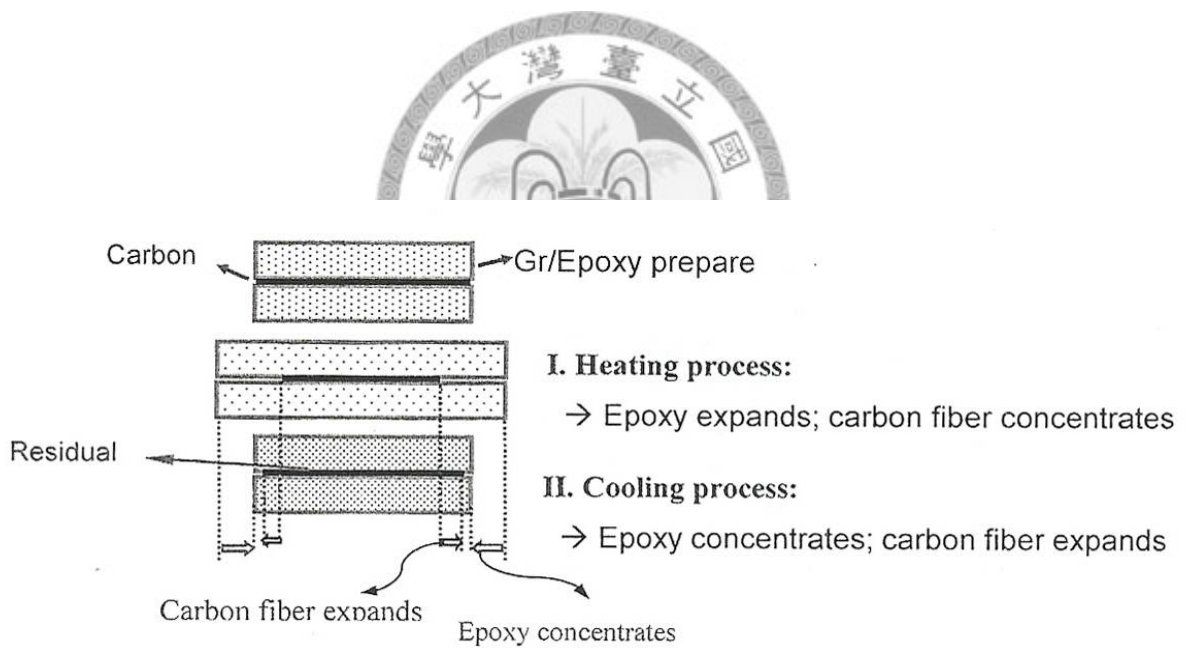
Fig. 2-8: Scheme for the explanation to the residual stress of composite manufacture [2]
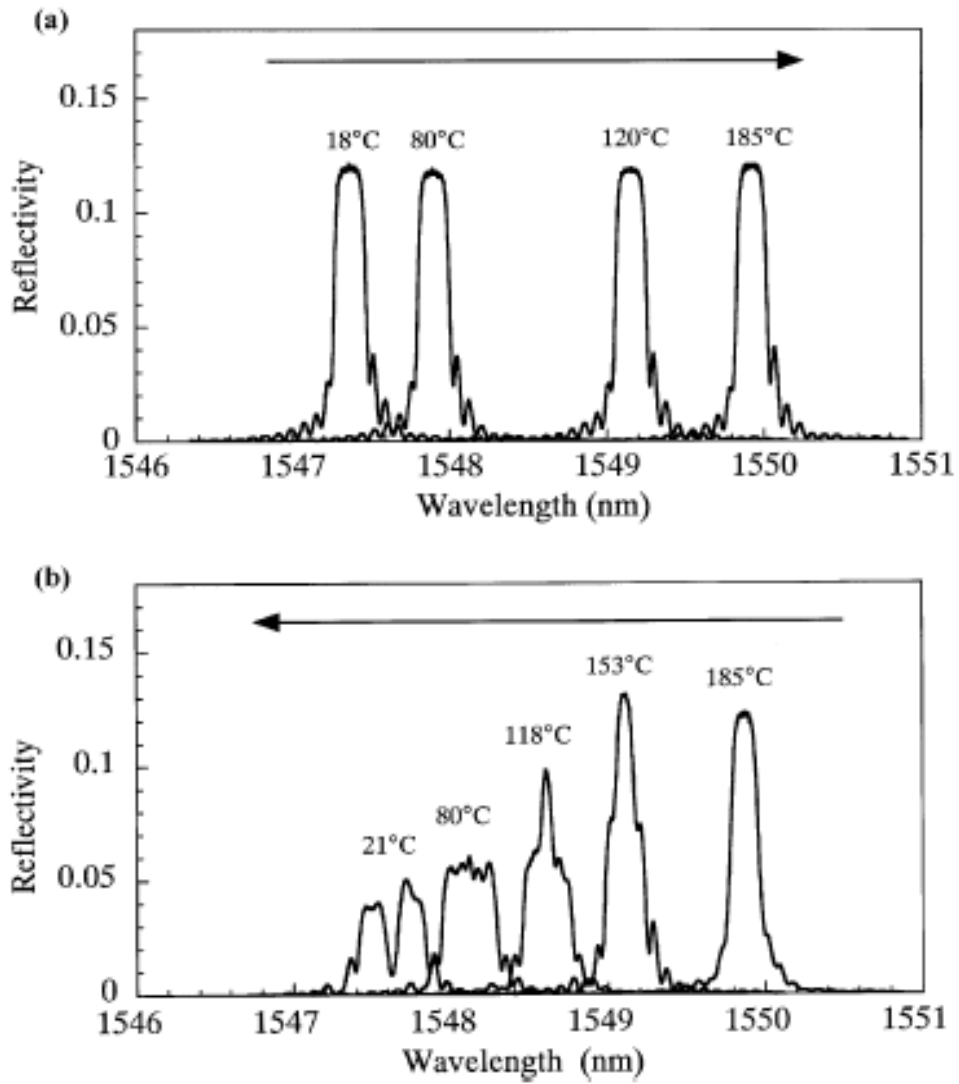
Fig. 2-9: Reflection spectra from the uncoated normal FBG sensor, which was embedded into the CFRP laminate, measured during the cure cycle (a) heating process (b) cooling process [16]
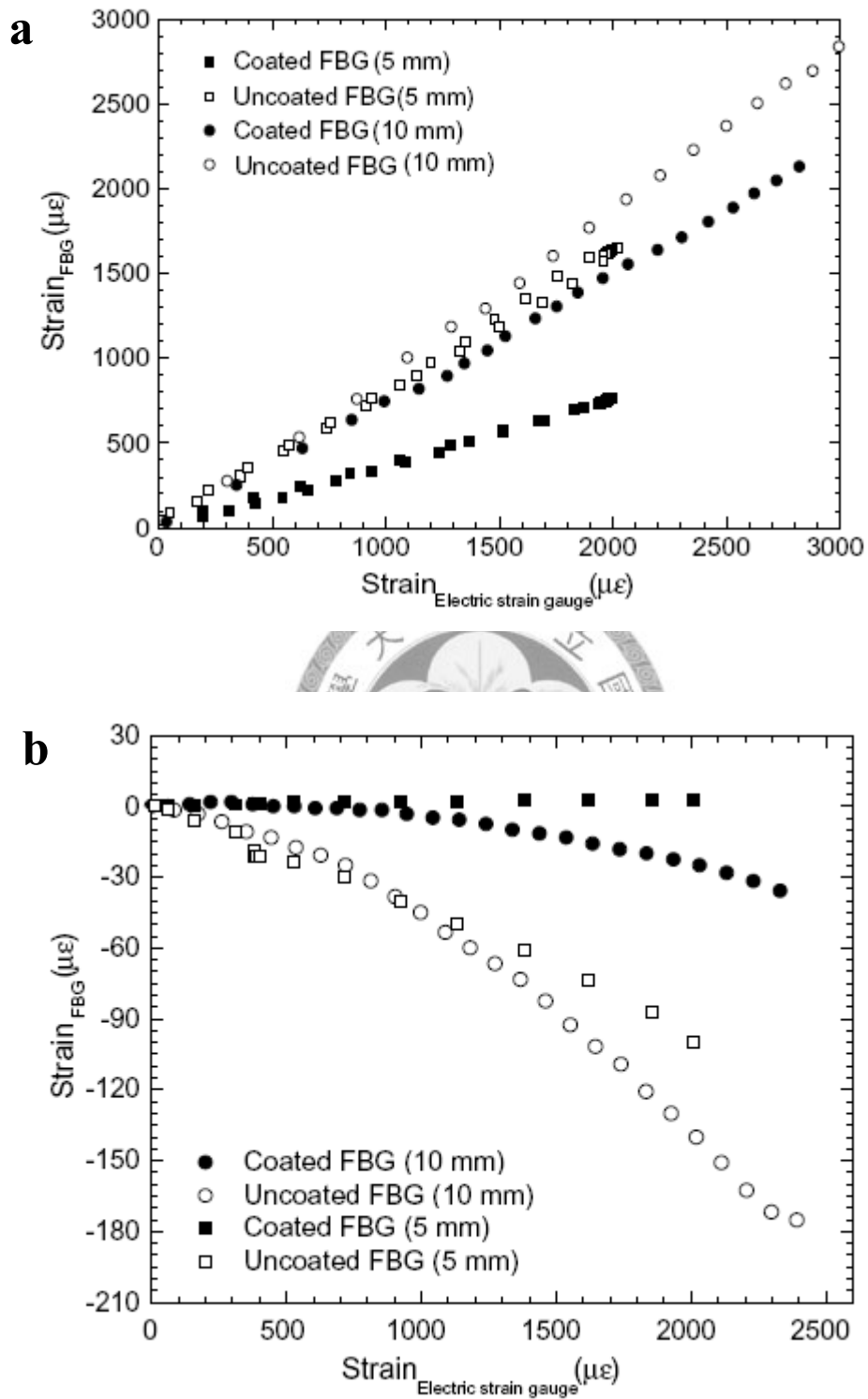
Fig. 2-10: FBG response along mechanical test: (a) tensile test (b) flexural test [18]
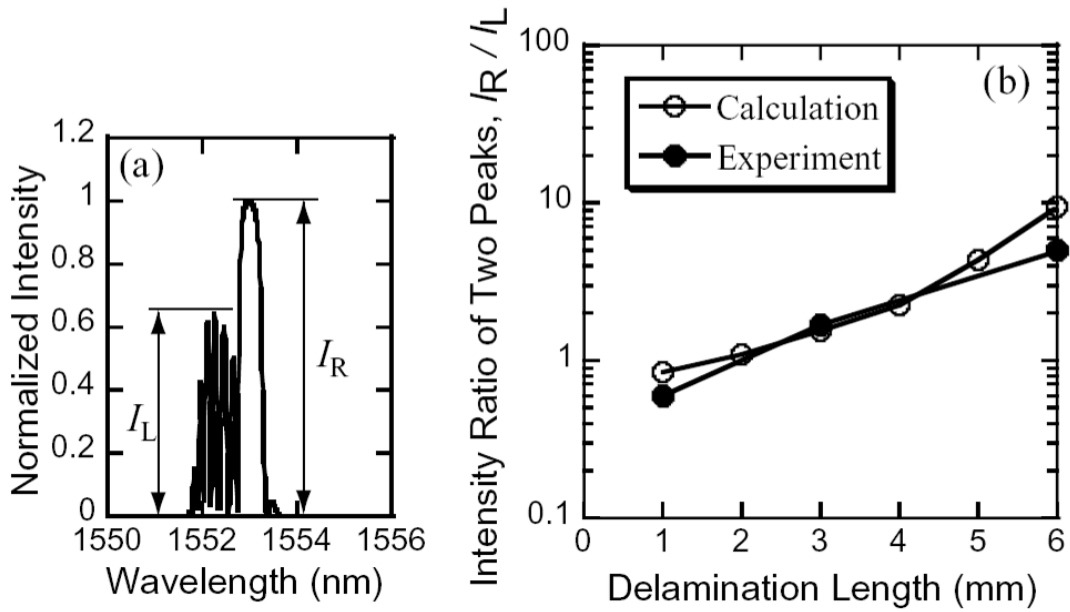
Fig. 2-11: Evaluation of delamination size. (a) Definition of intensities for two peaks and (b) logarithmic curves of intensity ratio against delamination size [20]

(a)   (b)   (c)

(d)
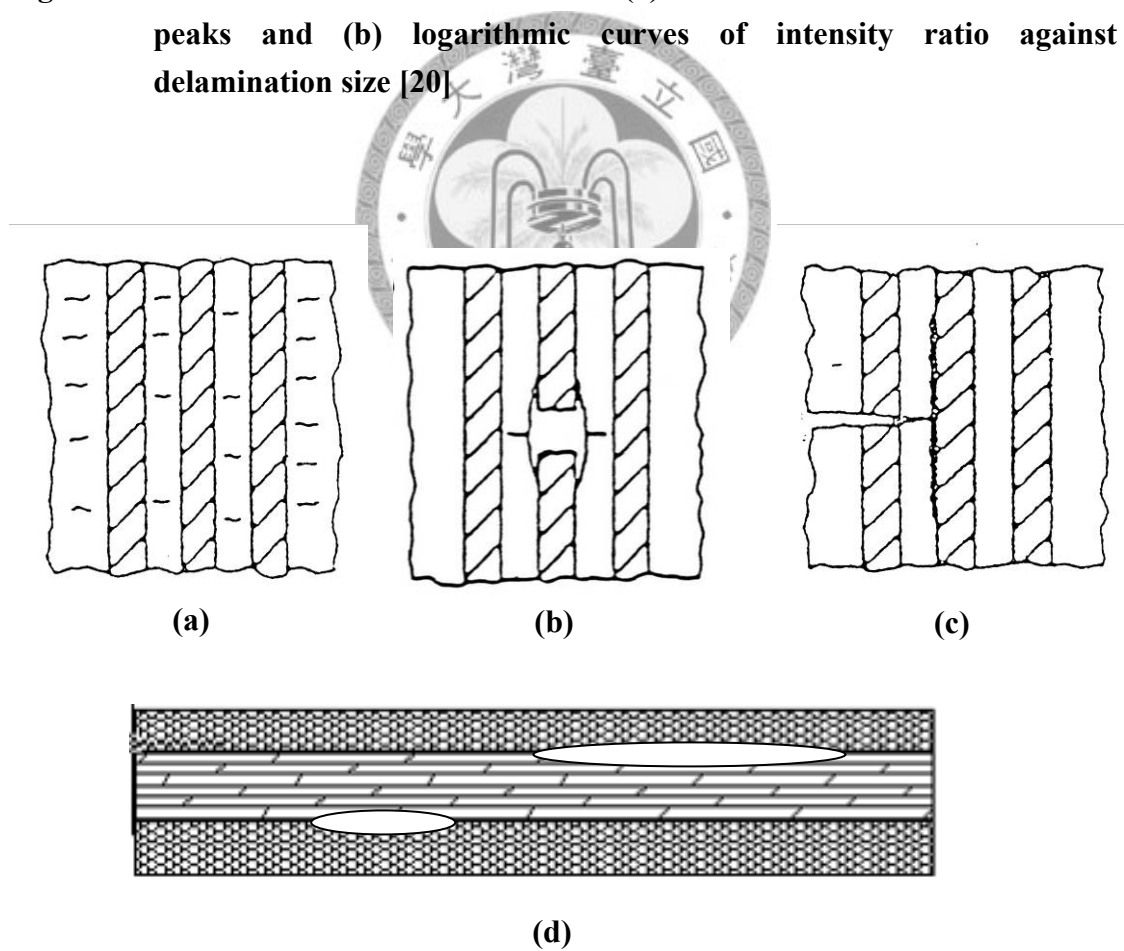
Fig. 2-12: Schematic failure mechanisms for fiber reinforced composites: (a) matrix cracking (b) fiber breakage (c) fiber/matrix interface debonding (d) delamination [21]
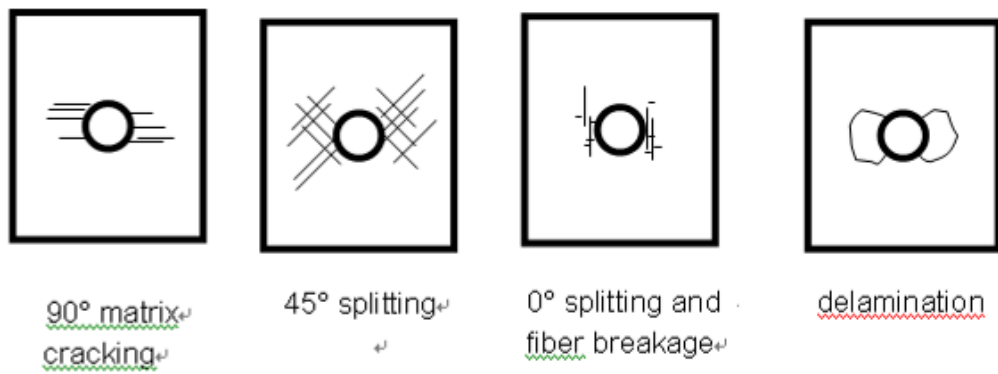
Fig. 2-13: Schematic fatigue damage modes of quasi-isotropic composite laminate [21]

Chapter 3 Experimental instruments and methodology

3.1 Experimental instruments

(1) Optical spectrum analyzer (see Fig. 3-1)

The reflective spectra of the FBG sensors were measured with an Optical Spectrum Analyzer (OSA). The spectral profile is graphically displayed on monitor, with wavelength on the horizontal axis and energy intensity on the vertical axis. The OSA, model MS9710C, manufactured by Anritsu Company Inc., was used in this study to receive a particular wavelength range from 600nm to 1750nm.

(2)MTS 810 material testing system (see Fig. 3-2)

An MTS 810 servo-hydraulic material test system is employed to apply the mechanical loading, for tensile test and fatigue test. The MTS 810 test system used in this study includes: load cell, hydraulic power supply system, and electronic control system. The load control mode to set the loading output or stroke control mode to adjust displacement speed will depend on specific testing requirements. In this thesis, the post-impact fatigue testing and tensile test were carried out on the MTS 810 test system, which was manufactured by MTS systems Corporation.

(3)Impact testing machine [26] (see Fig 3-3)

Impact testing was carried out using a home made drop weight testing machine.

By adjusting the dropping height, different impact energies could be achieved. Fig. 3-4 depicts the configuration of the simple impact testing machine used in this study. The specimen clamp used in impact test and the specimen clamp used in post-impact fatigue test were designed following ASTM-D3029 and ASTM-D5628-07 standards, respectively. Two falling darts were used accordingly. One of the falling darts made of iron with a weight of approximately 260g, was employed in post-impact fatigue test. The other one made of aluminum with a weight of approximately 90g, which was employed in the impact test (shown in Fig 3-5). The clamp for impact test has a larger inside diameter allowing more flexibility for the specimen, which in a heavier dart is needed to produce the designed damage. The drop heights selected in this study were 80cm and 140cm. Table 3.1 shows the impact energies which depended on falling height and dart mass.
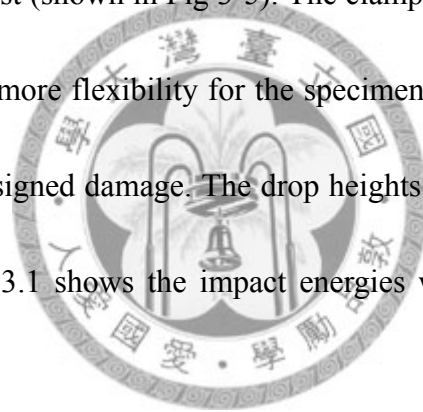
(4) Four-points bending instrument (see Fig. 3-6)

In order to find out more about the influence caused by impact damage on the CFRP plate, we applied a four-points bending to test specimen. The configuration of the four-points bending instrument used in this study is shown in Fig. 3-6. Bending load was applied by adding load weights on the upper platen of the bending instrument. The bending stress shifted the wavelength of the FBG sensors. Such shifts in wavelength against the applied load could reveal the stiffness changes associated with

impact-induced damage inside the CFRP specimens.

(5) Broadband light source (see Fig. 3-7)

To obtain strong light signals, a broadband light source with high power intensity is required. The broadband light source, model HP 83437A, used in this study was manufactured by Hewlett-Packard Company. The broadband light source was based on Edge-emitting LED (EELED) and could provide a stable light source with a wavelength in the 1550nm region. Moreover, it provided a high power density of more then -33dBm. The external modulation allowed the use of lock-in amplifiers for high sensitivity measurement. The Power stability was ±0.02 dB at the wavelength of 1550nm.

(6) Abrasive diamond-coated wheel cutting machine (see Fig. 3-8)

The specimens were cut from the CFRP plate into needed size to undergo post-impact fatigue test through an abrasive diamond-coated wheel cutting machine. The rotational speed of the abrasive-wheel for cutting the plate was approximately 4500RPM. In the process of cutting the CFRP plate, water was used as the cooling liquid to reduce the temperature of the specimen. The abrasive-wheel cutting machine used in this study was manufactured by KENT Industry Co.

(7) Hot press molding system (see Fig. 3-9)

The CFRP specimens were cured under the high pressure, high temperature and

vacuum conditions in this study. In order to fabricate the test specimens, we used a hot

press molding system which including: hot press molding machine, air compressor and

vacuum pump, to cure CFRP plate. The hot press molding machine comprised of a

matched metal tool and an electrical controller. The matched tool was placed between

the platens of a hydraulic press, which was heated to the forming temperature by the

electrical controller. The pressure in the sealed chamber was supplied by the air

compressor, whereas vacuum pump was used to remove the gas from the sealed

pressure chamber.

(8)Ultrasonic imaging system (see Fig. 3-10)

Ultrasonic C-scan technique features the production of a color image displaying a

contoured map of the internal surface condition. Basically, ultrasonic C-scans are

processed in water tank to ensure good coupling between the transducers and the tested

samples. When scanning a structure, the piezoelctric transducers or probes inject

acoustic waves, and can also receive reflective waves. Therefore, the probes act both as

the sender and receiver, as illustrated in Fig. 3-11 [21]. For this reason, we utilized the

Ultrasonic C-scan to examine the impact-induced defects. The Ultrasonic imaging

system used in this study was manufactured by Keiyu NDT Supply CO.

(9)Fusion splicer (see Fig. 3-12)

In order to joint the fiber optic patch cord and FBG sensor together, we used the

29

fusion splicer. The fusion splicer consists of two fixtures on which the fibers are

mounted, two electrodes, and an inspection microscope. The principle of fusion

splicing is to use localized heat for melting or fusing the ends of two optical fibers

together. The heat source is usually an electric arc. After the process of fusion splicing,

a tensile proof test of 5 kN force is performed to ensure that the splice is strong enough

to survive from handling, packaging and extended use. The fusion splicer used in this

study featured a heat-shrink oven which was utilized to further protect the splice area

using a heat shrink tube. The attenuation of optical fibers due to the fusion splicing is

typically less than 0.03dB. The fusion splicer used in this study was manufactured by

Fitel, Furukawa Electric Co., Ltd and the model was S199.
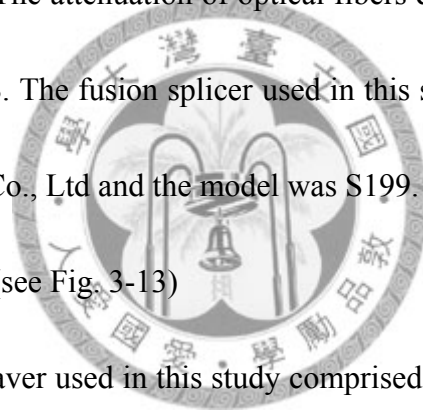
(10)Optical fiber cleaver (see Fig. 3-13)

The optical fiber cleaver used in this study comprised a 10-posion blade and was

capable of cutting the bare optical fiber into a good end face. The quality of the bare

fiber end-face would determine the quality of the joint of the fibers during the fiber

optic fusion process, and the joint point quality would influence attenuation of the fiber

connection line. The optical fiber cleaver used in this study was manufactured by Fitel,

Furukawa Electric Co., Ltd and the model was S324.

(11)Optical fiber coupler (see Fig. 3-14)

The optical fiber coupler used in this study included one input and two output

ports. The input port was connected with a broadband light source, and the other two

ports were connected with FBG sensor and OSA respectively. As a result, we could

obtain the reflective spectra from FBG sensors with OSA. The connectors of the optical

fiber couplers used in this study were of FC/PC type.

3.2 Experimental procedure of impact test

3.2.1 Fabrication of fiber Bragg grating sensors

In this study, we used the phase mask method to fabricate the FBG sensors. The

FBG sensors were fabricated with the Ge-B co-doped single cladding photosensitive,

which was produced by Fibercore Co. Ltd and the mode was PS1250.

The 248nm UV radiation from a KrF excimer laser employed contained impulse

frequency in 3Hz during the manufacturing process. The laser power should be less

than 500mJ/cm² to prevent the phase mask from burning. By exposing the

photosensitive fiber to UV beam through the phase mask, which was manufactured by

Lasiris Co. Ltd., the Bragg grating could be inscribed on the fiber. The FBG sensors

used in this study contained a periodic refractive index modulation with a period of

1.05~1.08μm and a reflective peak of Bragg wavelength at 1550nm. The total length of

the Bragg gratings was 15mm while the reflectivity of the resulting FBG was about

98~99% and the Full Width Half Maximum (FWHM) of the FBG was about 0.175nm.

3.2.2 Preparation of CFRP plate specimens

The CFRP test specimens used in this study were produced using 8 layer of quasi-isotropic T300/3501 Graphite Epoxy prepreg fabrics, which were laid up in the stacking sequences [0/45/90/-45]2S. The individual layers consisted of high-modulus, high-strength fibers in epoxy material. Before stacking up, the prepreg fabrics were precut into 200mm × 200mm sheets. Each prepreg fabric had nominally 61% by volume of graphite fiber, and the thickness was 125μm. The stack was cured at 140°C under 140psi pressure for 30 minutes in a diaphragm-type forming mold, as shown in Fig. 3-15 [27]. Fig. 3-16 [27] illustrates the forming conditions to cure the CFRP plate specimens. During the curing process, the Teflon sheets were put both above and below the stack to allow easy de-molding. The dimensions of resulting nominal CFRP plate specimen for impact test were 0.5mm × 200mm × 200mm.
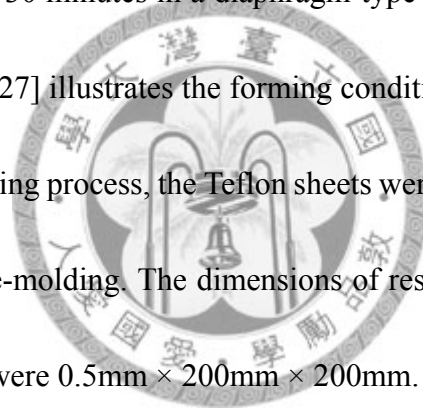
3.2.3 Embedding FBG sensors in specimens for impact test

The impact test was carried out on an 8 layer [0/45/90/-45]2S quasi-isotropic CFRP laminates plate specimen where the four FBG sensors were embedded in. In a previous study, the impact damages in different layer were different [26]. In order to fully detect the impact damage, FBG sensors were embedded in interfaces between laminates parallel to the adjacent reinforcing carbon fibers. The interfaces between laminates were designated as Layer 1 (L1), Layer 2 (L2), Layer 3 (L3) and Layer 4 (L4),

as Fig. 3-17 illustrated. The two FBGs embedded in L1 and L4 oriented at 0° and were

parallel but separated with each other by 6mm. The same is also true for the two

embedded in L2 and L3 (Fig. 3-18). All the FBG sensors in each layer were located in

the center of the plate specimen, and the fibers pierced through the plate to reach

outside, at 30mm away from the edge of the plate.

3.2.4 Experimental procedure for impact test

The purpose of the impact test was to investigate possibility of using FBG to

monitor impact-induced damage in the CFRP composite structure. Fig. 3-19 indicates

the procedures for impact test in this study. Impact damages were produced at specific

drop heights H (80cm and 140cm) on the CFRP plate specimen. The points of impact

were arranged as shown in Fig. 3-20, in order to find to find out the sensitivity of

measurement region for FBG sensors. A combination of three different distances R

(0mm, 30mm, and 50mm) and three different angular positions (A0, A45, and A90)

were employed. For impact distance R=0mm, each specimen was applied only one

impact on the center, the drop heights were 80cm and 140cm respectively. For impact

distance R=30mm and drop height H=80cm, the impacts were applied at A0 first, then

A45, finally A90 in one specimen, and we recorded the reflective spectrum as each

impact was completed. For impact distance R=30mm and drop height H=140cm, the

spectra was recorded after all the impacts were completed at A0, A45, and A90, in

sequence. The same is also true for impact distance R=50mm. The spectra were

recorded as each impact was completed under R=50mm and H=80cm, and were

recoded after all impacts completed under R=50mm and H=140cm. To compare with

the spectra between before and after impact, we recorded the reflective spectra in each

specimen before impact. The combination of drop height H and impact distance R are

detailed in Table 3.2.

To assess the effect of impact damage, four-points bending load applied to the

plate before and after each impact. The scheme of bending test setup is shown in Fig.

3-21. When a broadband light was transmitted towards the FBG, a specific narrow band

spectrum would be reflected by the Bragg gratings and was measured with the OSA. A

latching optical switch, which can be actuated by a DC voltage 5v, was used to choose

to connect one of the two parallel optical fibers in specimen plate into the measurement

path. As a result, we avoided the birefringence effect induced by macrobending on the

fiber. Moreover, a thermo coupler was located next to the specimen to record the

instantaneous temperature, avoiding the influence caused by environmental

temperature. Since the FBG sensors were embedded in different orientations, the

bending test was conducted in different directions, to produce axial bending stress in

the respective direction, as shown in Fig. 3-22.

By analyzing the changes of reflective spectra from the FBG sensors such as the

shifts in Bragg wavelength, the attenuation of the power intensity, and deformations of the waveform, we could infer the occurrence of impact damage induced inside the CFRP structure.

In addition, we also used the Ultrasonic C-scan to assess the delamination damage inside the CFRP test plate, regarding the sizes and location of the damage zones. The specimens were scanned before impact and after impact on those three designated positions. Consequently, the impact damage could be assessed by the results obtained from FBG sensors and Ultrasonic C-Scan.

3.3 Experimental procedure of post-impact fatigue test

3.3.1 Preparation of specimens for post-impact fatigue test

The specimens used in post-impact test were also laid up in the stacking sequences [0/45/90/-45]2s. Unlike the plate-shape specimens specifically for impact test, the test specimens were cut into bar-shape from the CFRP plate with abrasive diamond-coated wheel cutting machine. The cutting direction was along the reinforced fiber orientation of the 0° laminates enabled the optical fiber sensors to be placed in L1 and L4. As mentioned earlier, the water was used as cooling liquid during the cutting process, therefore we needed to put the specimens into a desiccator for more than one day before test. The nominal dimension of the post-impact fatigue specimen is 0.5mm × 200mm ×

25.4mm.

3.3.2 Embedding FBG sensors in specimens for post-impact

fatigue test

Due to the geometric restriction in the post-impact fatigue specimen, the FBG

sensors could only be embedded in L1 and L4. Fig. 3-23 illustrates the location where

the FBG sensors were installed. The distance between two FBG sensors was 6mm.   To

avoid the optical fibers being clamped by the grips during fatigue test, they were

surfaced at 50mm away from the center of specimen.

3.3.3 Experimental procedure for post-impact fatigue test

The procedure and setup in post-impact fatigue test were shown in Fig. 3-24 and

Fig. 3-25, respectively. First of all, the specimen would be impacted at a drop height of

80cm or 140cm. The 260g iron falling dart used in this test and the impact positions was

designated A, B, and C, as shown in Fig. 3-26. Position B was at the center of the

specimen (the location where FBGs were embedded), while positions A and C were

respectively in the upstream and downstream of the gratings based on the route of the

light propagation. When the light was routed through the gratings, it would reach

position A first, via the gratings through to position C.

After impact, the specimen was cyclically loaded with 0.5kN~5kN at a frequency

of 5Hz. The two FBG sensors embedded in L1 and L4 were also connected to a

selectable switch to display the designed reflective spectra on the OSA. During the

fatigue test, we used a thermocouple to monitor the temperature in order to reduce the

influence of temperature fluctuation. Besides, in order to confirm the development of

impact-induced damage during fatigue test, Ultrasonic C-scan was also employed to

detect the impact damage before and after the fatigue test.

Fig. 3-1: Optical spectrum analyzer (MS9710C)

Fig. 3-2: MTS 810 material testing system

Fig. 3-3: Impact test machine

Falling Dart

Drop Tube

Drop Height H

Clamp

Test Specimen
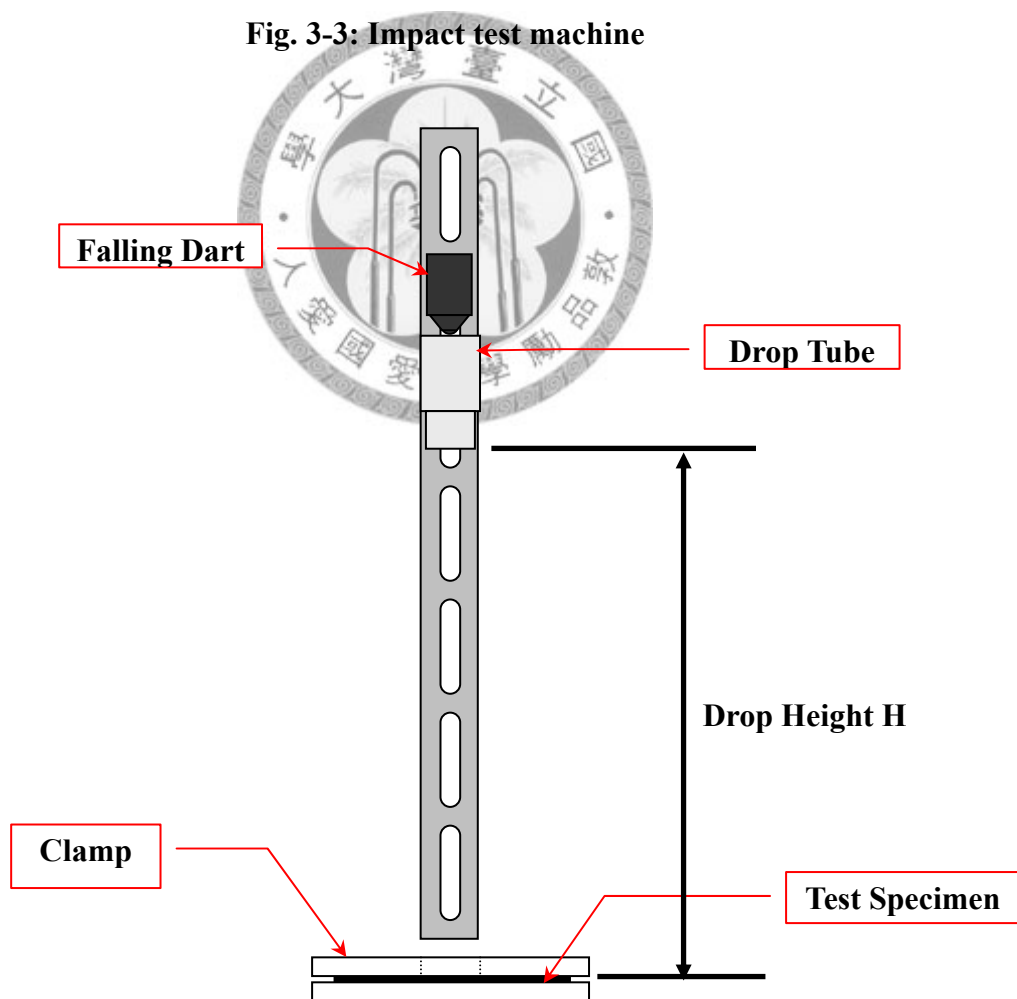
Fig. 3-4: Configuration of the impact test machine [26]
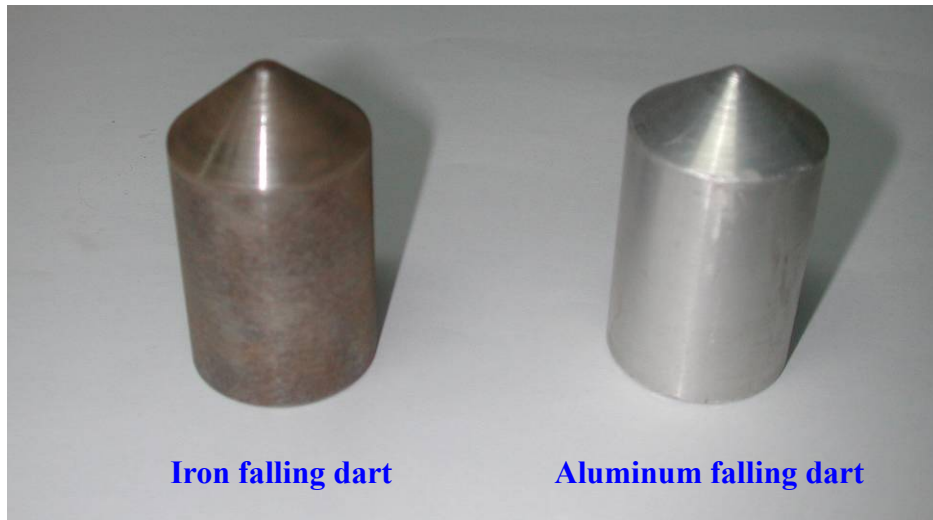
Fig. 3-5: Iron falling dart (Left) used in impact test and Aluminum falling dart (Right) used in post-impact fatigue test
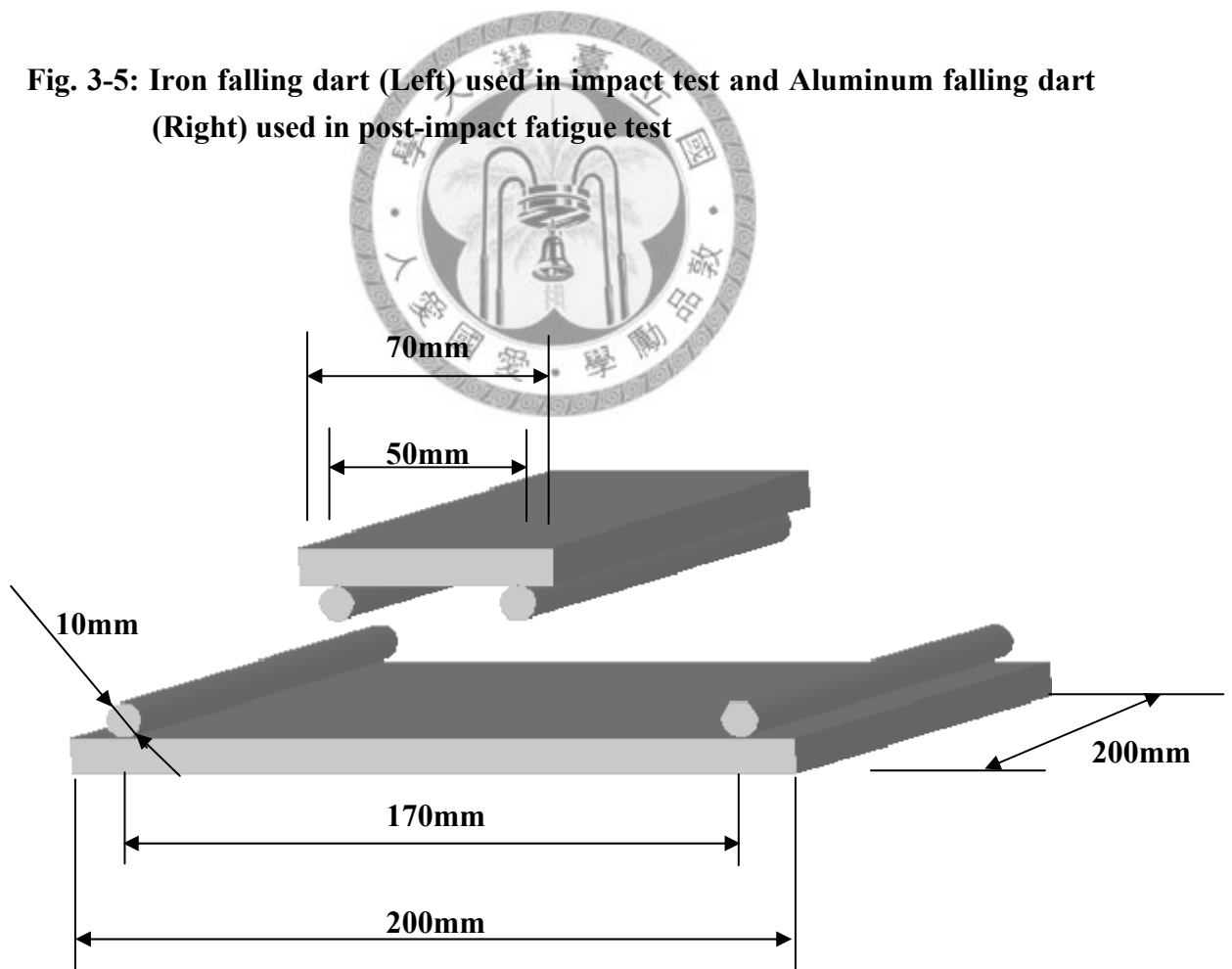
Fig. 3-6: Configuration of the four-points bending instrument
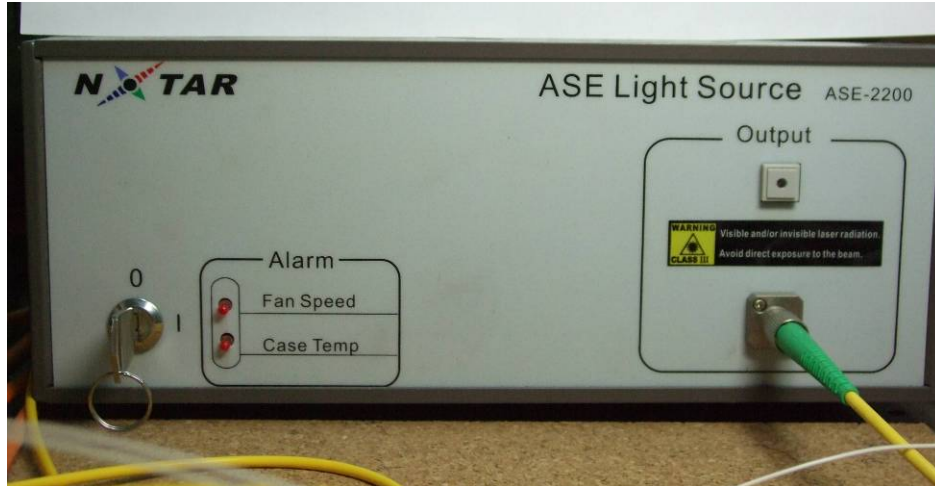
Fig. 3-7: Broadband light source

Fig. 3-8: Abrasive diamond-coated wheel cutting machine

Fig. 3-9: Hot press molding system

Fig. 3-10: Ultrasonic imaging system
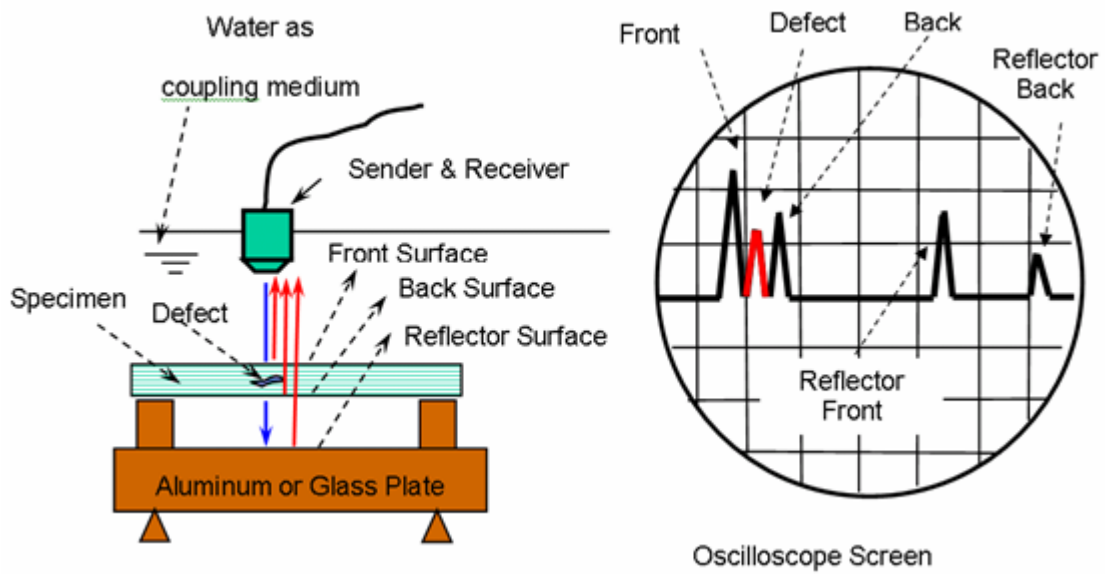
Fig. 3-11: Schematic of the C-Scan for laminate damage evaluation [21]

Fig. 3-12: Fusion splicer
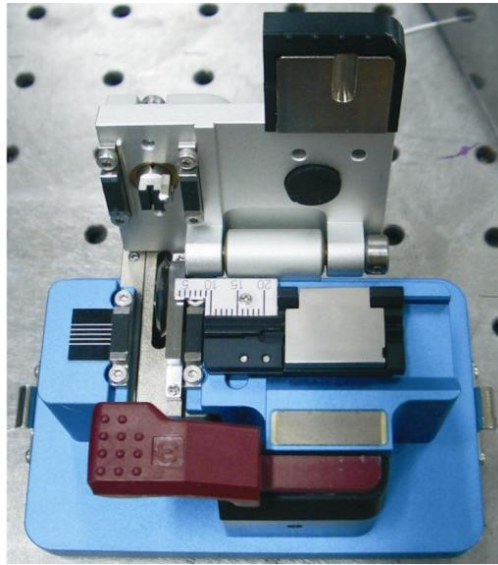
Fig. 3-13: Optical cleaver

Fig. 3-14: Optical cleaver
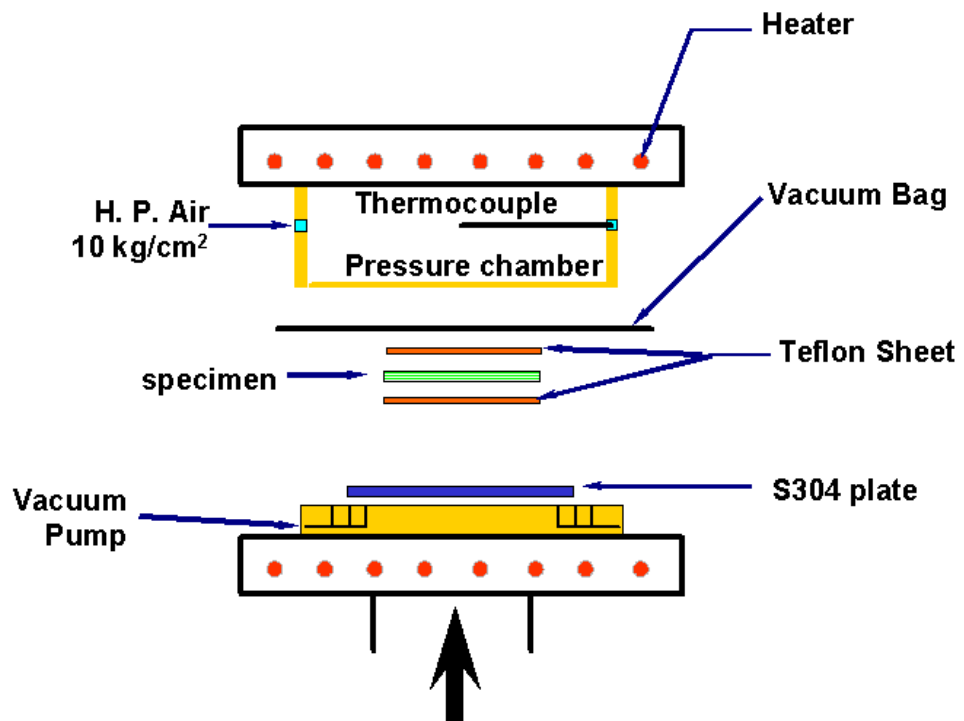
Fig 3-15: Schematic of the diaphragm type forming mold for laminate curing process
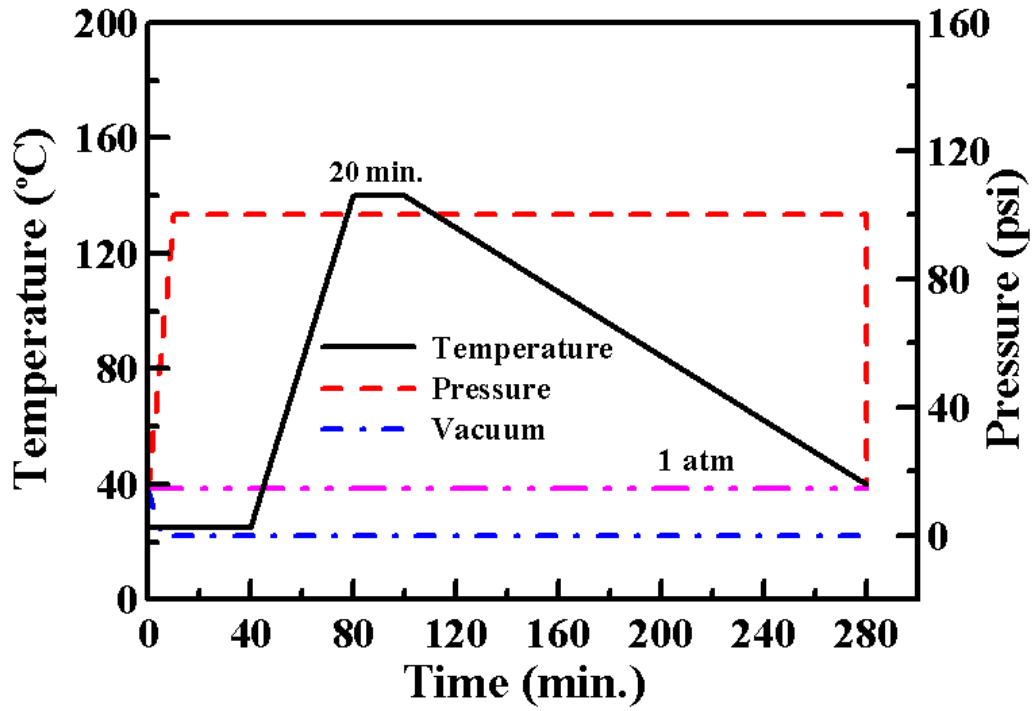
Fig. 3-16: The conditions for laminate curing process
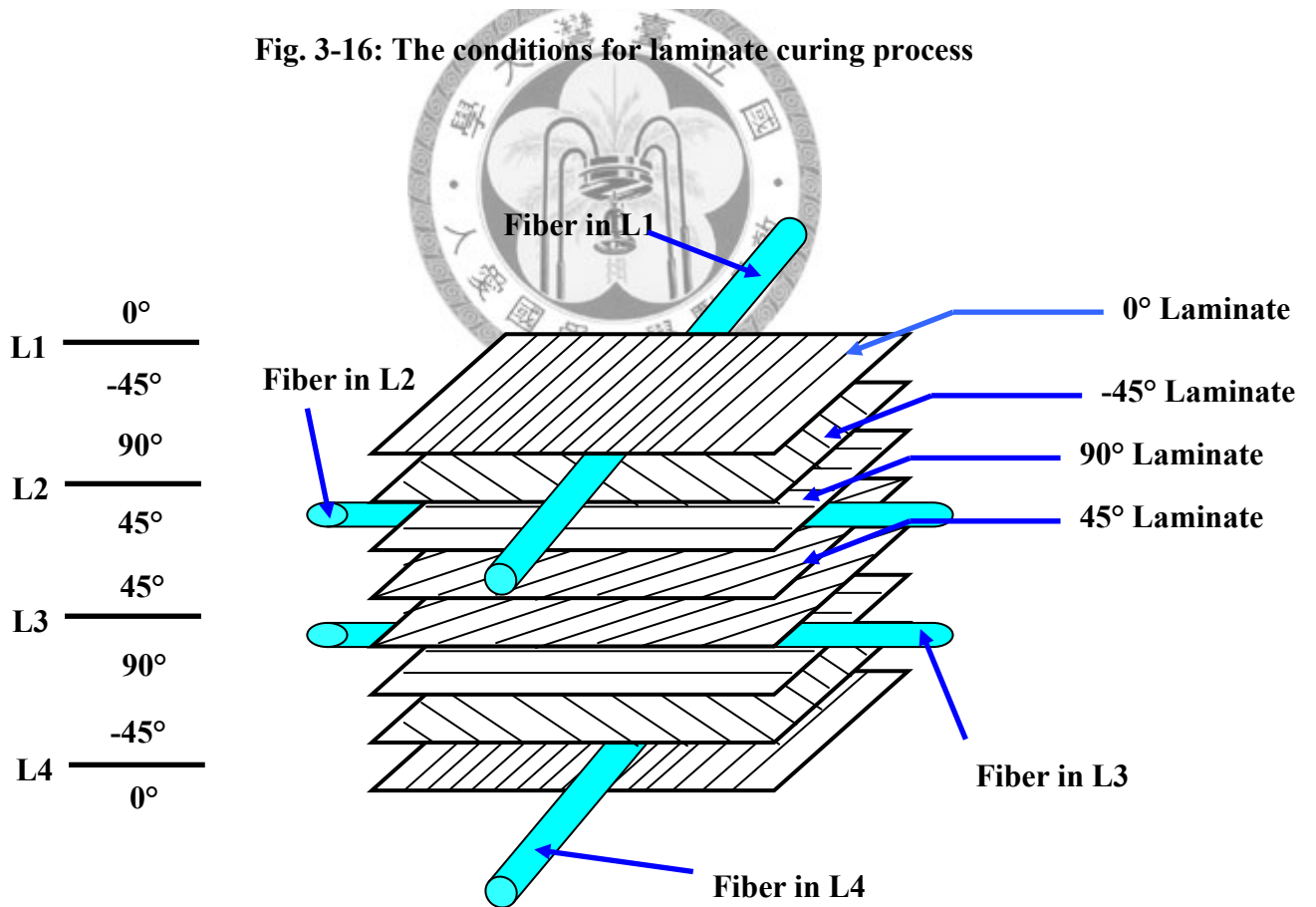
Fig. 3-17: Schematic of fiber-embedded method and laminates stacking sequence
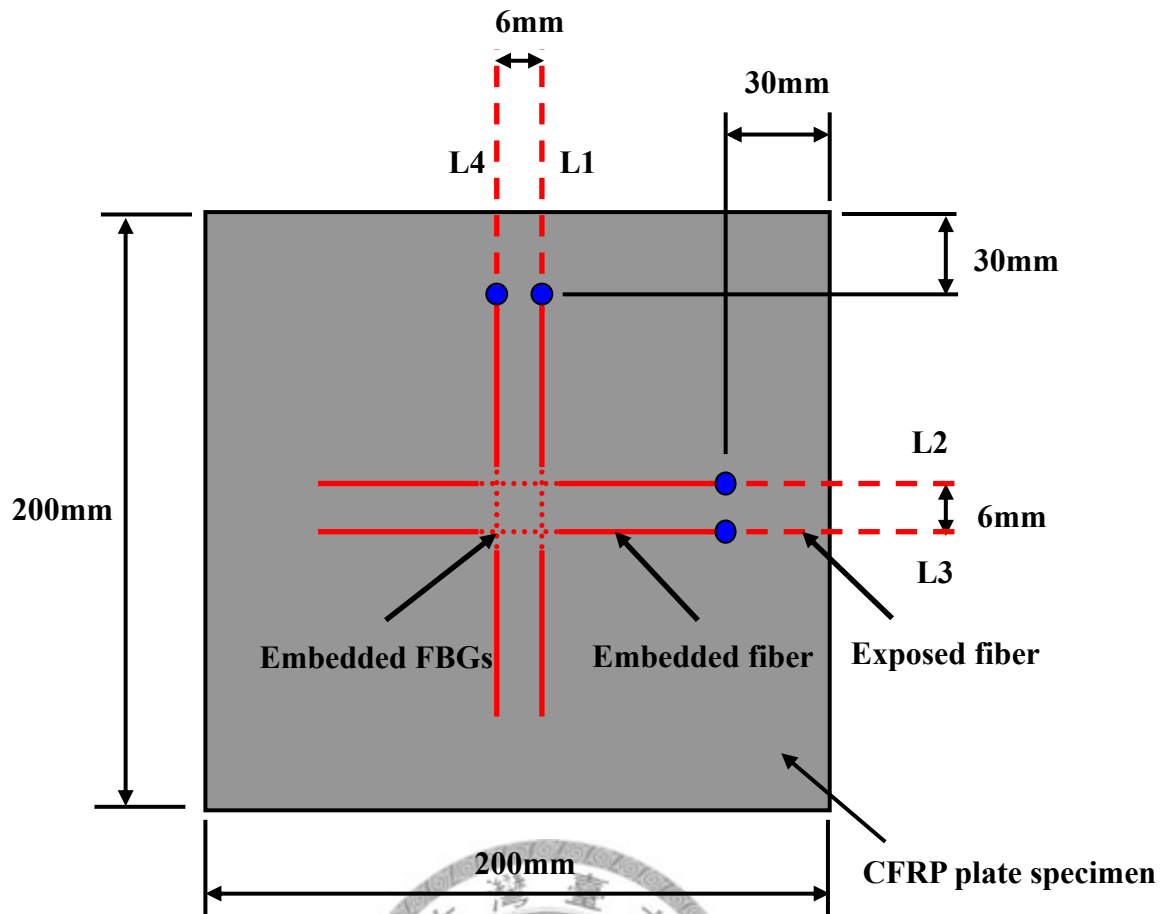
Fig. 3-18: Configuration of embedded FBGs in CFRP plate specimen

Procedure for impact test
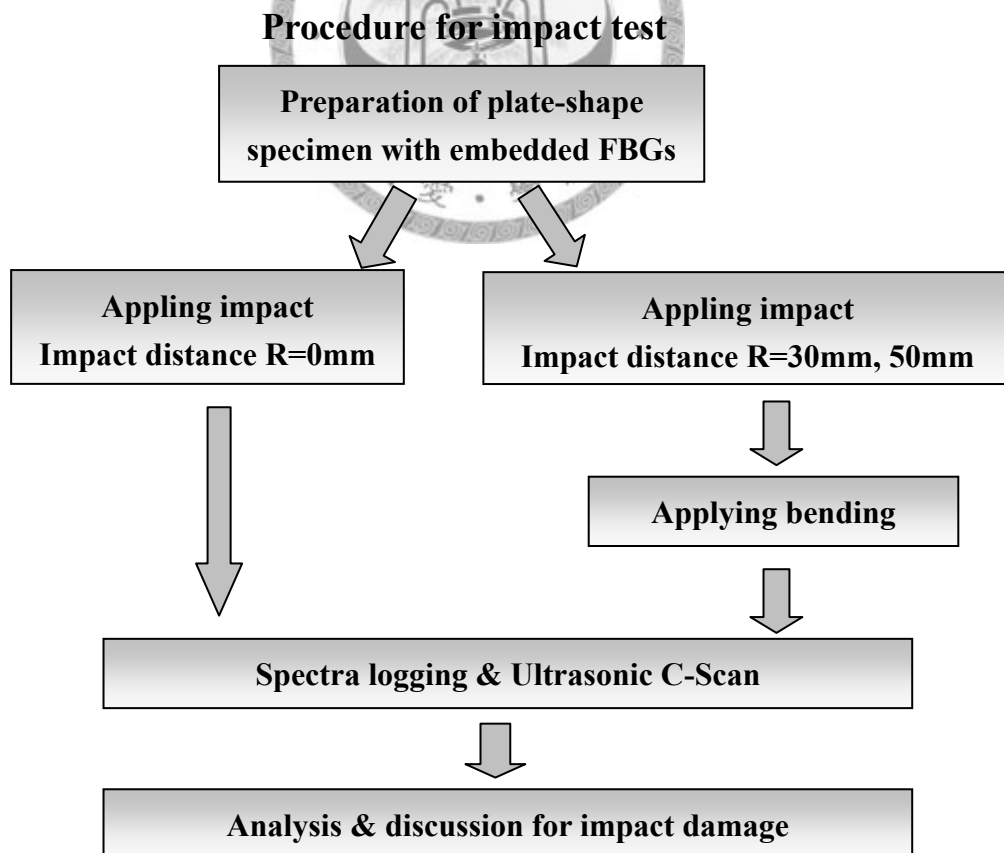
Fig. 3-19: Experimental procedure flow diagram for impact test
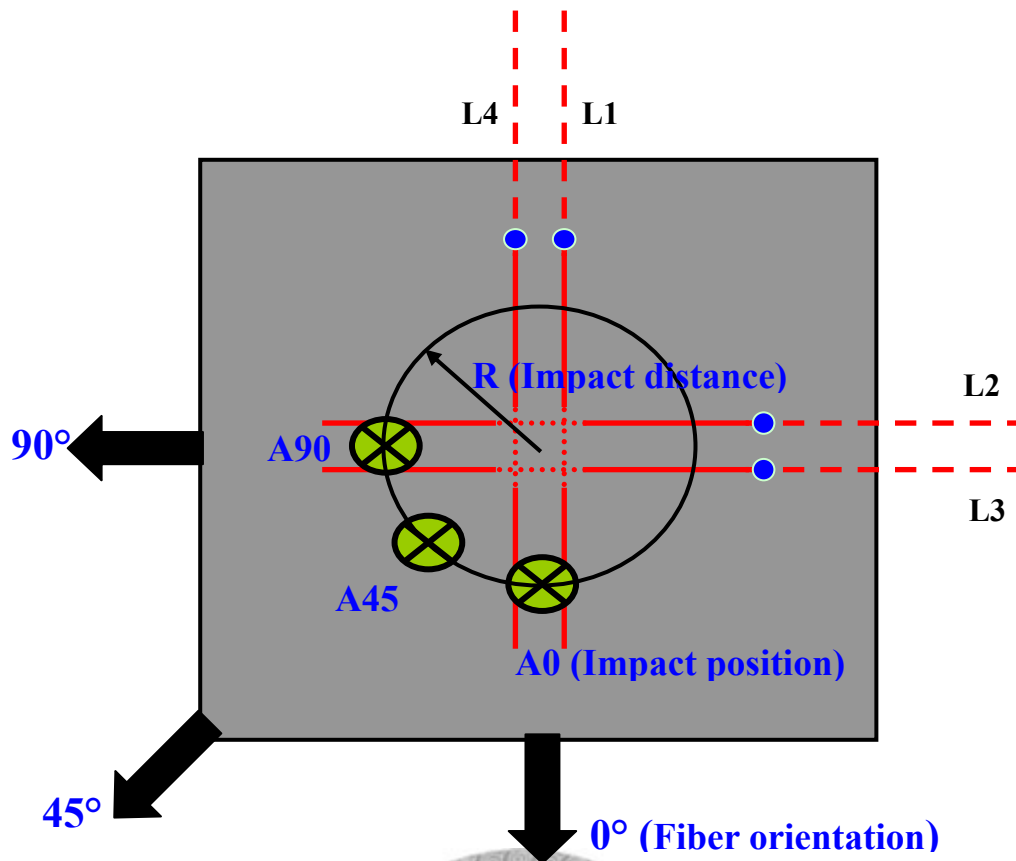
Fig. 3-20: Schematic of Impact distance R and Impact positions A0, A45, and A90
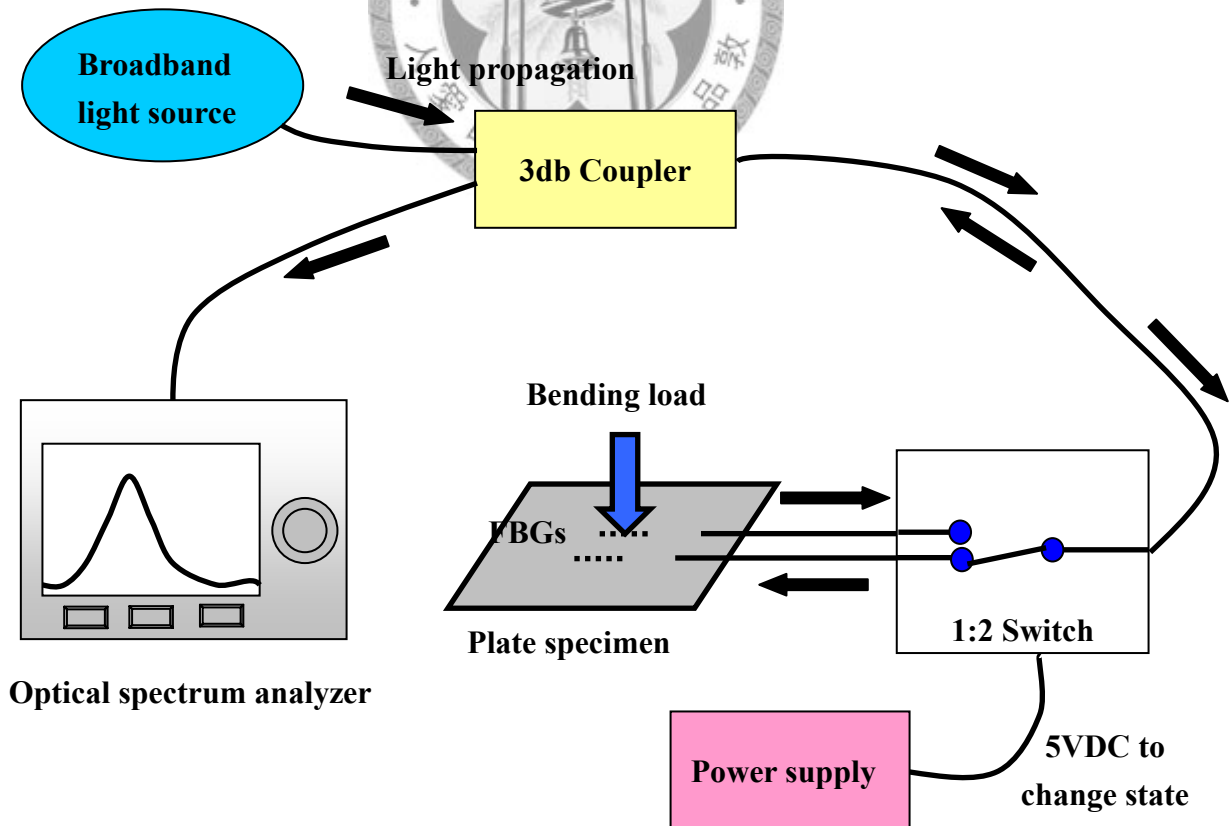
Fig. 3-21: Schematic of experimental setup in bending test
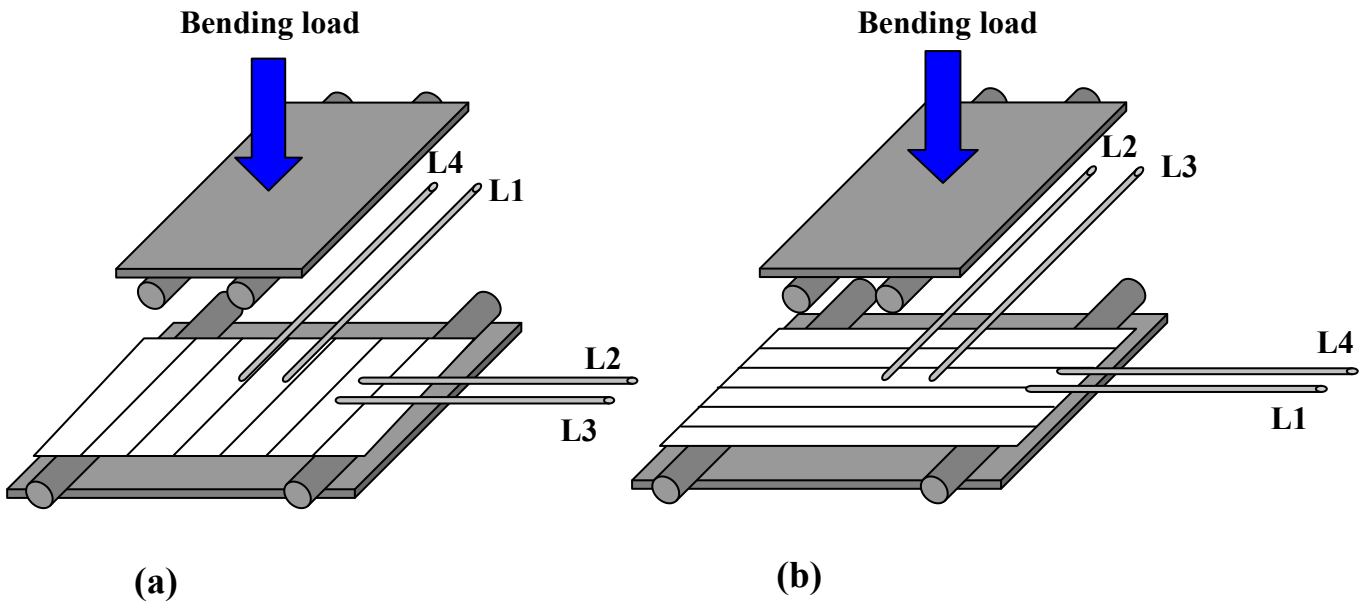
Fig. 3-22: Bending test was conducted in different directions for measuring embedded FBG sensors in each layer. (a) For measuring the FBGs in L2 and L3 (b) For measuring the FBGs in L1 and L4
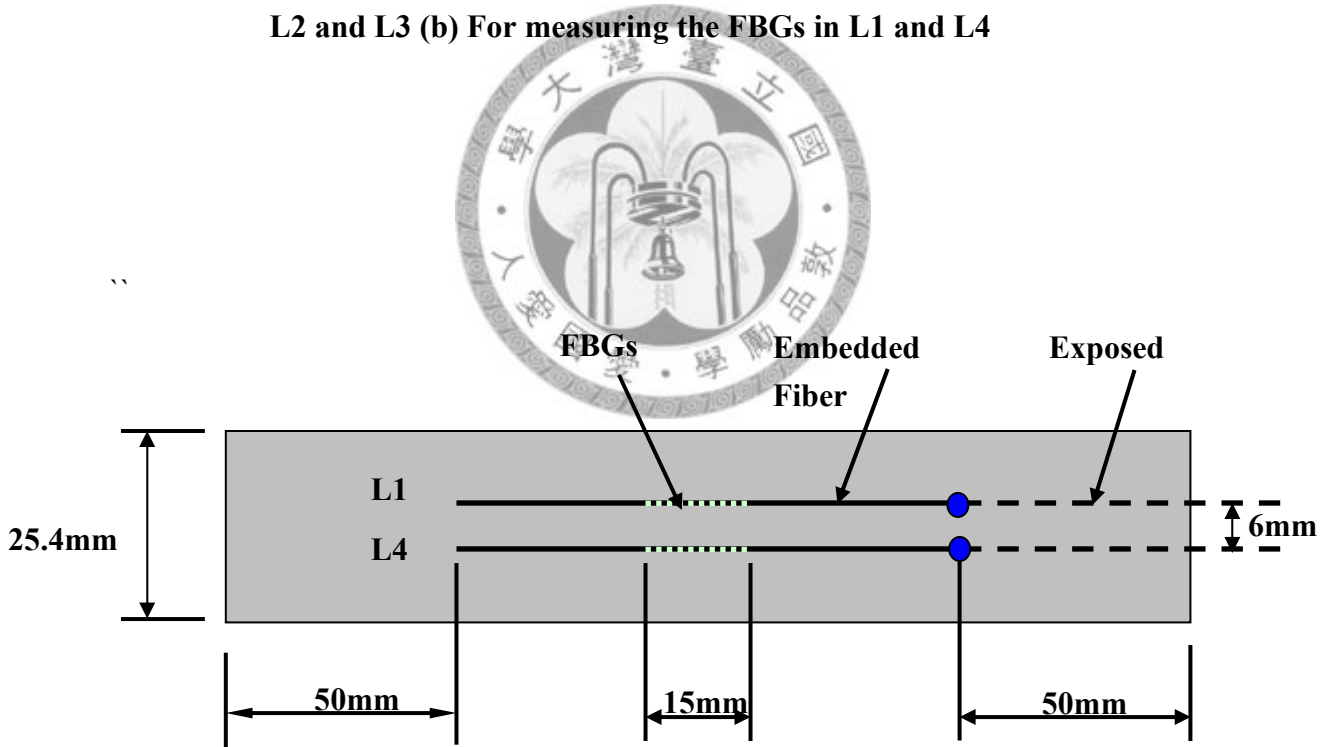
Fig. 3-23: Configuration of test specimen for post-impact fatigue test

Procedure for post-impact fatigue test
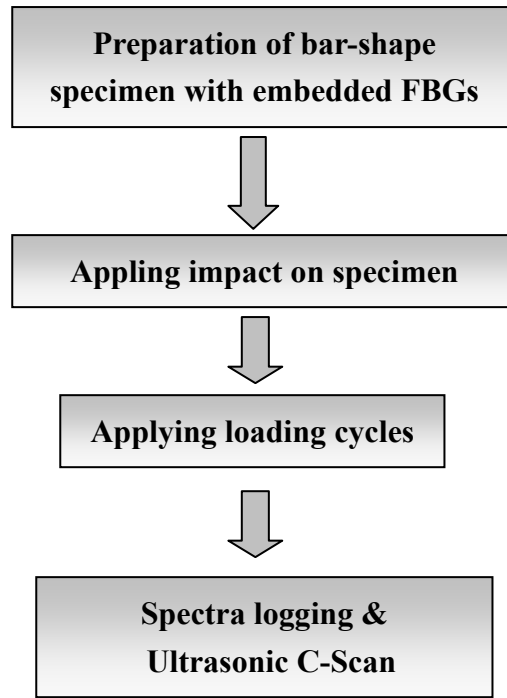
Fig. 3-24: Experimental procedure flow diagram for post-impact fatigue test
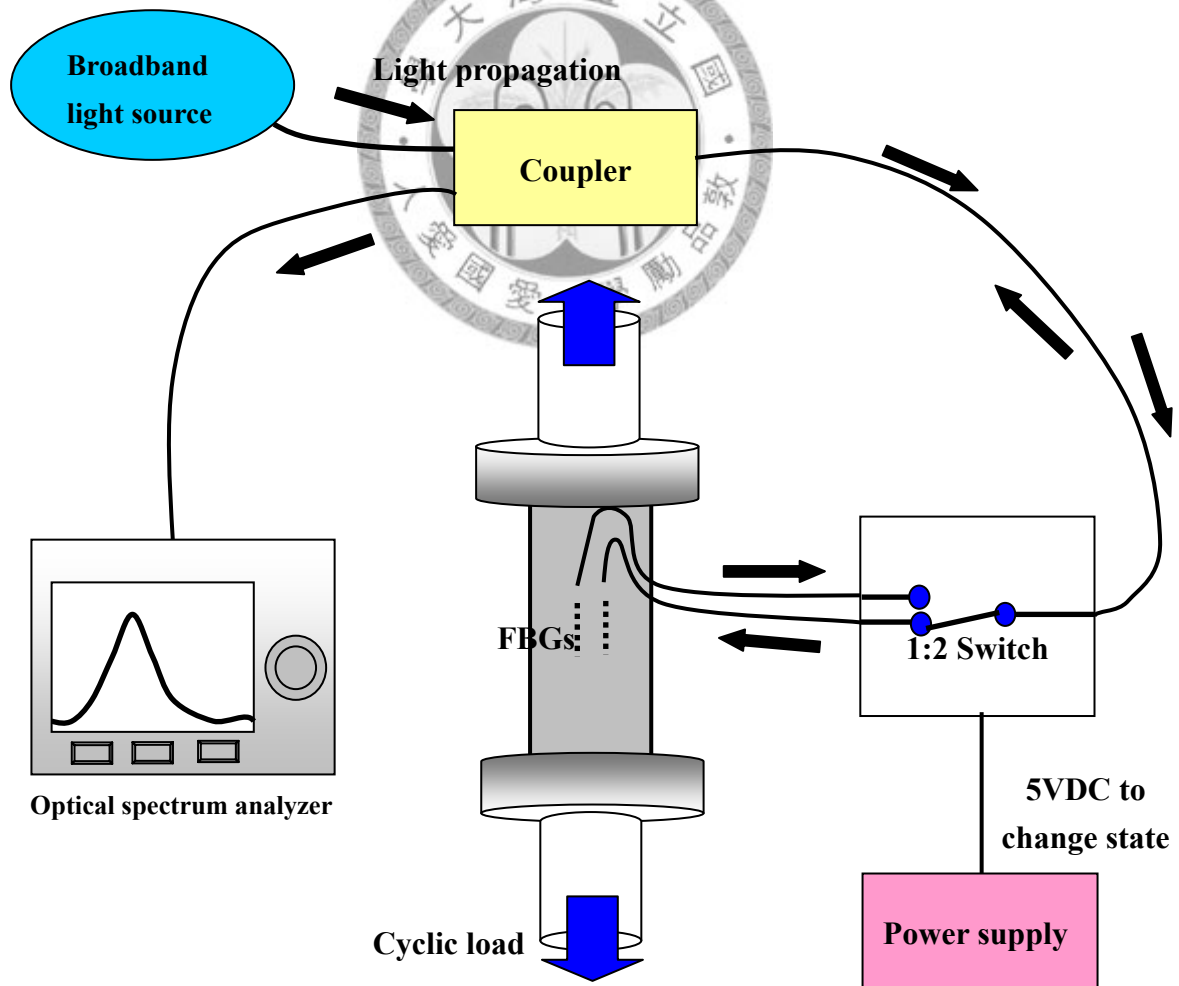
Fig. 3-25: Schematic of experimental setup in post-impact fatigue test
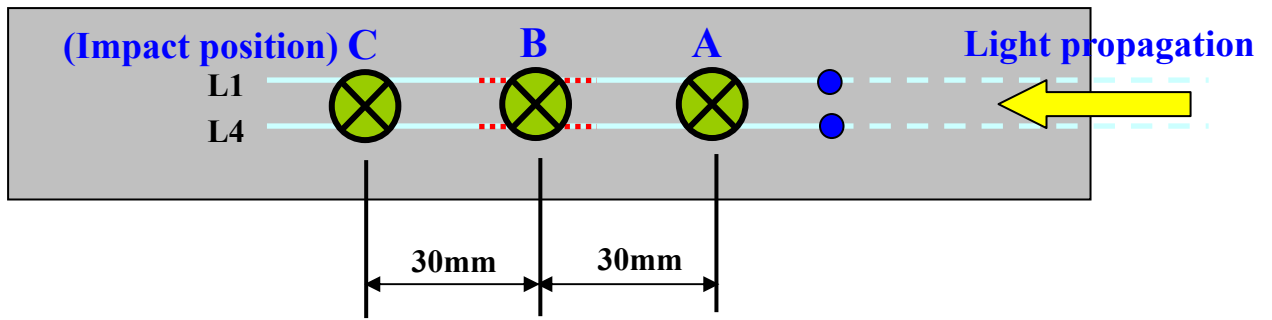
Fig. 3-26: Schematic of Impact positions A (in the upstream of the gratings based on the route of the light propagation), B (the center of the specimen), and C (in the downstream of the gratings based on the route of the light propagation).

Drop height	Iron dart (260g)	Aluminum dart (90g)
80cm	2.04J	0.71J
140cm	3.57J	1.24J

Table 3.1: Impact energies from different drop heights and dart masses

Impact Distance (R)	Drop Height (H)	Bending test					
0 mm (center)	80cm	Before impact		After impact			
	140cm	Before impact		After impact			
30mm	80cm	Before impact	✓	After impact	A0 (1st) ✓	A45 (2nd) ✓	A90 (3rd) ✓
	140cm	Before impact	✓	After impact	A0 (1st)	A45 (2nd)	A90 (3rd) ✓
50mm	80cm	Before impact	✓	After impact	A0 (1st) ✓	A45 (2nd) ✓	A90 (3rd) ✓
	140cm	Before impact	✓	After impact	A0 (1st)	A45 (2nd)	A90 (3rd) ✓

Table 3.2: Experimental parameters in impact test

Chapter 4 Results and discussion

4.1 Embedded FBGs in CFRP composite

The embedded FBG sensors were influenced by the thermo residue stress after the curing process of CFRP. Fig. 4-1 compares the reflective spectrum of FBG before and after being embedded. The single peak spectrum split into two distinct peaks with decreased power intensity, revealing that the FBG was under the non-uniform strain due to diametral residual stress induced during fabrication. Virtually all the FBG sensors embedded in each layer split alike. This phenomenon has been observed in previous study as well [16].
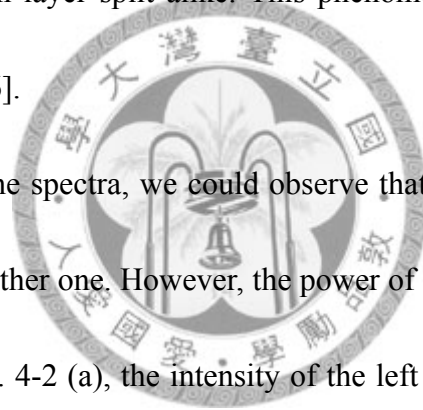
Furthermore, from the spectra, we could observe that the left peak had a higher power intensity than the other one. However, the power of each peak would reverse as the fiber was bent. In Fig. 4-2 (a), the intensity of the left peak was originally higher than the right one. However, on bending, the intensity of left peak was degenerated, as shown in Fig. 4-2(b), and the loss power was transferred to the right peak. Therefore the right side peak became higher and the left side peak became lower. From the discussion in chapter two, this phenomenon can be best explained by birefringence effect [17]. When the FBG sensors were embedded in CFRP laminates, the residue stress in the diametral direction caused the reflective spectra of FBG sensors splitting into two peaks. Bending change this residual stress as well as the longitudinal stress on the fiber,

giving rise to the observed phenomenon. One previous study [17] has explained that the bends of the fiber could induce the geometric modification, hence the refractive index of fiber was changed. It resulted in a light coupling in the fiber, and energy exchange between two modes as they propagated.

4.2 Impact on the FBGs (R=0mm)

4.2.1 R=0mm, H=80mm

In this test, the impact was applied at the center of the specimen under 80mm drop height, ensuring the arranged FBG sensors in the vicinity of the impact source. Fig. 4-3 shows the reflective spectra from FBG embedded sensors in each layer between before and after impact under 80cm drop height. The deformation of spectra of FBG embedded in L1 between before and after impact was not matched, nonetheless the width of the reflective peak became widened. The result best explained that the impact damage had affected the embedded FBG sensor, but the impact damage was relatively smaller in L1. Therefore, we could infer the impact load induced less damage on the most upper layer. For the FBG sensors in L2 and L3, there were significant changes in the spectra between before and after impact. The original waveform of the FBG embedded in L2 which almost deformed completely and the two peaks in the spectra of FBG embedded in L3 separated into four peaks. These significant changes indicate that the impact-induced damage in L2 and L3 were more serious than other layers. For the
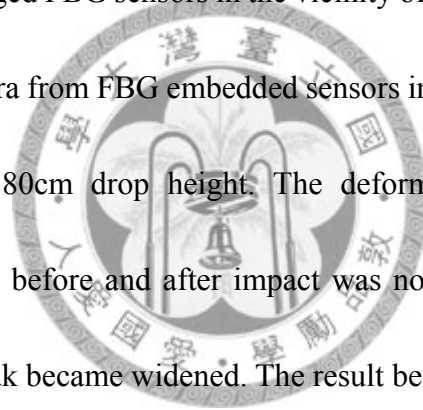
FBG sensor in L4, the small side peaks were generated by the impact, but the change in spectra was not as evident as the FBG in L2 and L3. According to the above results, it appears that the impact load may induce serious damage in L2 and L3, and although L1 faced impact directly, the impact damage was relatively slight.

4.2.2 R=0mm, H=140mm

Fig. 4-4 shows the reflective spectra from FBG sensors embedded in each layer before and after impact under a drop height 140cm. For the FBG sensor in L1, it was found that there was an alteration in the peak area, yet the deformation of spectrum was not significant. For the FBG sensors in L2 and L3, similarly to the previous condition, the original peaks broadened and separated into more peaks. For the FBG sensor in L4, due to the increase of impact energy, the spectra had significantly changed and the two peaks were separated into irregular forms. Based on the above mentioned, we found the power of reflective light which decreased due to the impact damage. Generally, the reductions of the power in each FBG were larger than previous ones.

4.2.3 Micrographs of impact-damaged CFRP specimen

One study [26] has shown the optical micrographs on the sectional view of the impact-damaged specimens (Fig. 4-5 and Fig. 4-6). Under the 80cm drop height, it could be observed that the delaminations in the middle laminates and some cracks in the middle and bottom laminate, as shown in Fig. 4-5. Although the up laminate faced

the impact load directly, it seemed to have less visible damage. Fig. 4-6 shows the micrograph on the sectional view of the impact-damaged specimen under the 140cm drop height. It was found that the density cracks and deliminations increased in the laminates. Moreover, we could observe one crack developed to the up laminate. It shows the larger impact energy induced more serious damage, which might cause higher reduction in intensity of the reflective spectra from FBG sensor.

From the micrographs we can observe delaminations were induced in the middle layer, and some cracks in the middle and bottom layer. However, the impact induced relative less damage in the up laminate, even though it was faced the impact directly. These results are in good agreement with reflective spectra of embedded FBG sensors. According to the above results, the FBG sensors could detect the impact damages in different degrees. In addition, the results shows the sensors were well-protected in CFRP plate specimen in which they could directly endure the determined impact energy in this study.
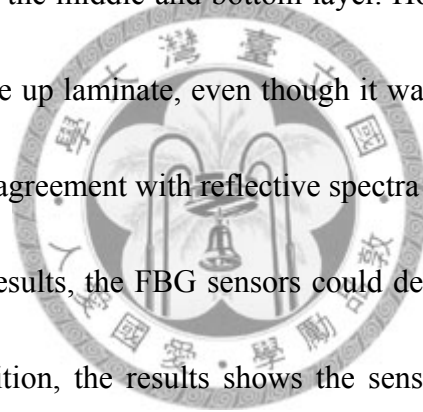
4.3 Impact at 30mm from FBGs (R=30mm)

4.3.1 R=30mm, H=80cm

This experiment aimed at evaluating the ability of impact damage detection from a distance. The iron falling dart was employed to impact on the CFRP plate specimens at heights of 80cm at the three positions: A0, A45, and A90, in sequence. The spectra

were recorded before and after each impact completed. Fig. 4-7 shows the reflective spectra from FBG sensors embedded in each layer between before and after impact under 140cm drop height and a distance 30mm away from FBG sensors. It could be seen that the deformations of waveform were not significant. This suggests the FBG sensor is not sensible to the impact damage at the current distance of 30mm under the load-free condition. For this reason, the bending test was conducted to review the deformation of waveform and shifts in wavelength.

Fig. 4-8 (a) shows the changes in the spectra from the L4 FBG sensor under the bending load before impact. The shifts were induced by the bending stress. There was no substantial deformation of waveform as the bending load was increased or released. Fig. 4-8 (b) shows the shifts in wavelength of the spectra from the embedded FBG sensor after impact at the three positions under 80cm drop height and a distance 30mm away from FBGs. We found out that the power intensity of the peak gradually decreased as the bending load increased or decreased. It was also found that the waveform had changed between before and after bending. After completely releasing the bending load, the spectrum did not return to the original shape. Moreover, the power intensity appeared to be a little lower than original state. Fig. 4-9 (a) and (b) show the shifts in wavelength of the spectra from the FBG sensor embedded in L1 before and after impact at the three positions under 80cm drop height and a distance 30mm away
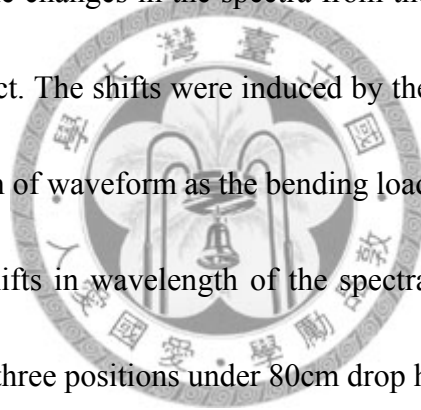
from FBGs. When the bending load was released, the intensity power just decreased slightly before impact. After the specimen was impacted, the power intensity decreased in comparison with previous condition as the bending load was released. The above results show that the action of bending stress on the impact damage has lead to some slight effect on the residual strain field surrounding the FBGs. The same as previous results, the intensity reduction in L4 was larger than that in L1 after test bending load was fully released.

For the quantitative evaluation, the wavelength shifts was plotted as a function of bending load. In each bending test, we conducted three bending cycle on the specimen. Fig. 4-10 (a) and (d) shows the wavelength shifts during the bending test before impact. Due to the resolution limitation of the OSA and variation of environmental temperature, the initial peak wavelength would change in each bending test. However, the comparison of the peak wavelength shifts during the bending test depends on the line deviation and slop, so the different initial peak wavelength would not affect the measurement. It was found from the charts that the peak wavelength shifts of the FBGs embedded in each layer could almost linearly increase or decrease during the bending test, and the slope had no significant change. To check reproducibility, we conducted another three bending cycles again on the specimen. The results showed that the bending did not substantially affect the CFRP specimen, and the embedded FBG

sensors could stably adhered to the reinforced fiber before impact.

Taking into account a simply supported beam under four-points bending state, the bending moment M in the middle of the beam is in proportion to applied bending load. The bending stress in the middle of the beam can be written as the following:
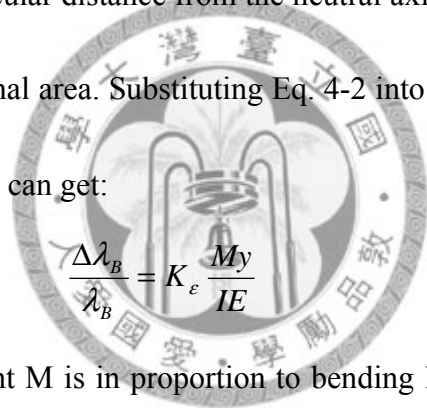
$$\sigma = \frac{My}{I} \tag{4-1}$$

and the strain ε can be derived as the following:

$$\varepsilon = \frac{My}{IE} \tag{4-2}$$

where y is the perpendicular distance from the neutral axis, and I is the moment of inertia of the cross-sectional area. Substituting Eq. 4-2 into Eq. 2-17, while neglecting the temperature effect, we can get:

$$\frac{\Delta\lambda_B}{\lambda_B} = K_\varepsilon \frac{My}{IE} \tag{4-3}$$

Since the bending moment M is in proportion to bending load, the wavelength shifts were directly proportional to the bending load. The L1 and L2 were above the neutral axis, so the wavelength shifts linearly increased as the bending load increased. On the contrary, the wavelength shift in L3 and L4 were decreased as the bending load decreased.

After impacting on the CFRP plate specimen, several occasions of damage in the specimens took place. The wavelength shifts along the bending test were influenced by the damage. Fig. 4-11 (a) to (d) show the comparison of wavelength shifts from

embedded FBG sensors along bending test before and after impact, under an 80cm drop height and a distance 30mm away from FBG sensors. The first impact was applied at A0, then the second impact was applied at A45, finally the third impact was applied at A90 in one specimen. The bending test was conducted as each impact was completed, and recorded the peak wavelengths under different bending loads. After impact at A0 (the first impact), the wavelength shift was not able to return to the initial wavelength as the three bending load cycles completed. It shows that the hysteresis started to take place after the damage was induced in the specimen. After impacting at A0 and A45 (the second impact), it was found the line deviation tended to be enlarged. It shows the two impact damages seemed to have more influence to the specimen. After impact at A0, A45, and A90 (the third impact), the deviation of the line due to the bending enlarged again. For each case, it was could be observed hysteresis occurred and the wavelength could not return to the initial value after each bending cycle was completed. The slope just slightly change after each impact was completed, it showed that the alteration of slope could not be an indicator to help us infer the degree of impact damage in specimen.
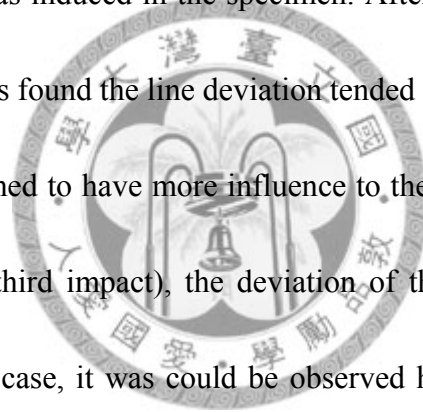
4.3.2 R=30mm, H=140cm

`Fig. 4-12 (a) and (b) show the comparison of wavelength shifts from embedded FBG sensors along bending test before and after impact under a 140cm drop height and

a distance 30mm away from FBG sensors. In this test, the bending tests were conducted and the spectra were recorded before and after the three impacts were completed. Before impact, the peak wavelength shifts from FBGs in L1 and L2 almost increased or decreased linearly during bending test, this showed that they had good repeatability under different bending stresses. For the FBGs in L2 and L3, it could be observed that the lines diverged slightly before impact, this might be caused due to the fiber had not fixed very well during fabricating processes.

The fiber in L1 was fractured during the second bending cycle after impact due to artificial cause. However, the hysteresis phenomenon was still observable. For the FBG in L2, L3 and L4 after impact, the shifts of peak wavelength diverged obviously as the three bending cycles were complete. Comparison of the peak wavelength shifts of the FBGs in all layers, it could be seen the lines of peak wavelength shifts had evident deviations after impact. This shows the impact induced the defects in specimen, and caused stress concentration under bending load. The FBG in each layer could reflect the induced stress change by conducting the bending tests.

The impact-induced damages were also investigated by Ultrasonic C-scan, as shown in Fig. 4-13 and Fig 4-14. From above results, we can conclude that the FBG sensors could be used to investigate interior damage within a 30mm distance.

4.4 Impact at 50mm from FBGs (R=50mm)

4.4.1 R=50mm, H=80cm

In this experiment, the impact distance extended from 30mm to 50mm, and the impacts were applied under an 80cm drop height. The designated impact positions were A0, A45, and A90. The first impact was applied at A0, then the second impact was applied at A45, finally the third impact was applied at A90 in one specimen. The bending test was conducted as each impact was completed, and recorded the peak wavelengths under different bending loads. Fig. 4-15 (a) to (d) show the comparison of wavelength shifts from embedded FBG sensors along bending test before and after impact under the 80cm drop height and a distance 50mm away from FBG sensors. For the FBG in L1, it could be seen that the lines diverged after impact at A0 (first impact). After impact at A0 and A45 (second impact), it had no evident increase in deviation in peak wavelength shifts. One possible reason could be that the second impact not only induced the impact damage, but also occasionally compressed the laminates structure, resulting in the optical fiber was inlaid by the reinforced fiber again. Hence, the effect of stress concentration under bending load near the FBG sensor did not increase. As a result, the deviations did not have significant increase. However, after impact at A0, A45, and A90 (third impact), the deviations increased again. It shows the third impact further damaged the specimen, causing more significant stress concentration under the

bending stress. The trends of the deviations in peak wavelength shifts of the FBG in L2 and L3 were similar. It could be seen the deviations keep increasing as each impact was completed. After all the impacts were completed, we could observe the significant deviation of the lines. Hysteresis phenomenon occurred in wavelength drifts after impacting at each position. For the FBG in L4, the slight deviation could be observed before impact. This might be caused by the artificial cause during fabricating process. The deviations increased after impact at A0 (first impact), but did not have obvious increase after impact at A0 and A45 (second impact). It was similar with the result in L1. After all the impacts were completed, the FBG sensor responded the obvious hysteresis in peak wavelength drifts. Above results show that all the sensors appeared to be obvious hysteresis phenomenon after the third impact was completed. By comparison, the deviations of wavelength shift in L2 and L3 were more significant than they were in L1 and L4. We could infer the impact damage induced larger influence in L2 and L3 than that in L1 and L4.

4.4.2 R=50mm, H=140cm

Fig. 4-16 (a) and (b) show the comparison of wavelength shifts from embedded FBG sensors along bending test before and after impact under a 140cm drop height and a distance 50mm away from FBG sensors. In this test, the bending tests were conducted and the spectra were recorded before and after the three impacts were completed.

Before impact, the peak wavelength of the FBGs in L2 and L4 could almost increase or decrease linearly during bending test. The slight deviations appeared in the lines of peak wavelength from the FBGs in L1 and L3. For each layer, the line of peak wavelength diverged apparently as the three bending cycles were completed after impact at A0, A45, and A90.

Above results shows the FBG sensors could detect the impact damage up to 50mm away from the sensors. Fig. 4-17 and 4-18 show the Ultrasonic C-scan images of specimen between before and after impact. Ultrasonic C-Scan facilitated us in finding out the exact positions and scale of the impact damage. In next section, we will discuss the relation between the degrees of lines deviation and impact distance R and drop height H.
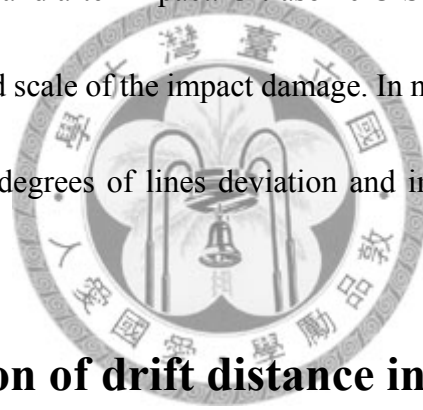
4.5 Quantification of drift distance in peak wavelength lines

So far, we determined the degrees of impact damage by observing the occurrence of hysteresis in the line of peak wavelength shifts. In order to quantify the degrees of hysteresis in wavelength shifts during bending cycles, we utilize the root-mean-square deviation (RMSD) to evaluate the average drift distances before and after impact at A0, A45, and A90. The method was shown in Fig. 4-19. The bottom line is the wavelength shifts of increasing bending load in the first cycle, and the top line is the wavelength

63

shifts of decreasing bending load in the third cycle. These two lines were selected to calculate the average drift distances of peak wavelength after the three bending cycles were completed by following formula:

$$RMSD(\lambda_1, \lambda_2) = \sqrt{\frac{\sum_{i=1}^{n}(\lambda_{2,i} - \lambda_{1,i})^2}{n}} \qquad (4\text{-}4)$$

where λ_1 is the wavelength of increasing bending load in the first bending cycle, and

λ_2 is the wavelength of decreasing bending load in the third bending cycle.

Tables 4.1 to 4.4 summarize the average drift distances of peak wavelength lines in each layer under experimental parameters of different impact distances and drop heights. These drift distances were obtained from previous results. For each table, it was found that the average distances were usually below 0.011nm before impact except 0.016nm under the conditions (FBG in L1, R=50mm, H80mm, before impact) and 0.026nm under the conditions (FBG in L4, R=50, H80cm, before impact). This might be due to sensor misalignment during fabricating process.

For the FBG in L1 (Table 4.1), it was observed that when the specimen was subject to impact at A0 (first impact) under R= 30mm and H=80cm, the distance had a significant increase to 0.041nm. However, it was found that it slightly decreased after impact at A0 and A45 (second impact). This indicates that the second impact load could probably compress the laminates and release the residual stress induced by first impact, and optical fiber to be stably inlaid again. However, after impact at A0, A45, and A90

(third impact), the average distances increased to 0.054nm. For R=50mm and H=80cm, it could be seen the drift distance of peak wavelength was reduced between after impact at A0 (first impact) and after impact at A0 and A45 (second impact), finally increased to 0.040nm after impact at A0, A45, and A90 (third impact). It is similar with the results under the conditions R=30mm, H=80cm. Above results show when the second impact was applied, it had higher probability to release the residual stress induced by first impact. However, compared with the results, the drift distances of peak wavelength had evident increases after impact. This shows the more impact damages could induced more complex stress under the bending load, causing the lines of peak wavelength to drift after bending test.
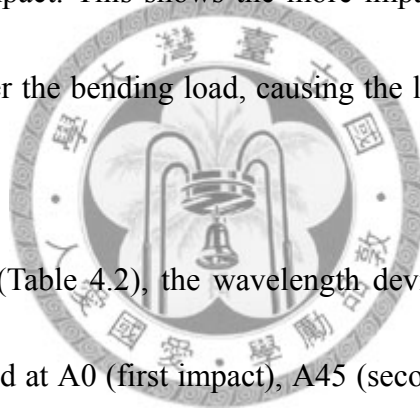
For the FBG in L2 (Table 4.2), the wavelength deviations increased gradually when impacts were applied at A0 (first impact), A45 (second impact), and A90 (third impact), in sequence. It could be observed that there was no decrease in peak wavelength drift after impact at A0, A45, or A90 under the conditions (R=30mm, H80cm) and (R=50mm, H80cm). The drift distance increased gradually as each impact was completed. The similar results were obtained from the FBG in L3 (Table 4.3). After all the impacts were applied, the average drift distances in peak wavelength had significant increase. These results are in line with earlier hypothesis that more impact damages could induced more complex stress under the bending load, causing the larger

average drift distance in peak wavelength during bending test.

For the FBG in L4 (Table 4.4), the drift distance in peak wavelength gradually increased as each impact was completed under the condition R=30mm, H=80cm. Nevertheless, it was found slight reduction in drift distance between after impact at A0 (first impact) and after impact at A0 and A45 (second impact). It shows the impact induced recovering of drift distance in peak wavelength might occur in L4. After all the impacts were applied, the drift distances increased, which agrees with previous results.

Table 4.5 summarizes the difference of drift distances in peak wavelength between before impact and after impact at all positions. The differences of drift distances in L1 and L4 were larger than they in L2 and L3 due to the different values of peak wavelength shift during bending test. From the table, it could be found that the differences under the same impact distance but different drop heights were different. Higher impact energy caused larger differences of drift distance in peak wavelength in all layers except L3. For the same drop height but different impact distances, the differences of drift distance between before and after impact were also different. The values were larger under closer impact distance to the embedded FBGs except in L2. Generally, the FBG sensors responded larger drift distances during bending test under higher impact energy and closer impact distance to embedded FBGs, but it appears that the drift distance of peak wavelength are not fully relate to impact distance and impact
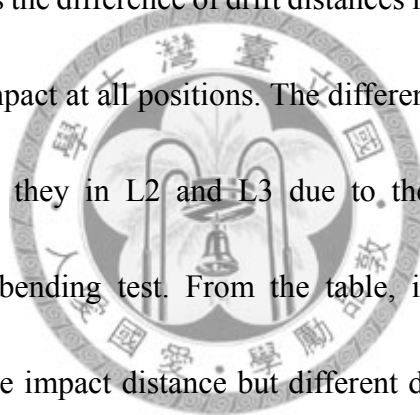
energy.

In summery, these results suggest the FBG sensor could detect to the impact damage in a distance, but it seems that FBG sensor could not efficiently evaluate the damage distances and energies. However, the average drift distance in peak wavelength had significant changes after impact at the three positions. The drift distance before impact was about under 0.015nm. After impact at A0, A45, and A90, it was about 0.040 to 0.050nm.

4.6 Results of post-impact fatigue test for impact position B

In this experiment, the fatigue test was carried out after the impact damage was made at specimen. Measurements were taken when the specimen was free after a completion of a certain amount of load cycling.
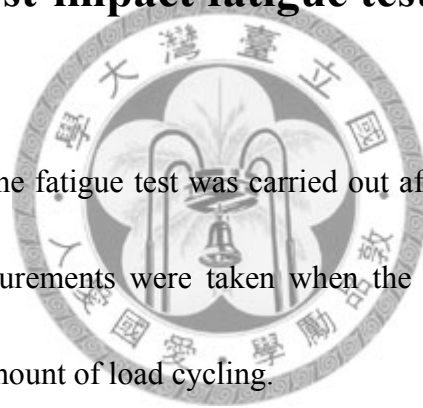
Fig. 4-20 and Fig. 4-21 show the spectra from FBGs embedded in L1 and L4 which were deformed as fatigue cycles increasing after an impact drop from 80cm at the impact position B. After impact, the spectrum was distorted into the irregular forms, which was the same comparing with previous results. As the fatigue cycles increased, the intensity of other wavelengths dramatically increased (at 10000 cycles in L1 and 5000 cycles in L4). As the cycles increased, the characteristic peak of the FBG gradually submerged.

Fig. 4-22 and Fig. 4-23 show the spectra from FBGs embedded in L1 and L4 which were deformed as fatigue cycles increased after an impact drop from 140cm at the impact position B. For the FBG in L1, it was discovered that the intensity of other wavelength notably increased at 10000 cycles, and the waveform slightly changed. As the fatigue cycles increased, the intensity in other wavelength also gradually increased. This result was similar with the previous results which was under drop height 80cm. For the FBG in L4, it also revealed the intensity of other wavelength gradually increased during the fatigue test. At 10000 cycles, we noticed the whole waveform of spectra was significantly altered. The spectra displayed that the waveform became corrugated in other wavelength, and the intensity of wavelength gradually attenuated from 10000 cycles to 200000 cycles. At 200000 cycles, the other wavelength surmounted the reflected wavelength peak, resulting in the wavelength peak of FBG sensor hardly distinguished from the spectrum.

Fig. 4-24 shows the Ultrasonic C-scan result of specimen after 200000 cycles. No propagation of impact damage is evident. It should be pointed out that C-Scan mainly responds to delamination , matrix cracking, debonding and fiber fracture did not show up.

The specimen fatigued 200000 cycles after applying impact (H= 140cm) was cut and mounted to examine the post-impact fatigue damages using optical microscope.

Fig. 4-25 shows the sectional views of the post-impact fatigued specimen. The sections 2-2 and 3-3 were the impact damage area, and the sections 1-1 and 4-4 were away from the damage area about 30mm. It could be observed evident damage in section 2-2 and 3-3. Nevertheless, it was difficult to distinguish the impact-induced damage or fatigue-induced damage. No evident damage was found in sections 1-1 and 5-5. It might be that the post-impact fatigue test might induce the development of cracks and delamination from the impact damage region, but not inducing new defects in other regions. According to the changes in spectra of the embedded FBGs, there should be the strain field alteration in specimen during post-impact fatigue test. However, we could not infer what structure alteration in the specimen from the optical micrographs. It indicates the fatigue- induced damage development could not be effectively estimated by optical micrographs.
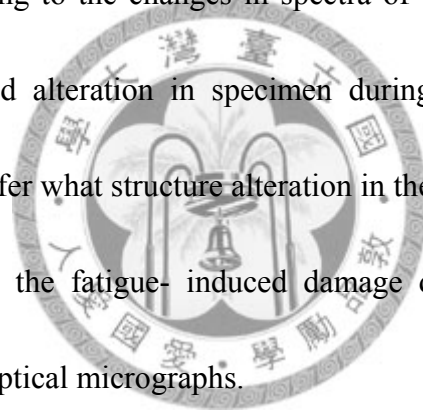
The disappearance or near disappearance of the characteristic Bragg wavelength peak may be caused by a highly non-uniform strain field around the FBG that seriously interrupt its periodicity. Corrosion of the optical fiber may also be the corrupt as the specimen had been immerged in water for Ultrasonic C-Scan examination. Another possible cause of this phenomenon is that the impact may have induced micro cracks on the optical fiber, and the cracks were further developed during fatigue test. The existence of a large number of crack interfaces may help to

reflect light unselectively. Therefore, the FBG appeared to reflect the light in a wide wavelength span. To test the above hypotheses, a number of tests were designed and carried out.

4.7 Results of post-impact fatigue test for impact position A and C

If the micro crack theory is correct, then impact at the upstream or downstream of the FBG should induce the same phenomenon as above. For both cases, a drop height of 140cm was employed. Before impact, Ultrasonic C-scan was carried out to examine the specimens as before. Fig. 4-26 and Fig. 4-27 show the spectra from FBGs embedded in L1 and L4 with various fatigue cycles under a drop height 140cm at the impact position A. With respect to the FBG in L1, there was no significant change in waveform, and the intensity of the reflected wavelength peak of FBG sensor merely changed slightly. With respect to the FBG in L4, it was found the intensity of other wavelength notably increased at 5000 cycles, however the waveform did not show any significant change. As the fatigue cycles increased, the intensity of other wavelength gradually increased. At 200000 cycles, the reflected wavelength peaks of FBG sensor were almost surmounted by the increasing intensity of other wavelength. This spectrum was similar comparing with the result shown in Fig 4-20 nonetheless the phenomenon of increasing intensity in other wavelengths occurred at a later time.

70

Fig. 4-28 and Fig. 4-29 show the spectra from FBGs embedded in L1 and L4 with various fatigue cycles under 140cm drop height, and at the impact position C. With respect to the FBG in L1, the intensity of peak wavelength was reduced as the fatigue cycles increased, which indicated that the induced changes of strain fields had affected the reflectivity of FBG sensor. The increasing intensity in other wavelength, however, was not evident. With respect to the FBG in L4, the phenomenon of increasing intensity in other wavelength was not discovered from spectra in the earlier fatigue loading cycles. However, at 200000 cycles, the intensity of other wavelength had increased. The phenomenon only occurred in L4 at 200000 cycles in this test. The Ultrasonic C-scan had also been executed at 0 and 200000 cycles, as shown in Fig. 4-30. From the figure, it can be observed that the impact damage propagation induced was not revealed clearly by C-Scan after fatigue test.
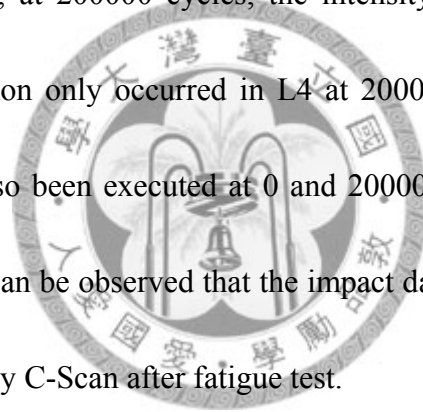
Summering the above observation, although the intensity rise of other wavelengths occurred to a certain extent in some of the case, such rise is far less extensive as observed before when the impact was made at position B. This largely ruled out the corrosion theory and the microcrack theory. The remaining explanation is a highly non-uniform strain field around the FBG. Even if impact is made at positions A or C, such a strain field may lead to a certain extent extends to the FBG due to the fatigue loading. In the following, we carry out a test with fatigue loading

71

only to see its effect on the FBG spectrum.

4.8 Result of fatigue without impact

Since impact damage might be the chief culprit which caused the light in a wide

wavelength range to be reflected, we conducted a fatigue test on the specimen without

impact. Fig. 4-31 and Fig. 4-32 show the spectra from FBGs embedded in L1 and L4

with various fatigue cycles which had undergone no impact. We observed that the

phenomenon of increasing intensity in other wavelength was not found in both figures.

These results indicate that if no prior impact damage occurred, the intensity increasing

in other wavelengths did not take place. The role of impact is to produce matrix cracks

and other defects that are grown by the further fatigue loading, inducing highly

complex non-uniform strain fields. If the FBG sensors were under these non-uniform

strain fields, it could reveal the phenomenon of increasing intensity in wide range of

wavelength.

To prove the above more conclusively, attempts were made to out from the CFRP

specimen. By submerging the specimen into acetone for about 2~3days, the epoxy

could be softened. The fiber can then be carefully drawn out from CFRP specimen.

The operation was done under an optical microscope. Fig. 4-33 and Fig 4-34

respectively show the optical micrographs of the FBG sensor embedded in L1 and L4,

which spectra before drawing out are shown in Fig 4-20 and Fig. 4-21. The

micrographs reveal some residual resins on the fiber surface. No obvious indication of crack was found.   We then focused on the cladding of the fiber as shown in Fig 4-33 (b) and Fig 4-34 (b), no evident defect was found. This shows the impact and post-impact fatigue did not induce evident defects the FBG sensor.

To examine whether the optical fiber was influenced by the impact, the FBG sensors drawn out from specimen and the fiber optic patch cord were jointed together to review the spectra with OSA. Fig. 4-35 compares the spectrum from the FBG before and after being drawn out from the composite specimen. Clearly when the non-uniform strain fields due to the CFRP specimens is removed, the spectra of FBG sensors revert to its original state before embedded.

Further, we conducted a bending test by sticking the fiber which spectra are shown in Fig 4-20 on a spring steel strip to apply a tensile stress on the fiber, as illustrated in Fig 4-36. A strain gage was also adhered in the vicinity of FBG sensor to measure the strain as well. The shifts of waveform along the bending test are shown in Fig 4-37. No significant deformation of spectrum is evident. This shows that the previous impact damage did not induce cracks and damage on the fiber. The founding of the characteristic spectrum in the post-impact fatigue case can only be attributed to non-uniform strain field in the specimen.

In a further test, we soaked the specimen which had undergone a 140cm impact

and 200000 fatigue cycle in acetone for 1 day. Fig. 4-38 compares the spectrum

before and after soaking. Soaking in acetone can soften the matrix and is supposed to

be able to relief most of the residual strain on the fiber. It was found that although the

alteration of spectra did not revert to its initial state, the intensity of other wavelengths

subsided. The result is consistent with our hypothesis that the FBG sensors were only

influenced by the non-uniform strain field in the CFRP structure, and not the cracks

on the fiber.

This phenomenon of intensity increasing in other wavelengths was also found in

tensile test. The specimen without impact was pulled in tension using MTS, and the

strains at various tensile loads were measured from Linear Variable Differential

Transformer (LVDT) displacement. As shown in Fig. 4-39, the waveform shifted as

the tensile load was increased. It could be observed that the waveform just shifted

before the strain was about 3428μ. At 4240μ, it was found that the intensity of the

other wavelengths was increased, and the wavelength peak was shifted as well. At

5126μ, we could observe that the waveform of other wavelength transformed into

corrugated form, Fig. 4-40 shows the spectrum in the wider wavelength span from

1520nm to 1580nm. This waveform of spectrum was also found in Fig.4-21.

Aditionally, as the strain increased to 6062μ, the intensity of other wavelength

reverted to normal state. In the mean time, we could heard that the fracturing sound of
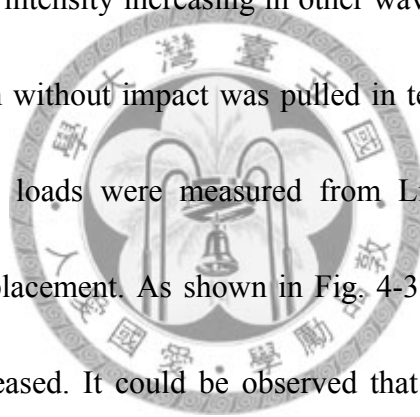
the reinforced fiber. It is possible that the strain was released due to the fracturing of

reinforced fiber, and as a result, the spectra reverted to the a more uniform state

during the tensile test. This result indicates that the intensity increasing of other

wavelength only occurs under a certain strain. Then, we observed from the spectra

that the phenomenon started to take place again as the strain continued to increase to

7047μ. Finally, the reflective peak of FBG sensor almost disappeared at 8031μ, and

became irregular corrugated form. The strain sensitivity of FBG sensor was about

1pm/με. We could see the peak wavelength shifted from about 1550.5nm to 1559nm,

it agrees with the theoretical value. At the strain about 0.008, the fiber was almost

fractured and the effect of FBG sensor became a failure. Fig. 4-41 shows the spectra

at 8031μ in the wavelength span from 1555nm to 1561nm. From the above results, we

acknowledge that the alteration of other wavelength includes the intensity increasing

or became corrugated form. It was proved that when the FBG sensor was under a

certain strain, the other wavelength would change. Compared with the results in

post-impact fatigue test, the post-impact fatigue test induced similar non-uniform

strain, and which caused the spectra to change.

In summery, the phenomenon of intensity increasing in other wavelength might

occur under highly non-uniform strain inside the CFRP specimen. Although the

designed cyclic loading in post-fatigued fatigue test was not as large as the load in

tensile test, the impact damage and the further fatigue test can induce complex

damage condition that lead to highly non-uniform strain, which cause the FBG

sensors to reflect not only the specific wavelength light, but also the light in a wide

span from about 1480nm to 1630nm, as shown in Fig. 4-42. Due to this phenomenon,

it makes the analysis of monitoring for post-impact fatigue damage progressing was

relatively difficult. As a result, for post-impact fatigue damage monitoring applications,

it is necessary to improve the fabrication method of this system to avoid the occurrence

of the intensity increasing in other wavelength.
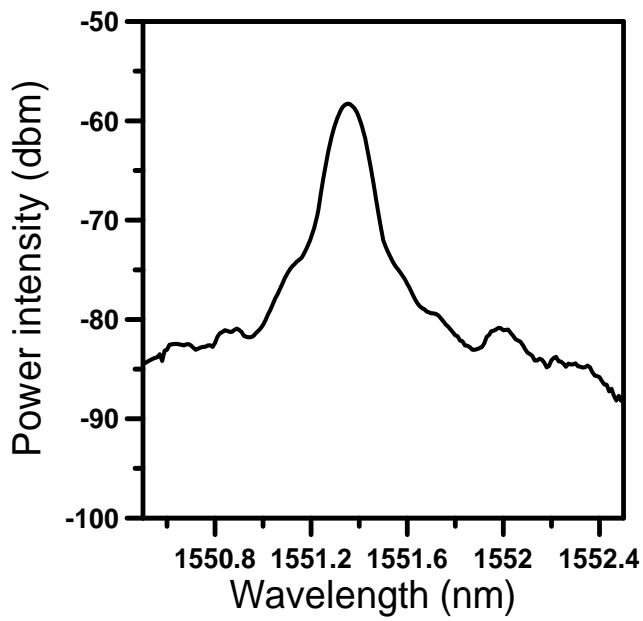
(a)
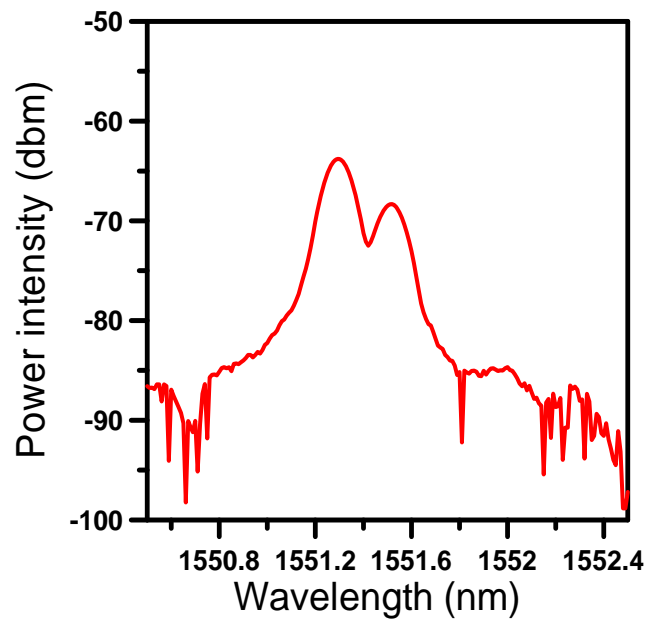
(b)

Fig. 4-1: Comparison of FBG spectra before embedding and after curing. (a) Before embedding (b) After curing.
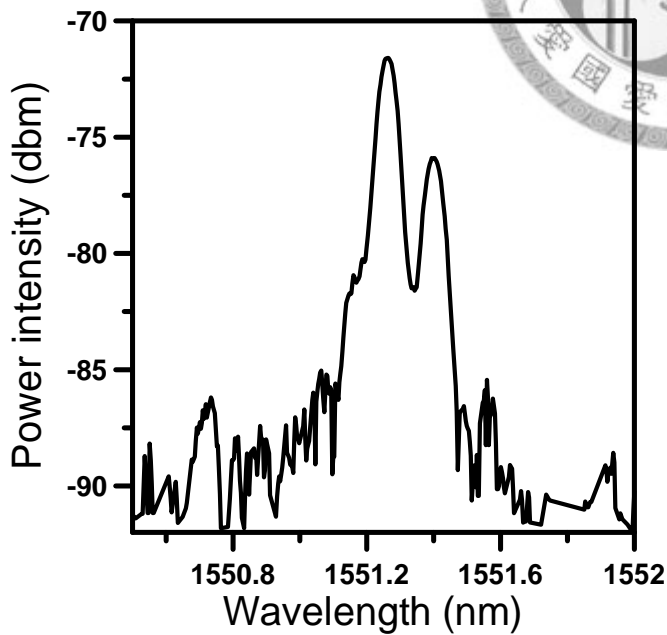
(a)
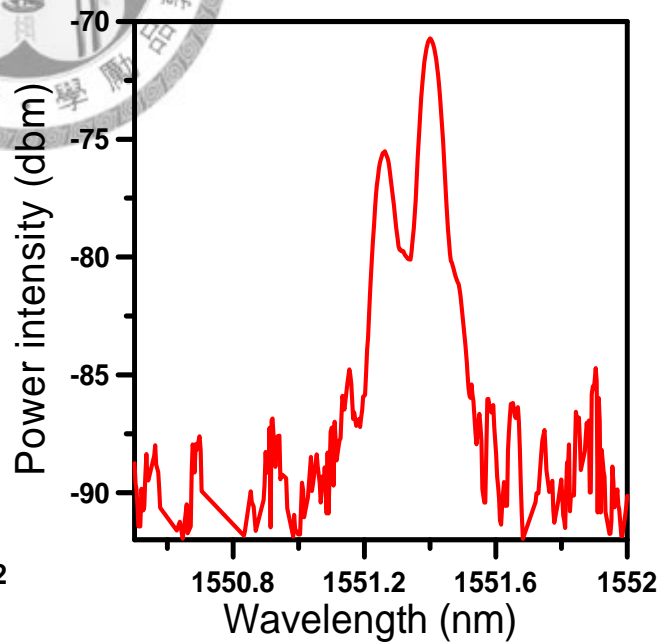
(b)

Fig. 4-2: Energy exchange between two peaks due to birefringence effect. (a) Initial state of the fiber (b) On bending
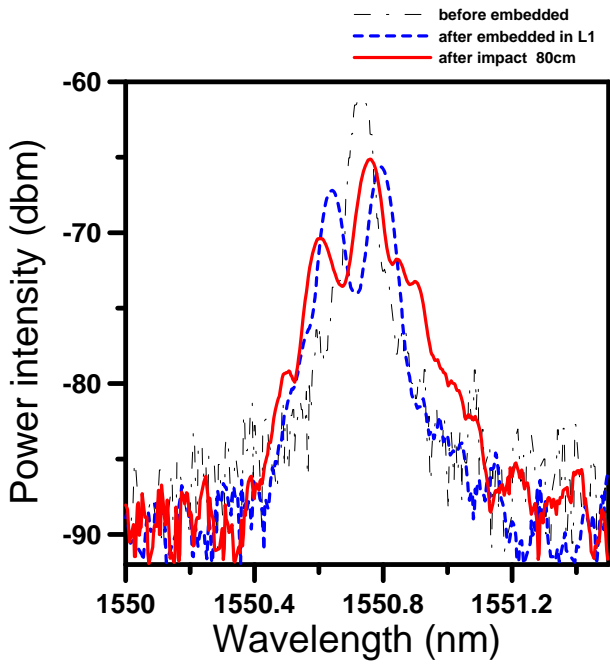
(a) FBG in L1
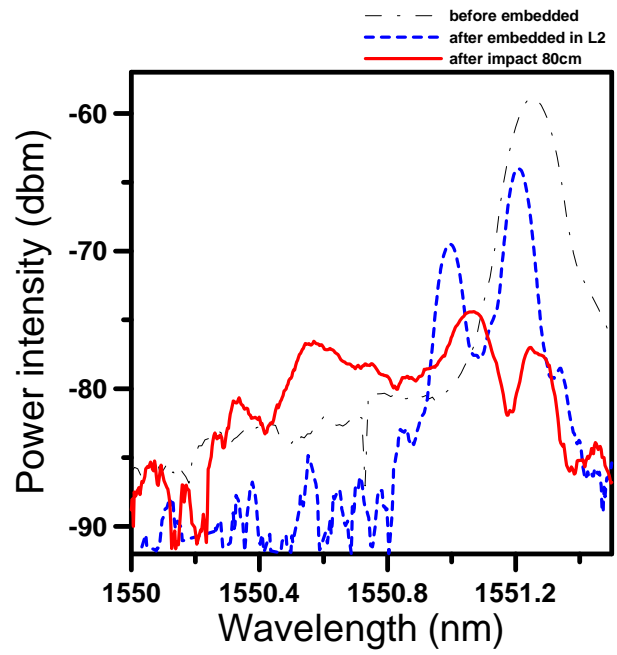
(b) FBG in L2
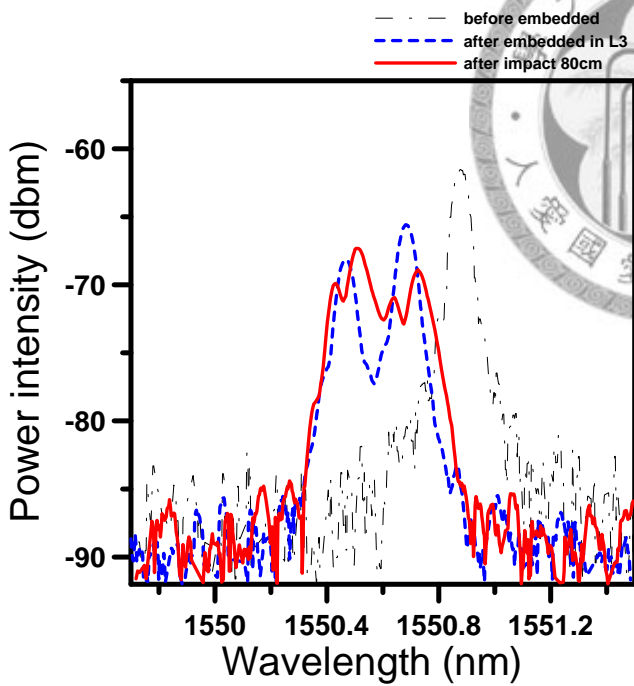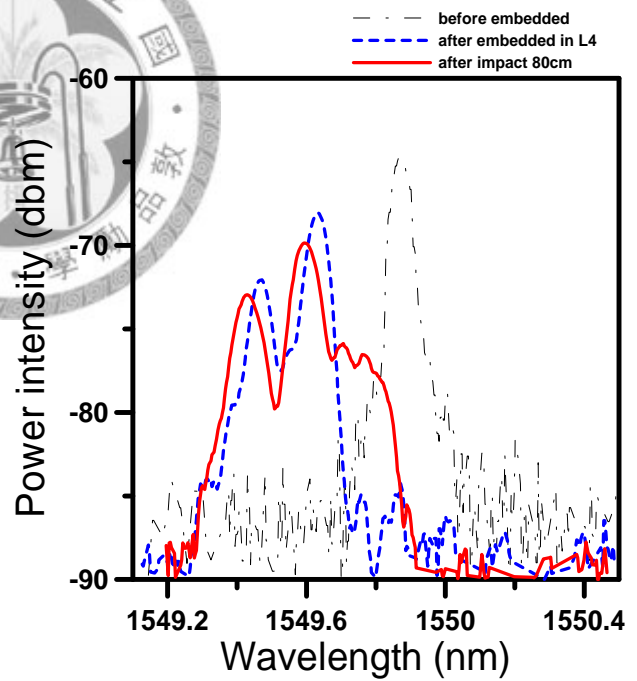
(c) FBG in L3

(d) FBG in L4

Fig. 4-3 (a)-(d): Comparison of spectra from FBG sensors in each layer between before and after impact under a 80cm drop-height.(a) Embedded in L1 (b) Embedded in L2 (c) Embedded in L3 (d) Embedded in L4
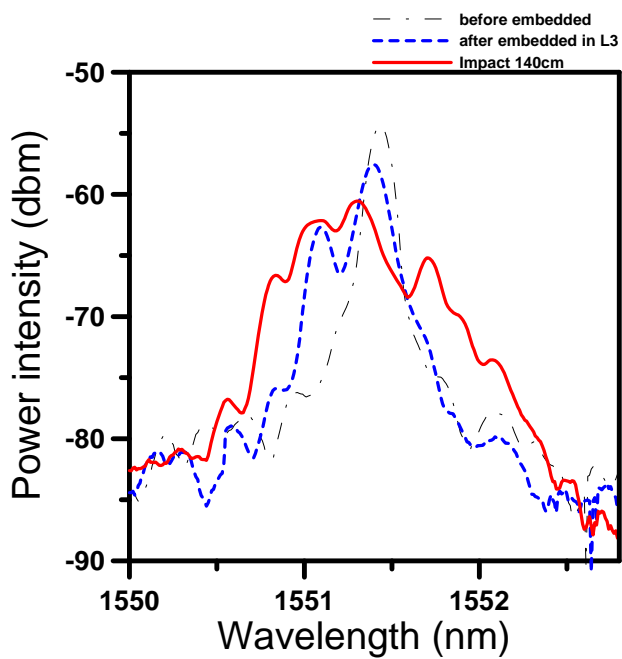
(a) FBG in L1 **(b) FBG in L2**
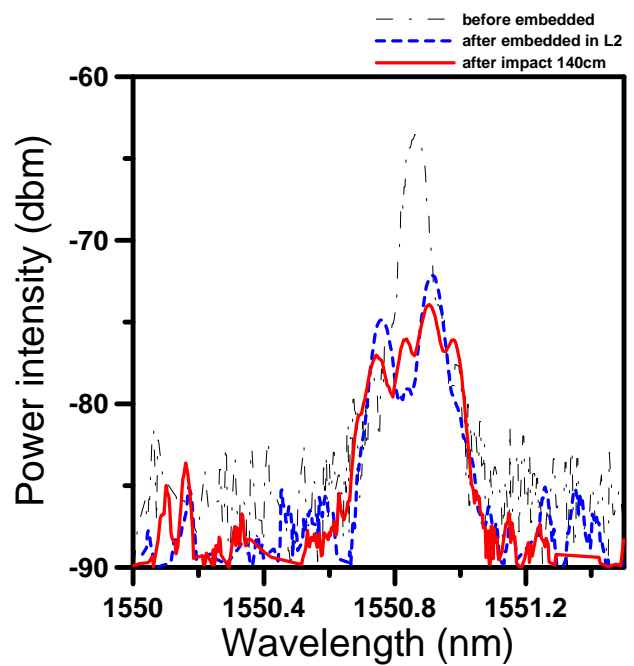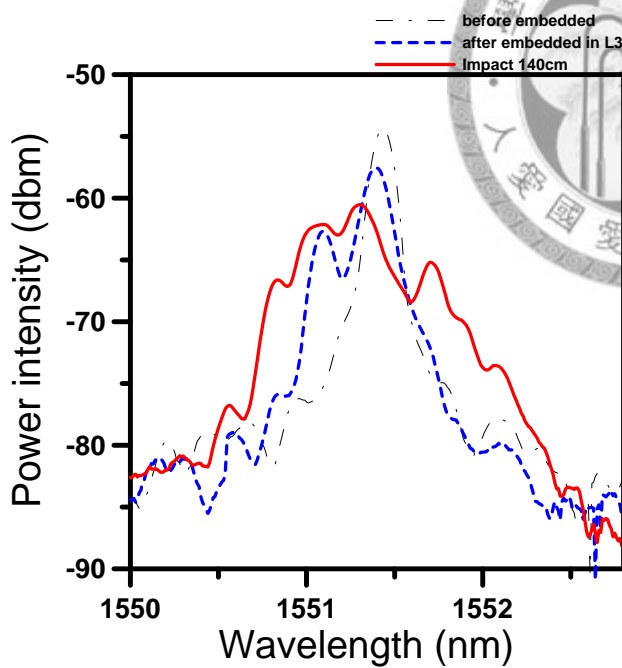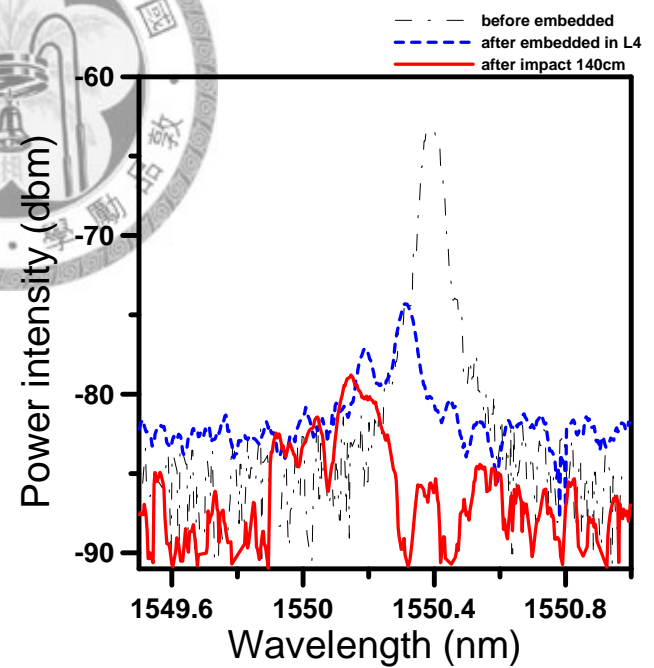
(c) FBG in L3 **(d) FBG in L4**

Fig. 4-4: Comparison of spectra from FBG sensors in each layer between before and after impact under a 140cm drop-height. (a) Embedded in L1 (b) Embedded in L2 (c) Embedded in L3 (d) Embedded in L4
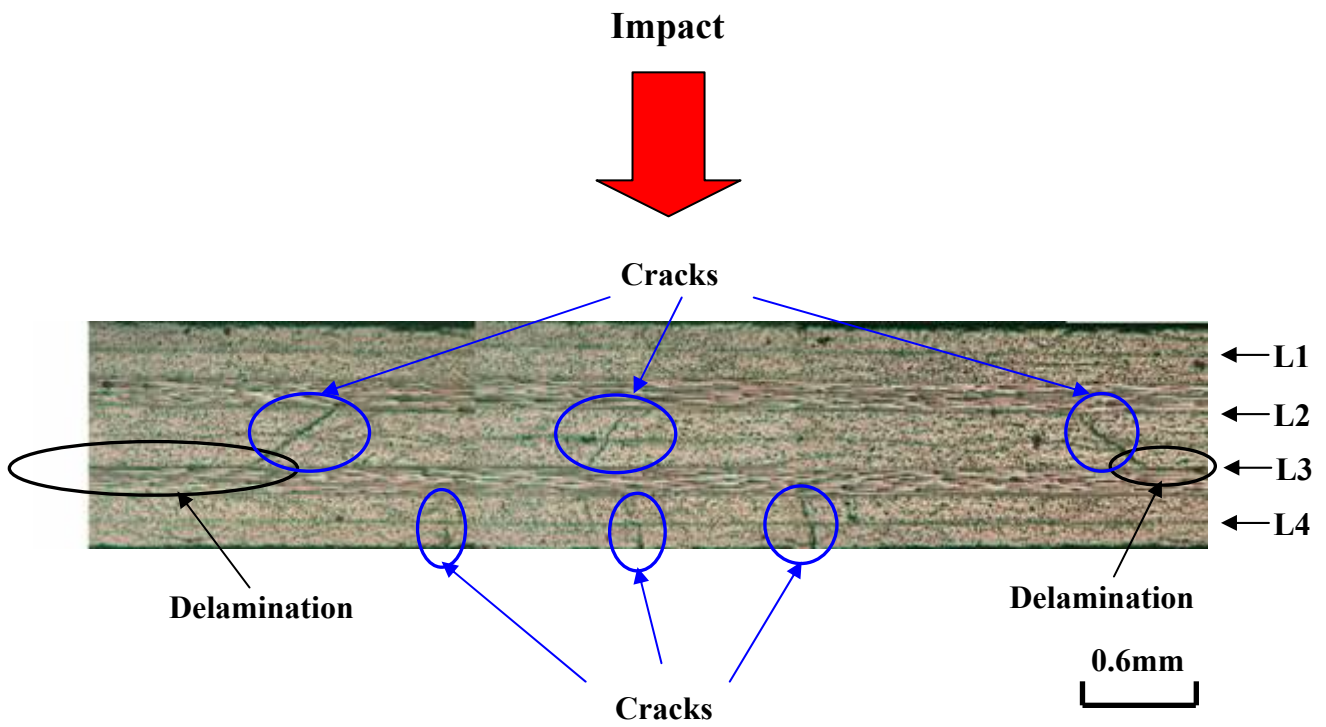
Fig. 4-5: Optical Micrographs of the impact-damaged specimen (drop height 80cm) [32]
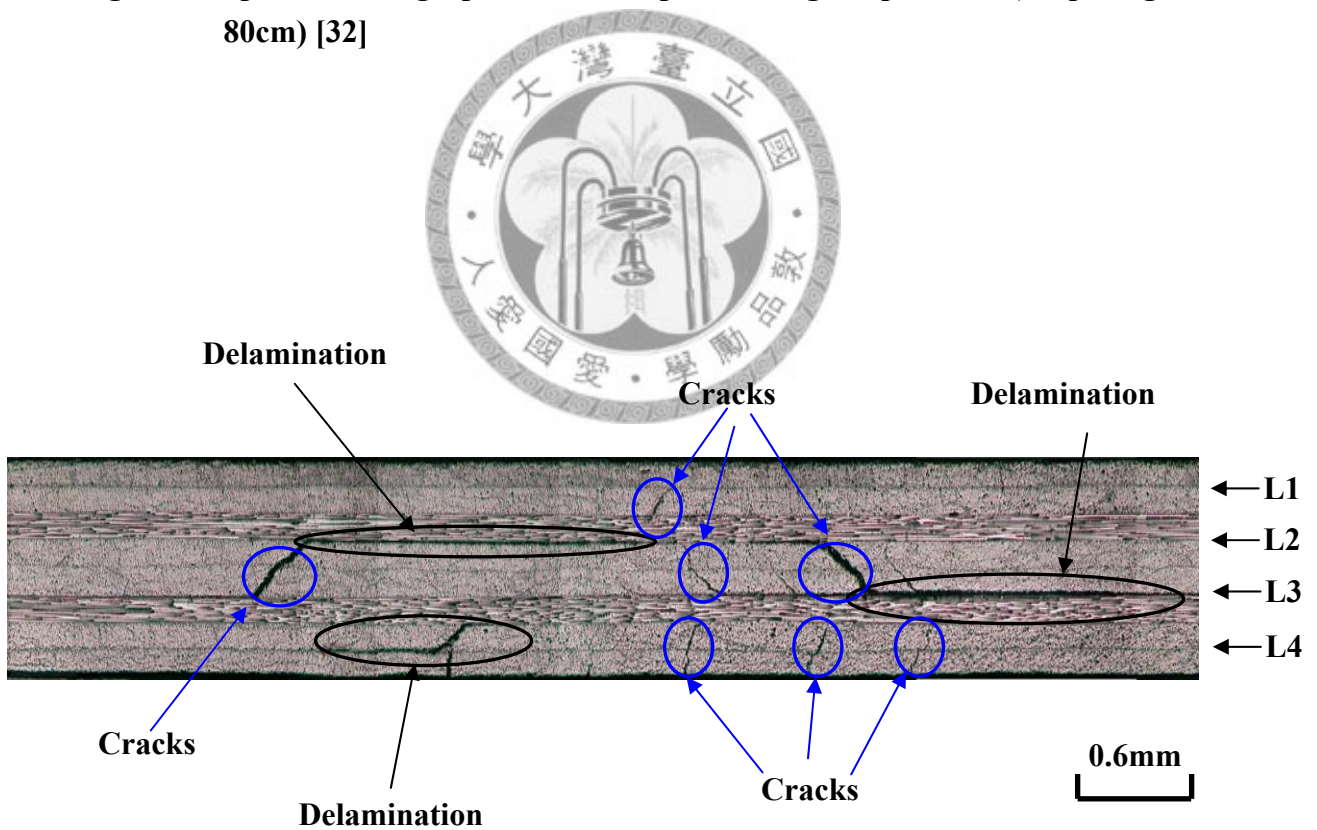
Fig. 4-6: Optical Micrographs of the impact-damaged specimen (drop height 140cm) [32]
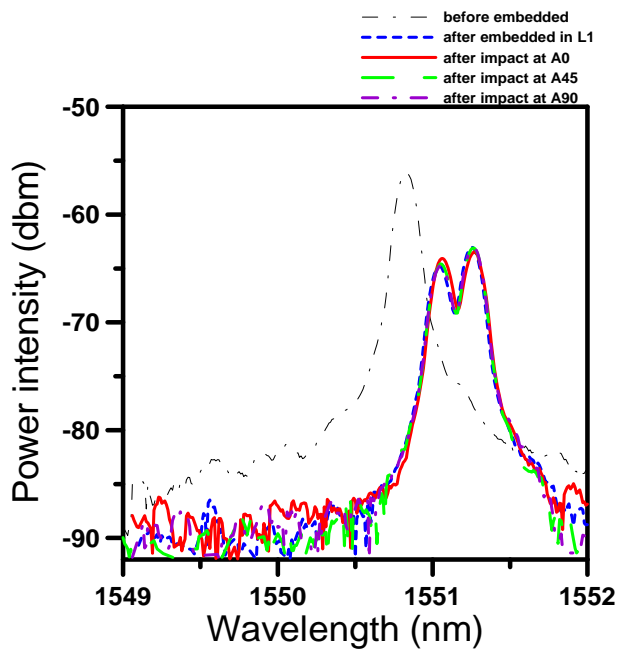
(a) FBG in L1
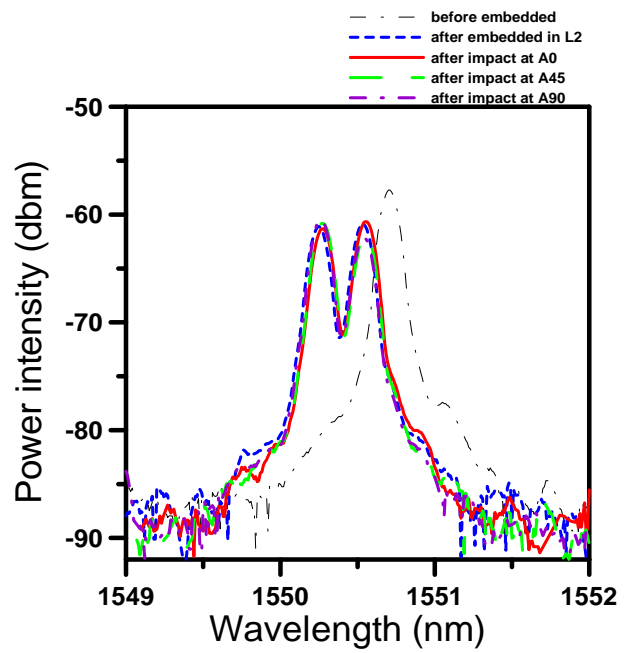
(b) FBG in L2
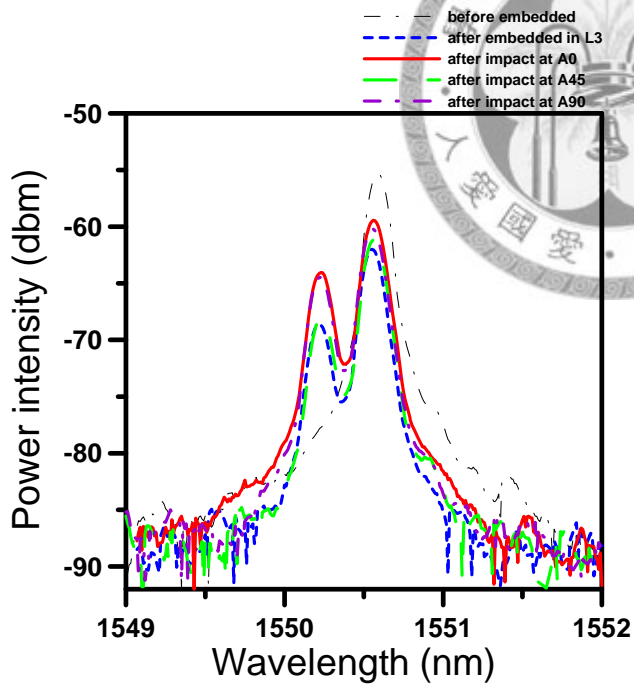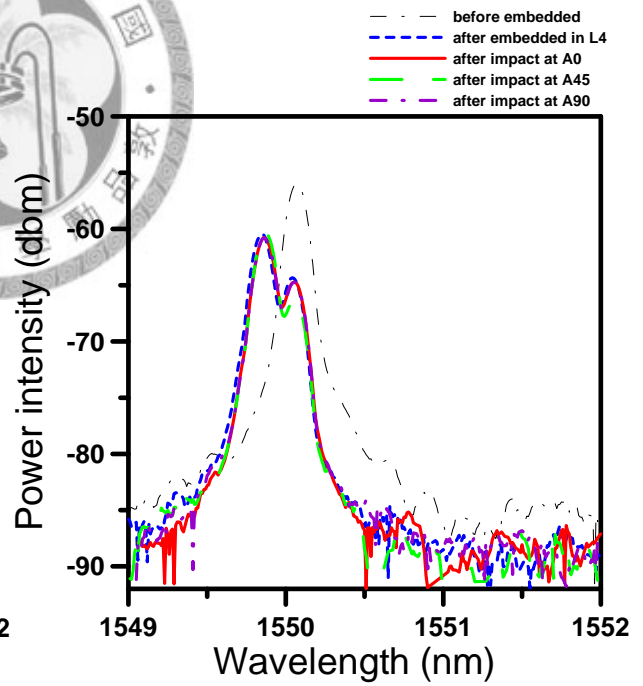
(c) FBG in L3

(d) FBG in L4

Fig. 4-7: Comparison of spectra from FBG sensors in L1 and L2 between before and after impact under a 140cm drop-height.
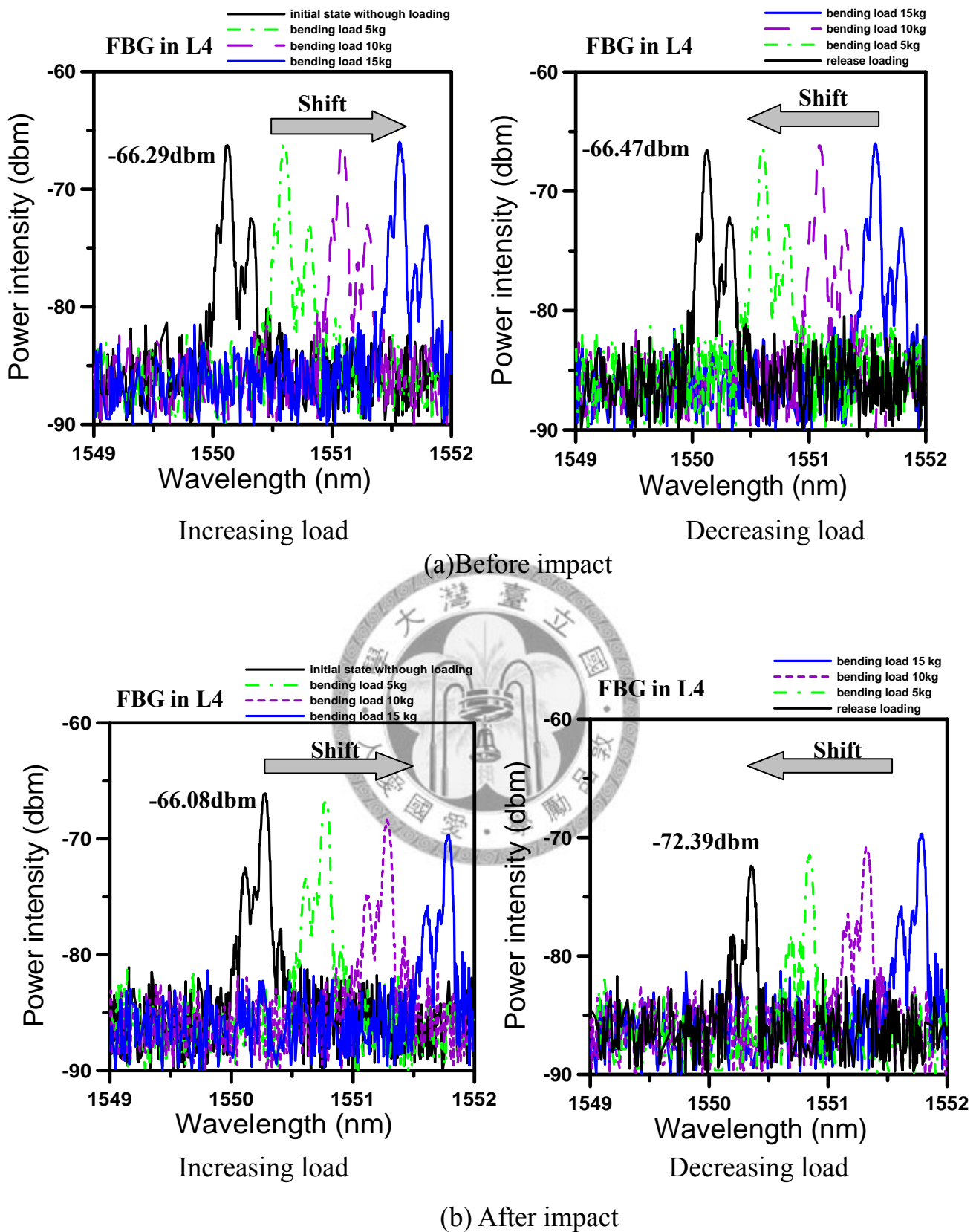
Fig. 4-8: The shifts in wavelength of the spectra from the embedded FBG sensor in L4 before and after impact under 80cm drop height. (a) Before impact (b) After impact at the three impact positions
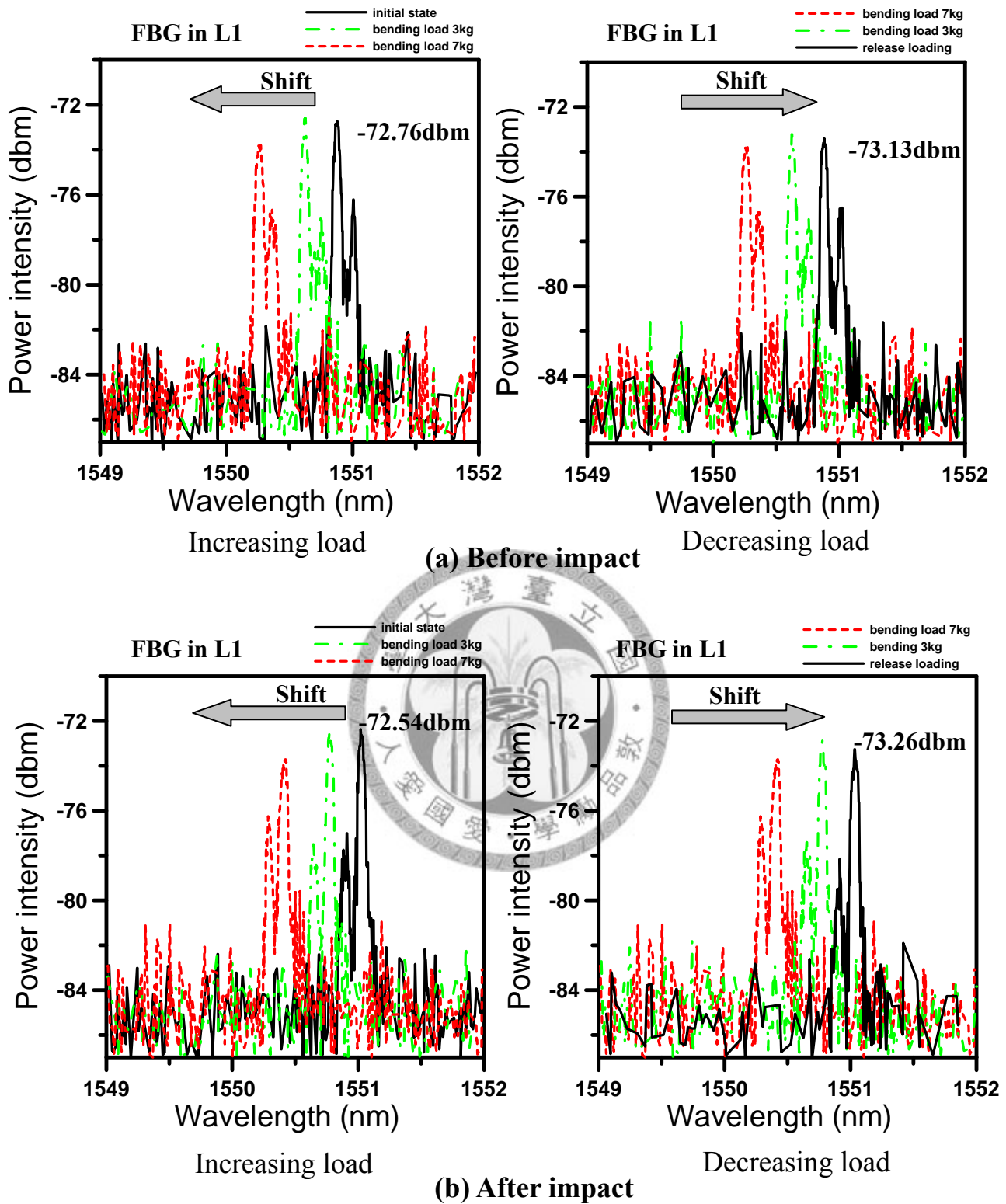
Fig. 4-9: The shifts in wavelength of the spectra from the embedded FBG sensor in L1 before and after impact under 80cm drop height. (a) Before impact (b) After impact at the three impact positions
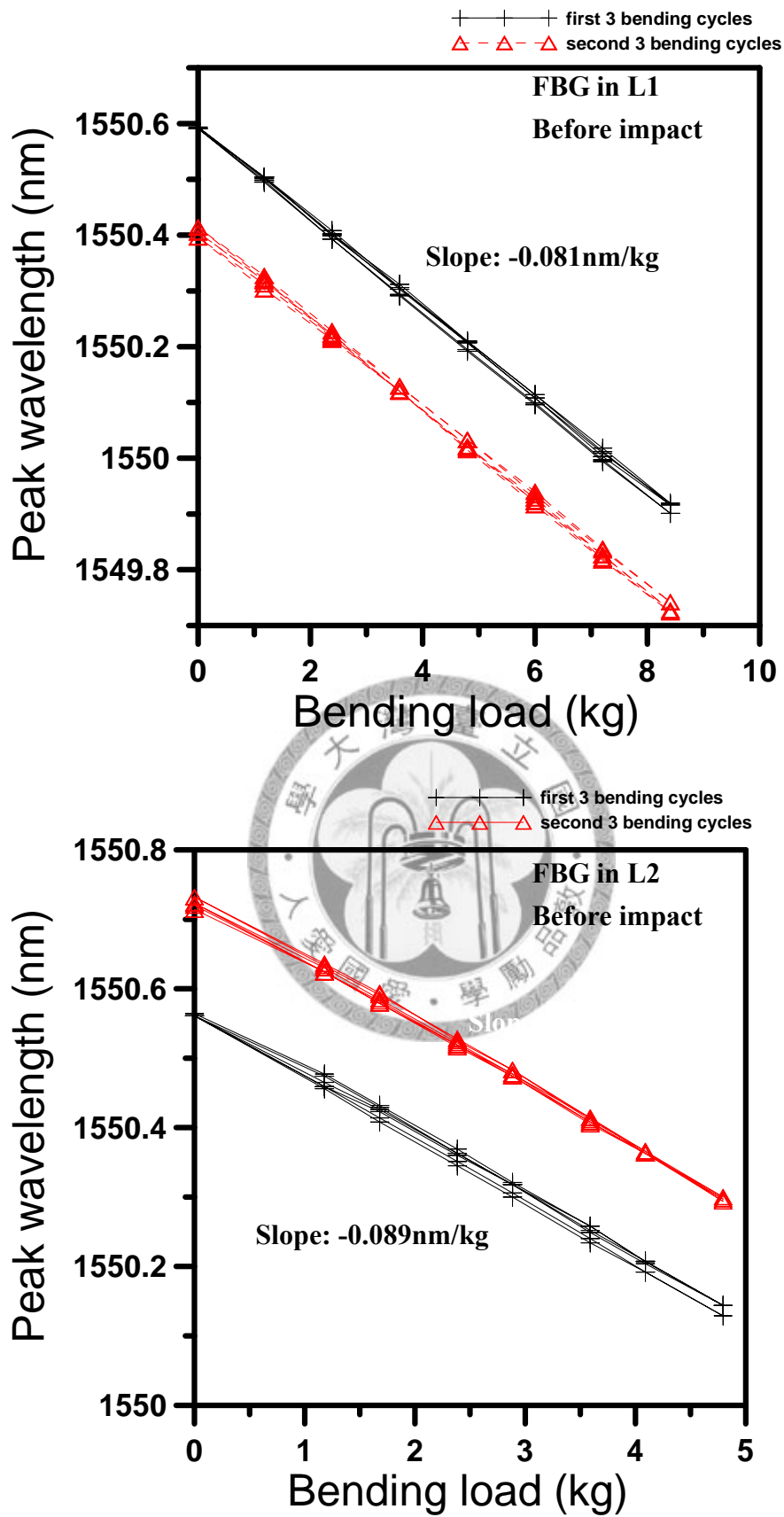
Fig. 4-10 (a): Wavelength shifts from the embedded FBG sensors in L1 and L2 along the bending test before impact.
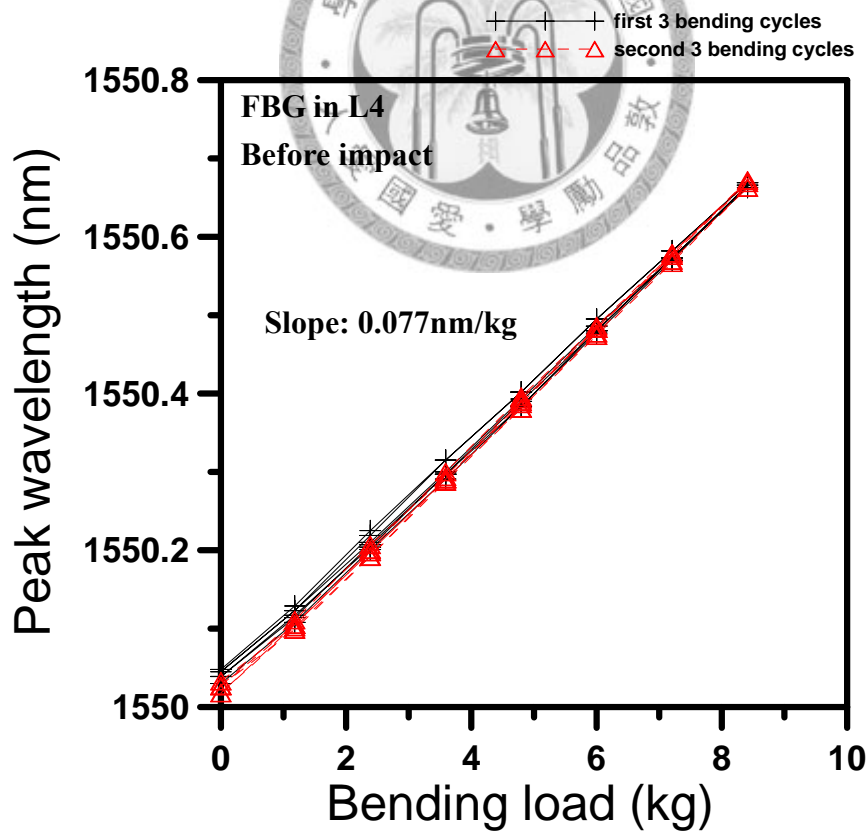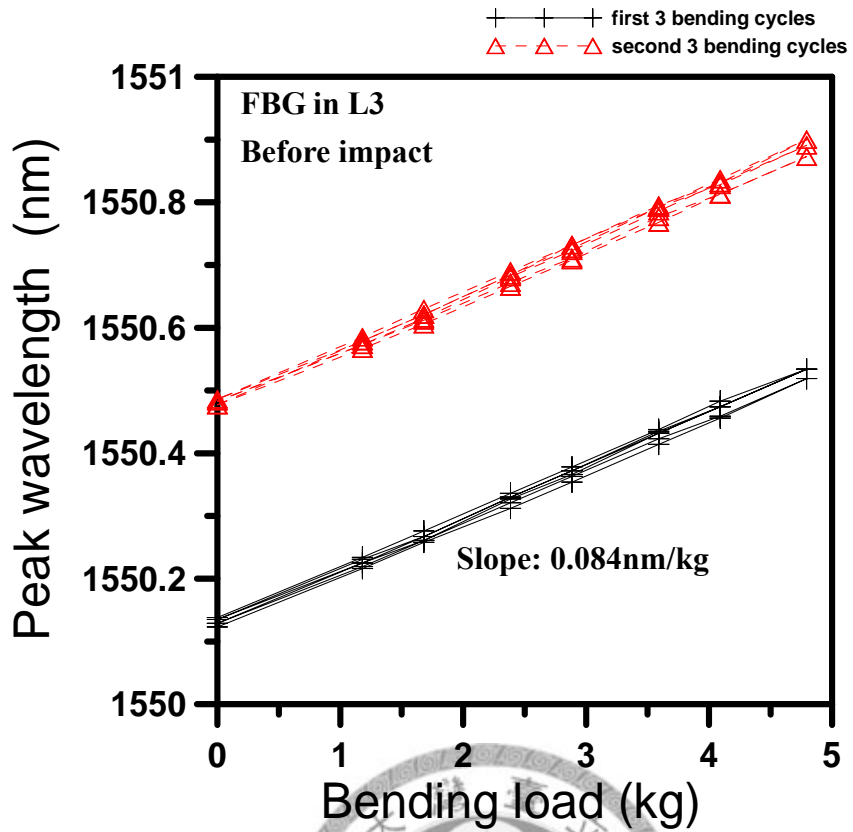
Fig. 4-10 (b): Wavelength shifts from the embedded FBG sensors in L3 and L4 along the bending test before impact.
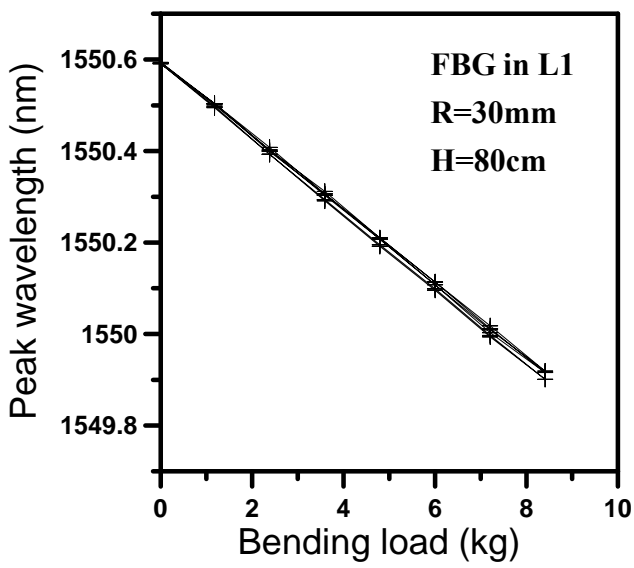
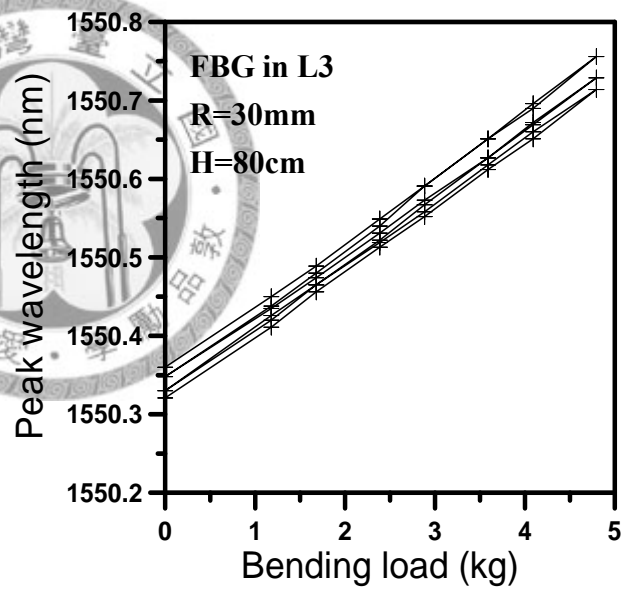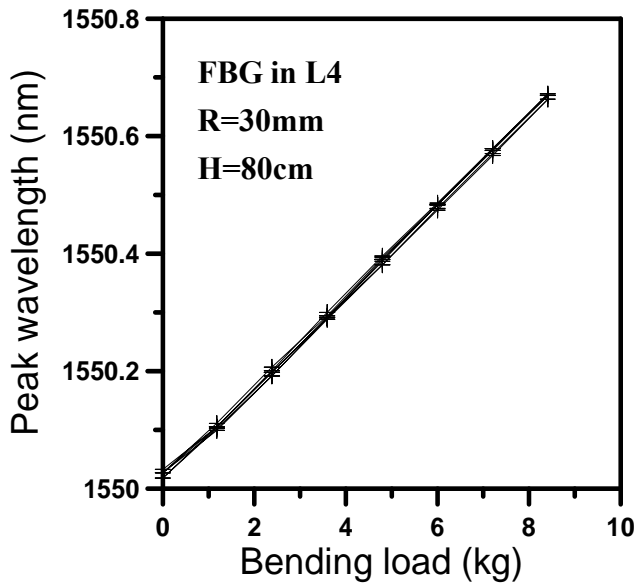Before impact
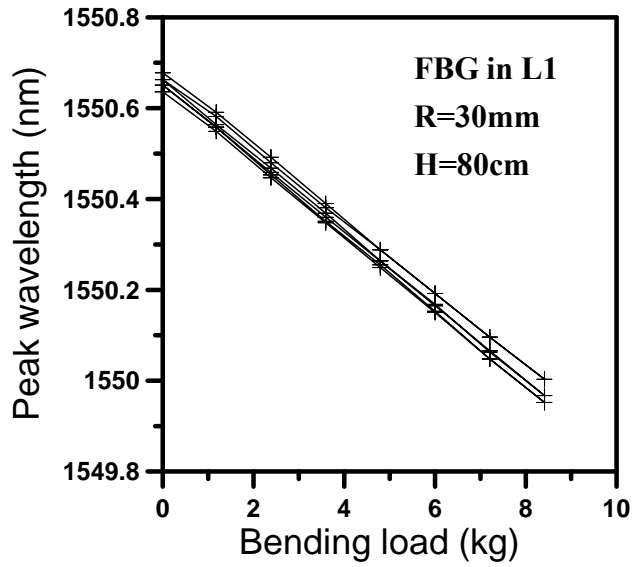
After impact at A0
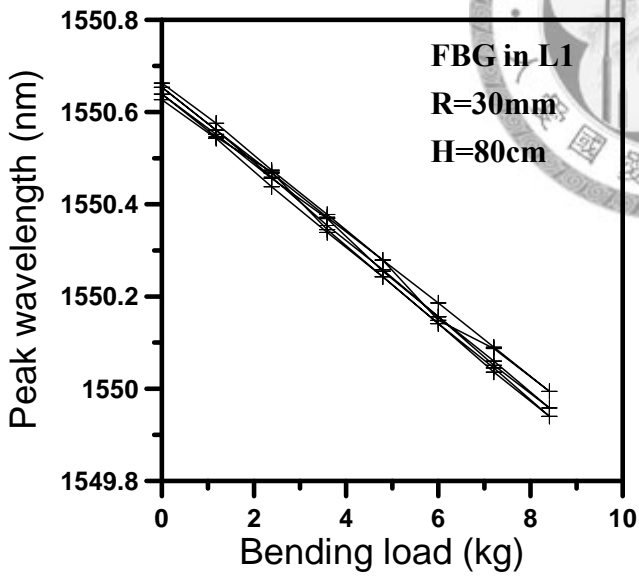
After impact at A0 and A45
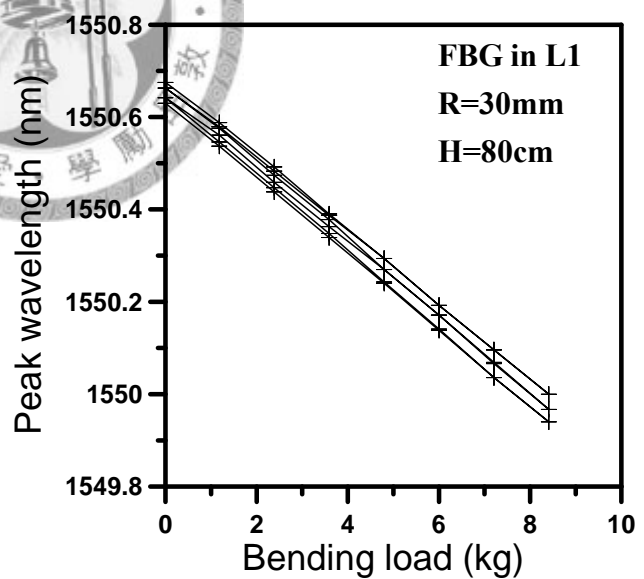
After impact at A0, A45, and A90

Fig. 4-11 (a): Comparison of wavelength shifts from embedded FBG sensor in L1 along a bending test before and after impact under an 80cm drop-height and a distance 30mm away from FBG sensors.
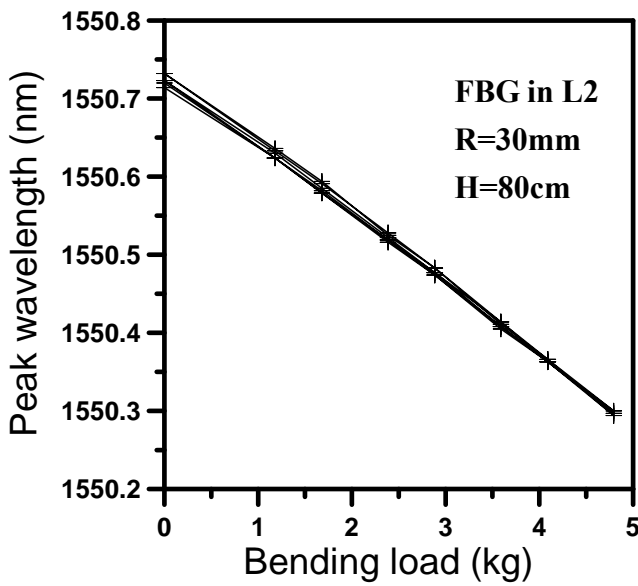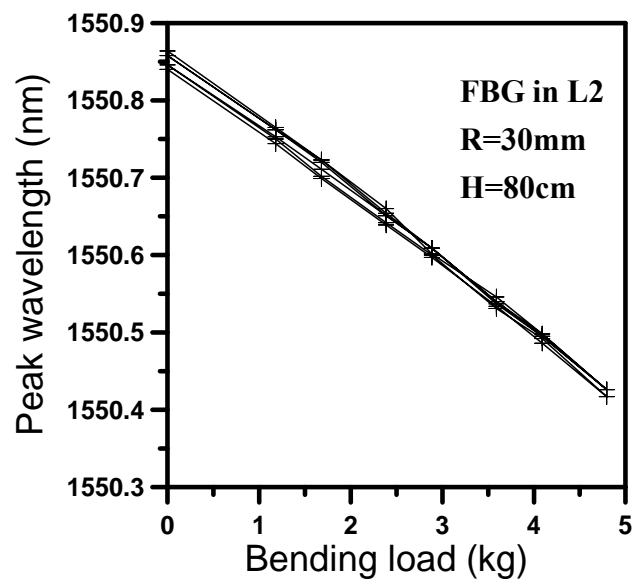
Before impact
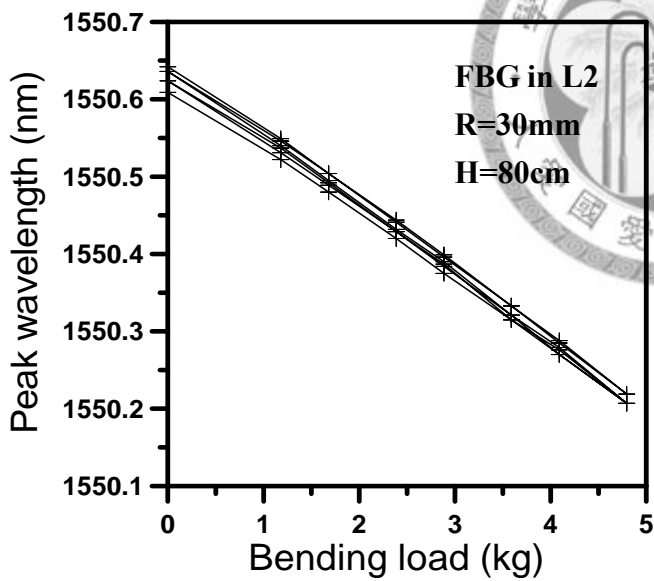
After impact at A0

After impact at A0 and A45
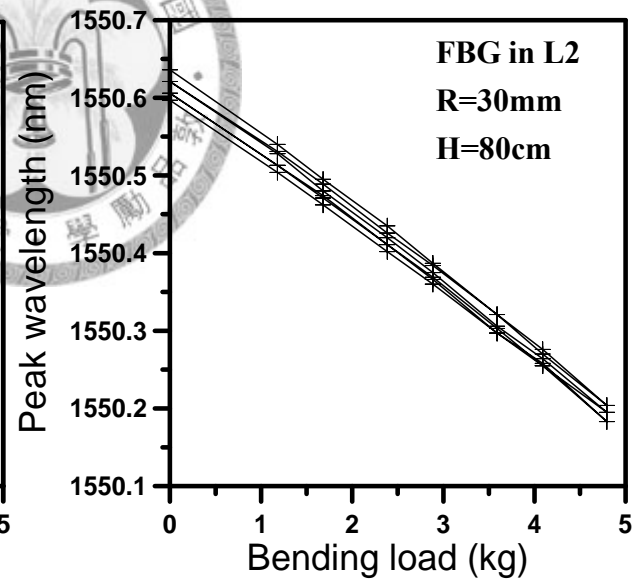
After impact at A0, A45, and A90

Fig. 4-11 (b): Comparison of wavelength shifts from embedded FBG sensor in L2 along bending test before and after impact under an 80cm drop height and a distance 30mm away from FBG sensors.
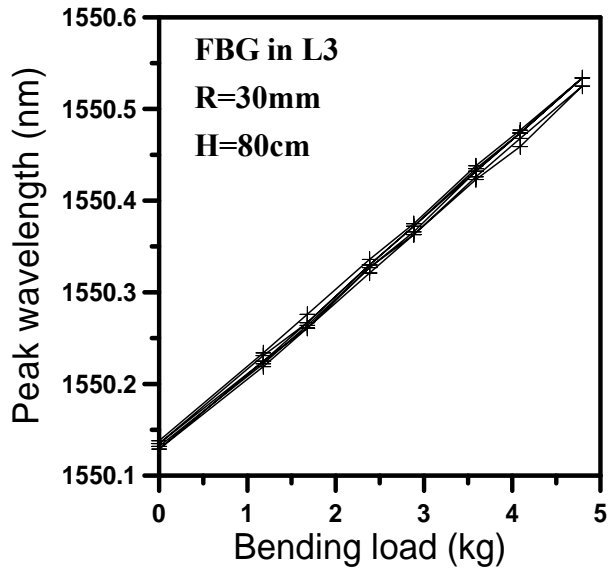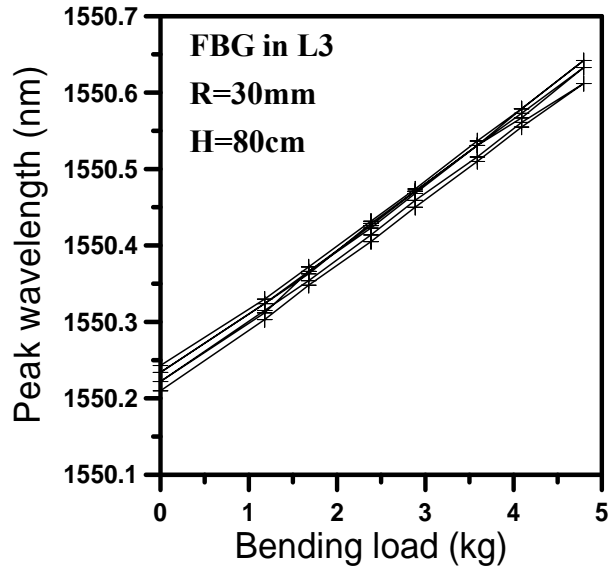
Before impact
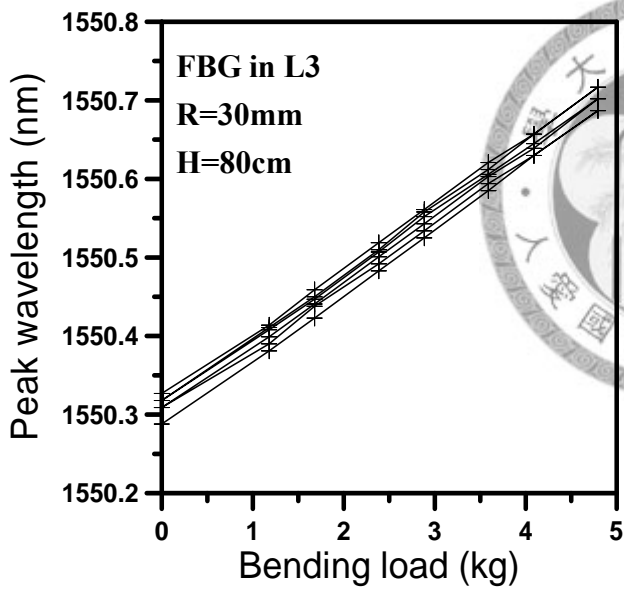
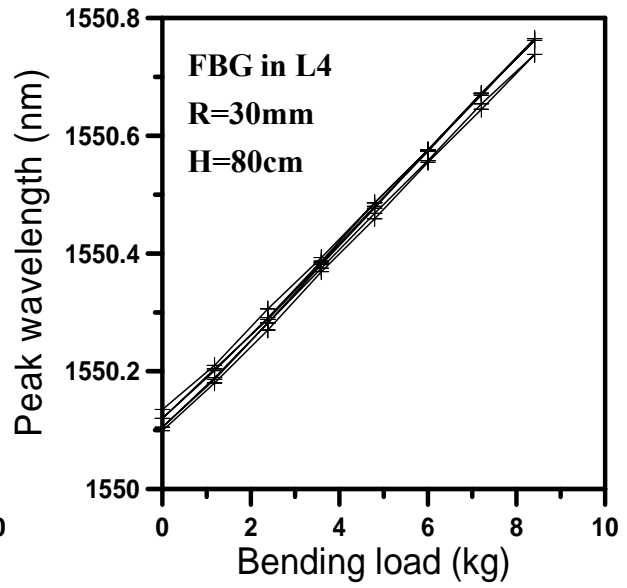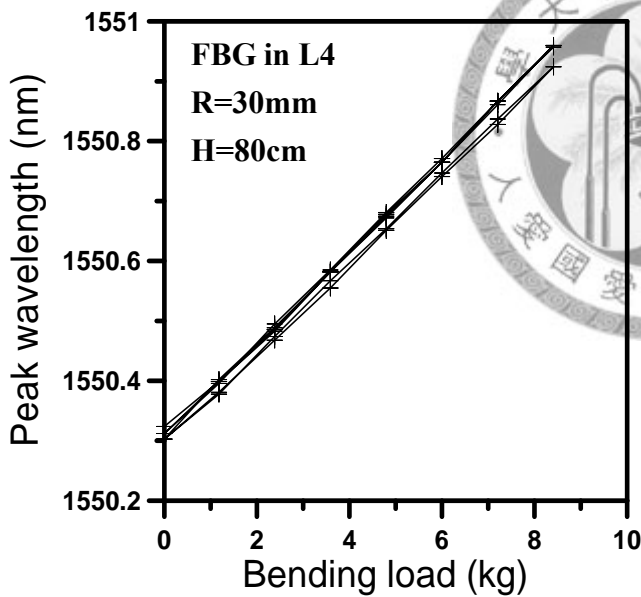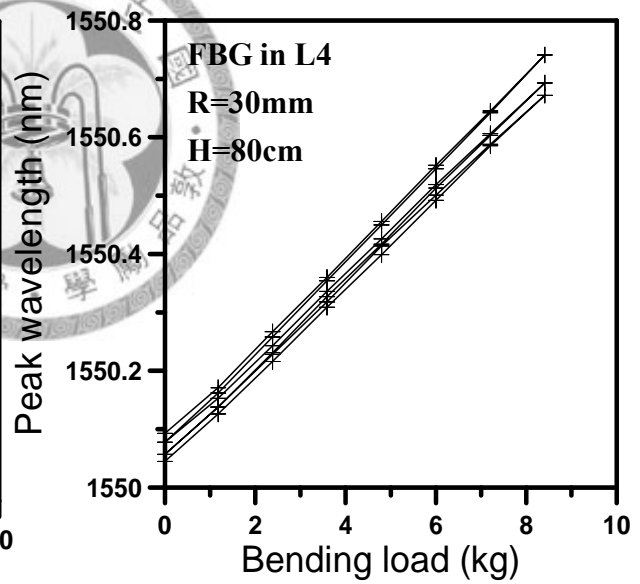After impact at A0

After impact at A0 and A45

After impact at A0,
A45, and A90

Fig. 4-11 (c): Comparison of wavelength shifts from embedded FBG sensor in L3 along bending test before and after impact under an 80cm drop height and a distance 30mm away from FBG
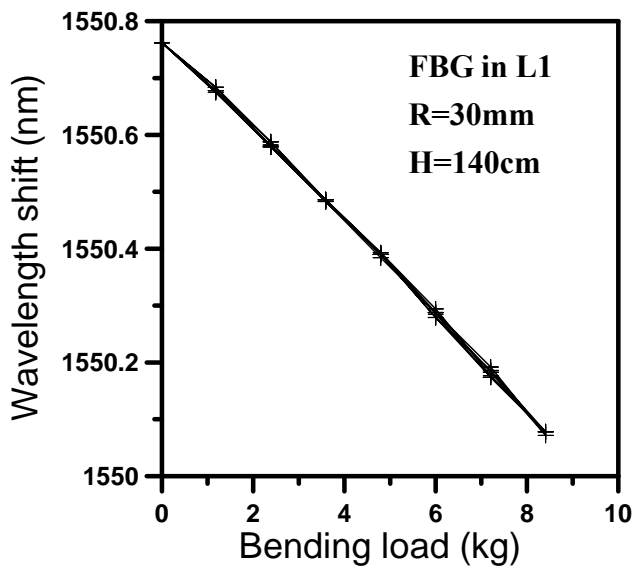
Before impact

After impact at A0
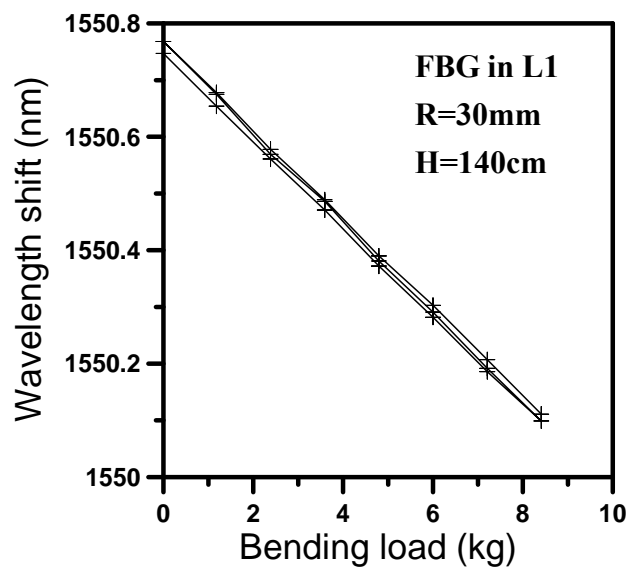
After impact at A0 and A45

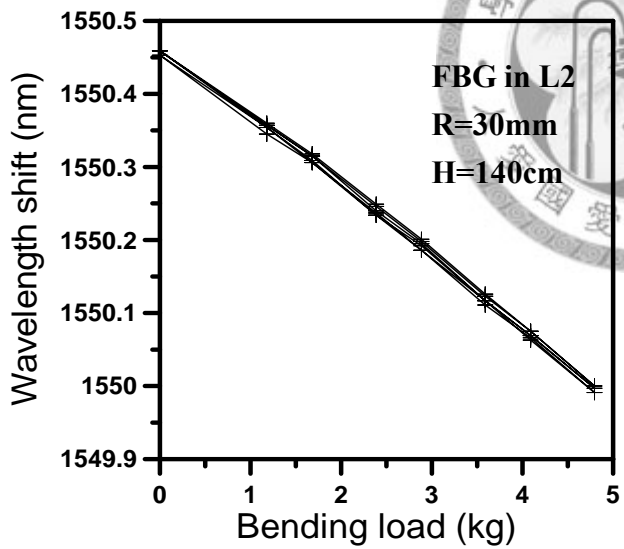**After impact at
A0, A45, and A90**

**Fig. 4-11 (d): Comparison of wavelength shifts from embedded FBG sensor in L4
before and after impact under an 80cm drop height and a distance
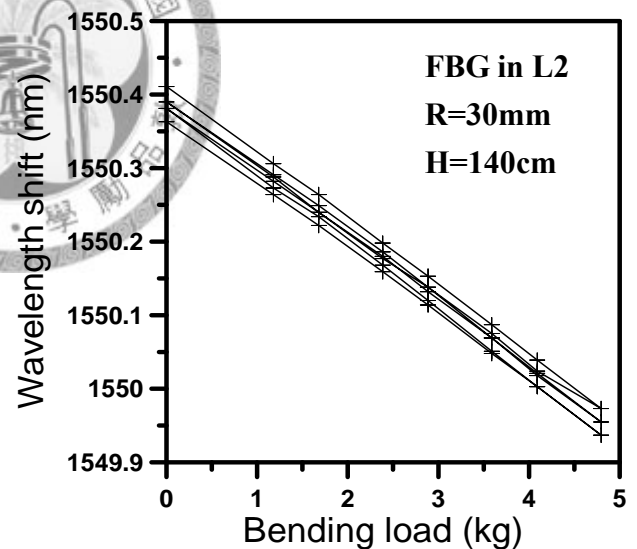30mm away from FBG sensors.**

Before impact

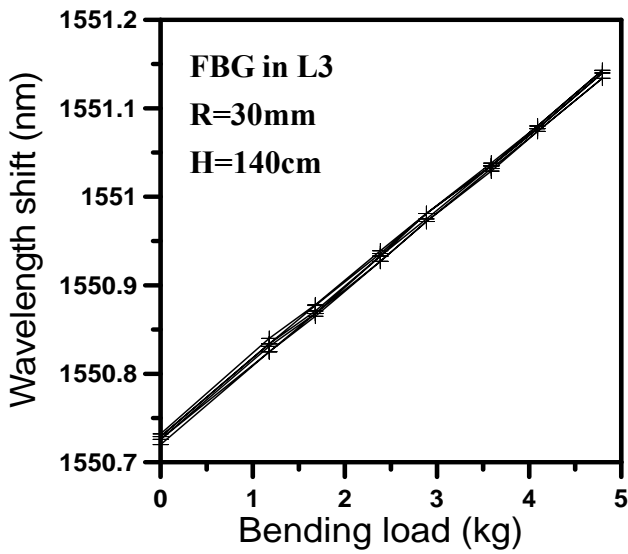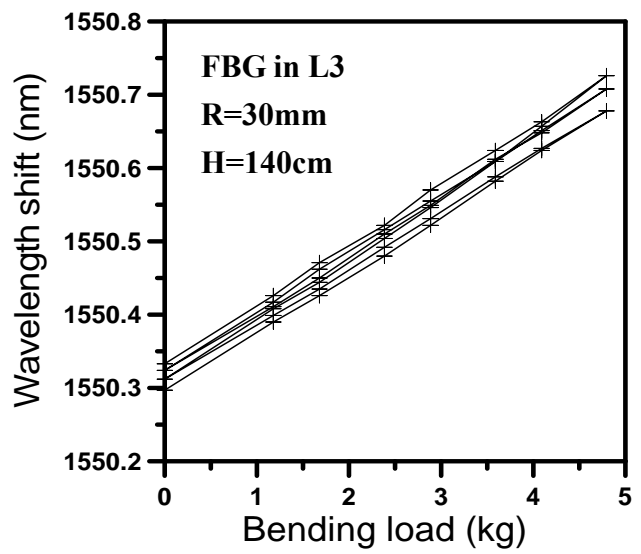After impact at A0, A45 and A90

Before impact

After impact at A0, A45 and A90
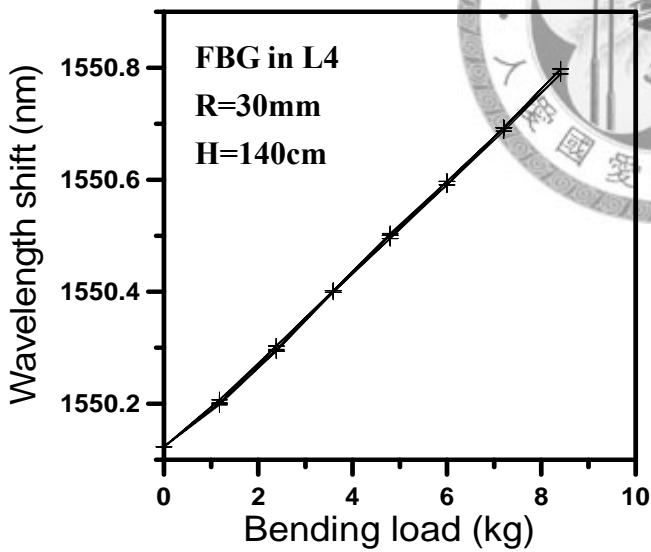
Fig. 4-12 (a): Comparison of wavelength shifts from embedded FBGs in L1 and L2 before and after impact under an 140 cm drop-height and a distance 30mm away from FBG sensors.

Before impact

After impact at A0, A45 and A90

Before impact

After impact at A0, A45 and A90

Fig. 4-12 (b): Comparison of wavelength shifts from embedded FBGs in L3 and L4 before and after impact under a 140cm drop-height and a distance 30mm away from FBG sensors.
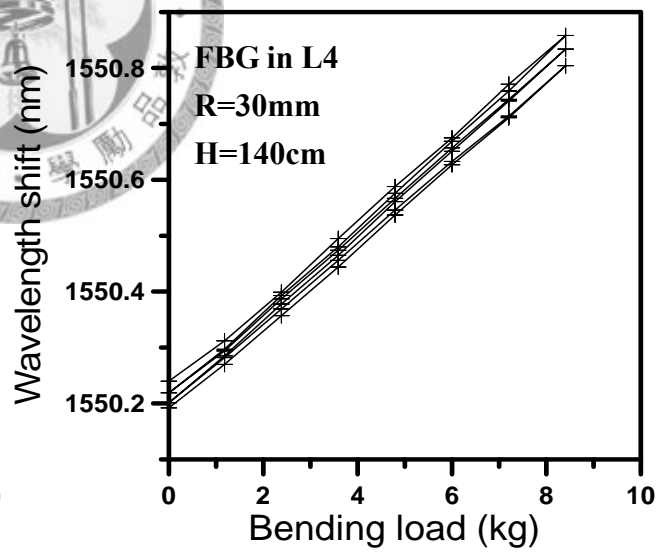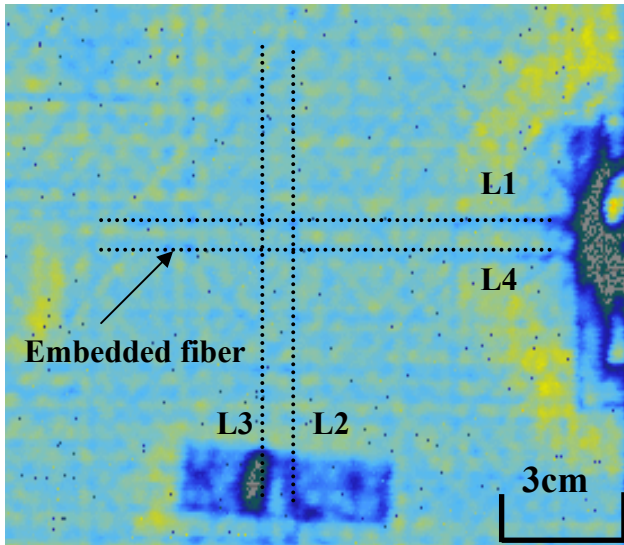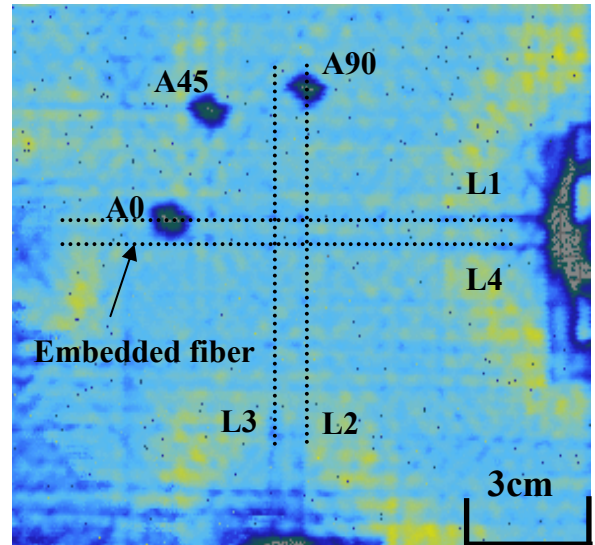
(a) Before impact   **(a) After impact**

Fig. 4-13: Comparison of Ultrasonic C-scan images between before and after impact under a 80cm drop height and a distance 30mm from the FBG sensors. (a) Before impact (b) After impact at A0, A45, and A90.
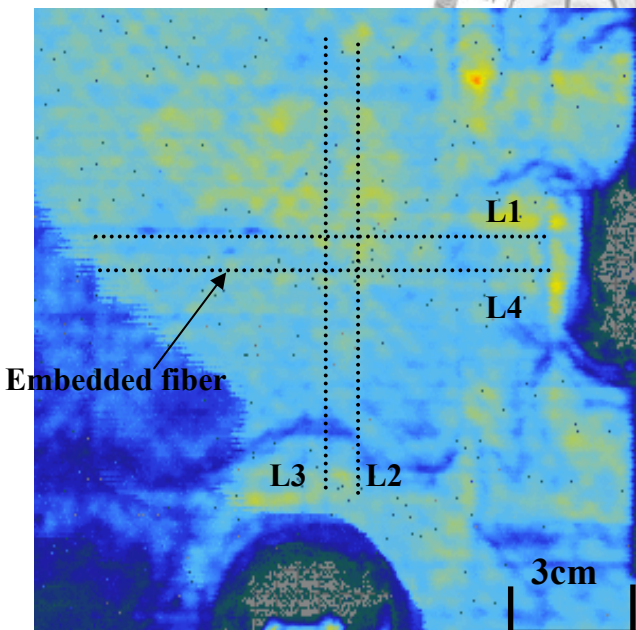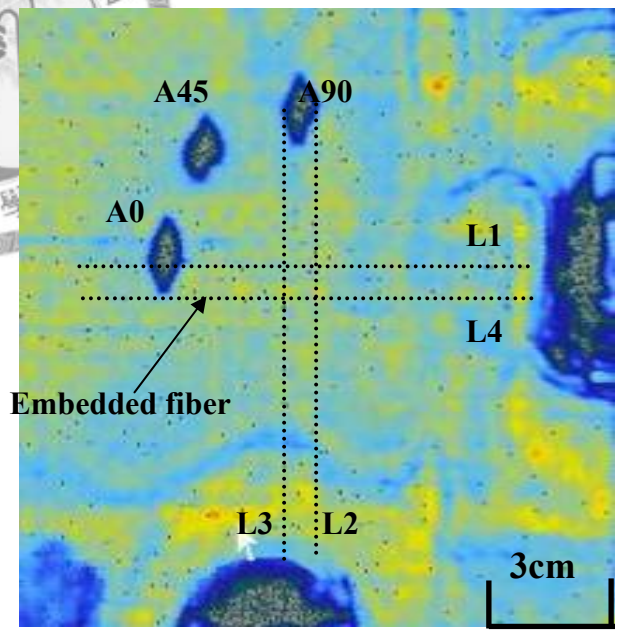

(a) Before impact   **(b) After impact**

Fig. 4-14: Comparison of Ultrasonic C-scan images between before and after impact under a 140cm drop-height and a distance 30mm from the FBG sensors. (a) Before impact (b) After impact at A0, A45, and A90.

Before impact

After impact at A0

After impact at A0 and A45

After impact at A0, A45, and A90

Fig. 4-15 (a): Comparison of wavelength shifts from embedded FBG sensor in L1 along a bending test before and after impact under an 80cm drop height and a distance 50mm away from

Before impact

After impact at A0

After impact at A0 and A45

After impact at A0, A45, and A90

Fig. 4-15 (b): Comparison of wavelength shifts from embedded FBG sensor in L2 along a bending test before and after impact under an 80cm drop height and a distance 50mm away from FBG sensors.

Before impact

After impact at A0

After impact at A0 andA45

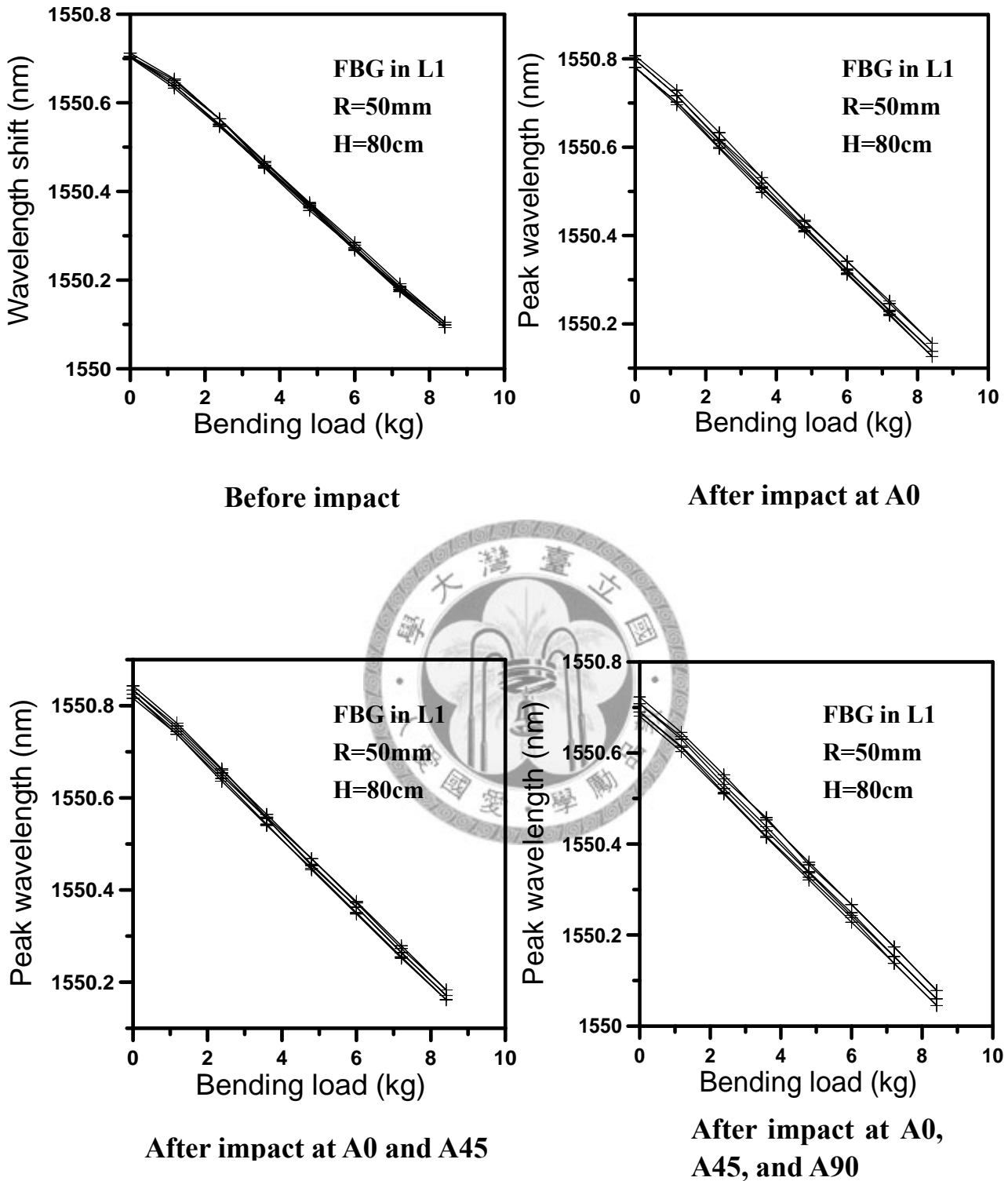**After impact at A0, A45, and A90**

Fig. 4-15 (c): Comparison of wavelength shifts from embedded FBG sensor in L3 along a bending test before and after impact under an 80cm drop height and a distance 50mm away from FBG sensors.

Before impact

After impact at A0

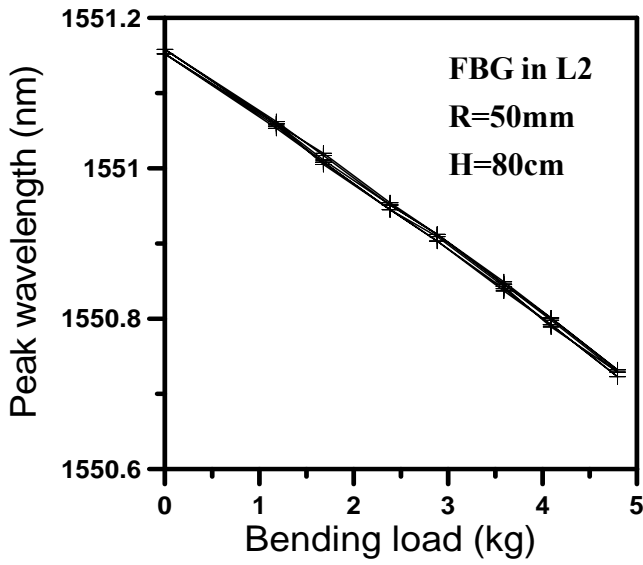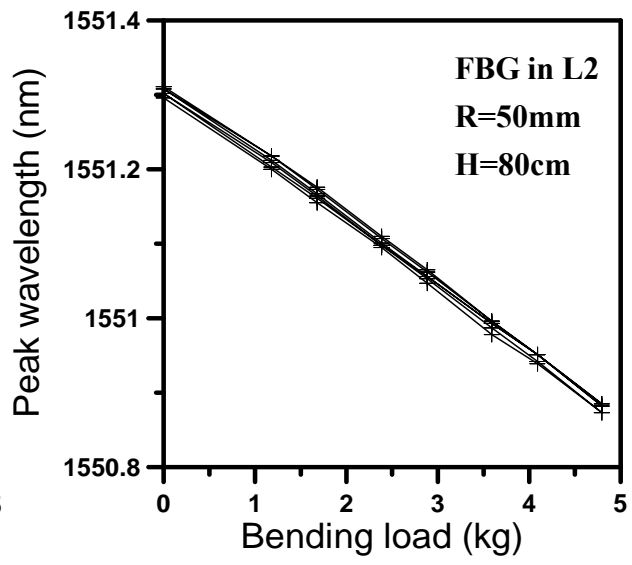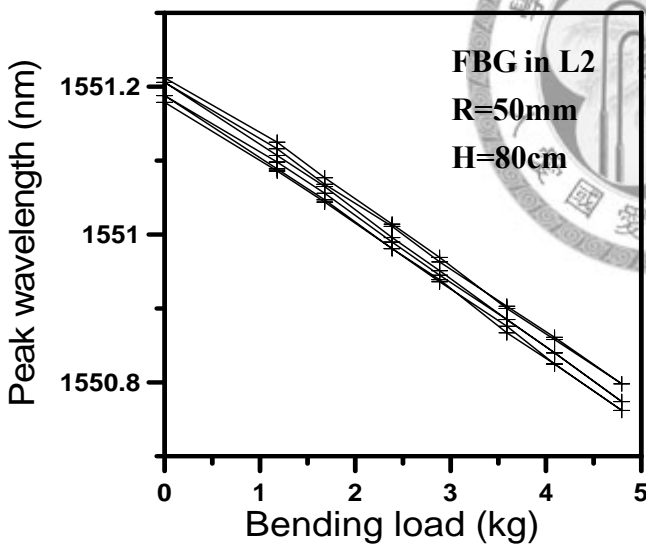**After impact A0 and A45**
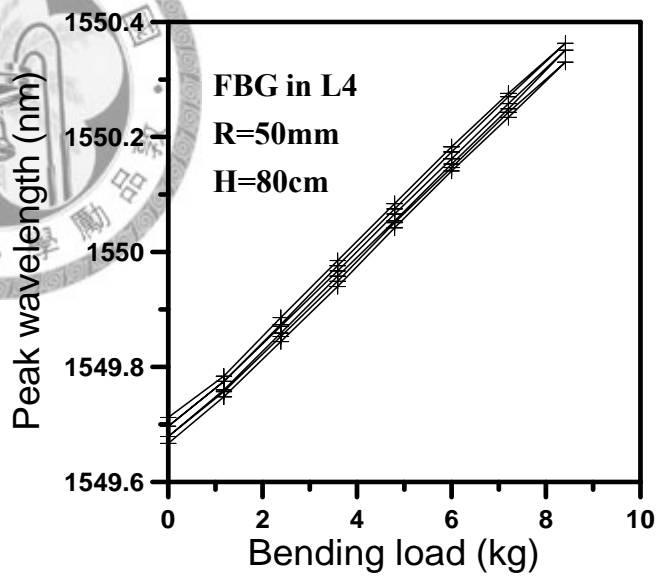
After impact at A0, A45, andA90

Fig. 4-15 (d): Comparison of wavelength shifts from embedded FBG sensor in L4
along a bending test before and after impact under a140cm drop height
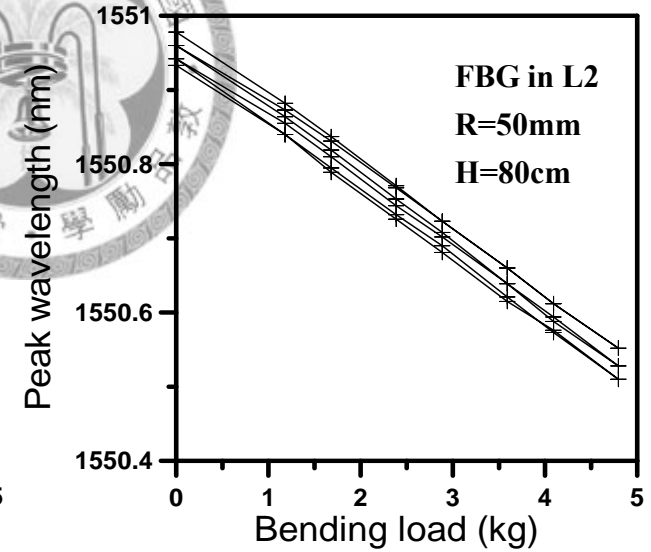and a distance 50mm away from FBG sensors.
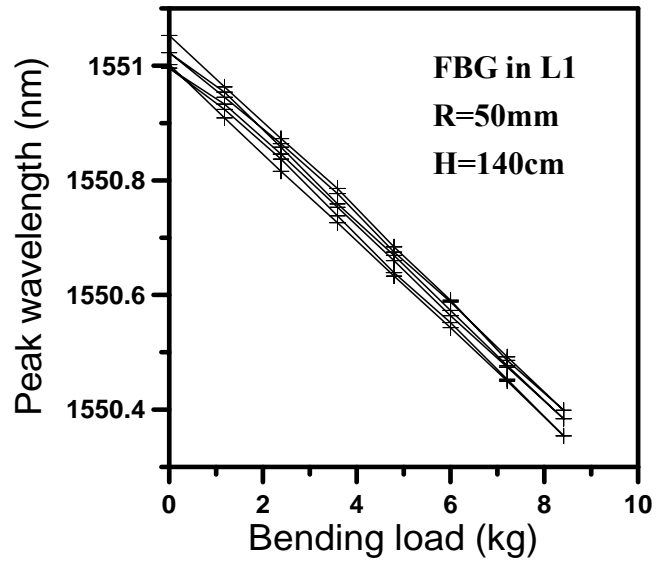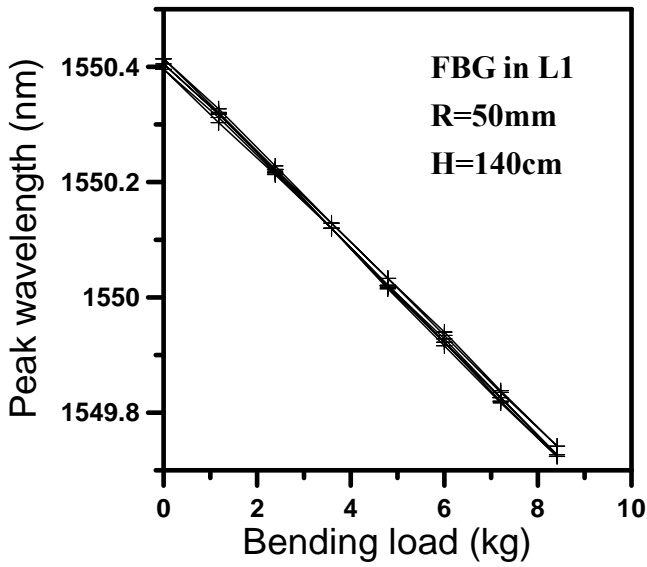
Before impact

After impact at A0, A45, and A90
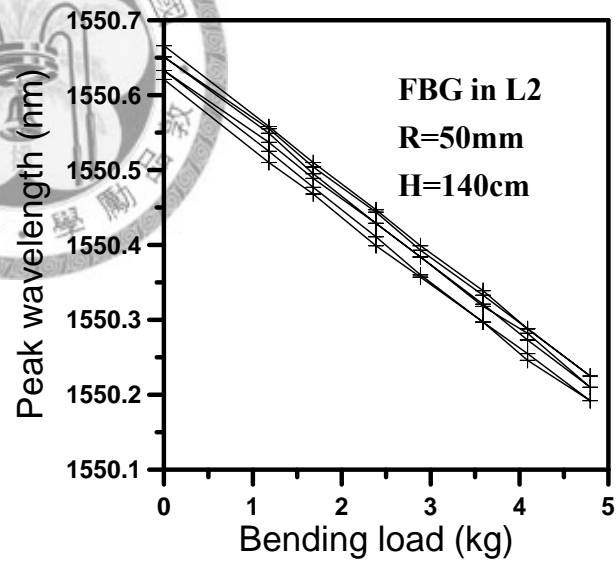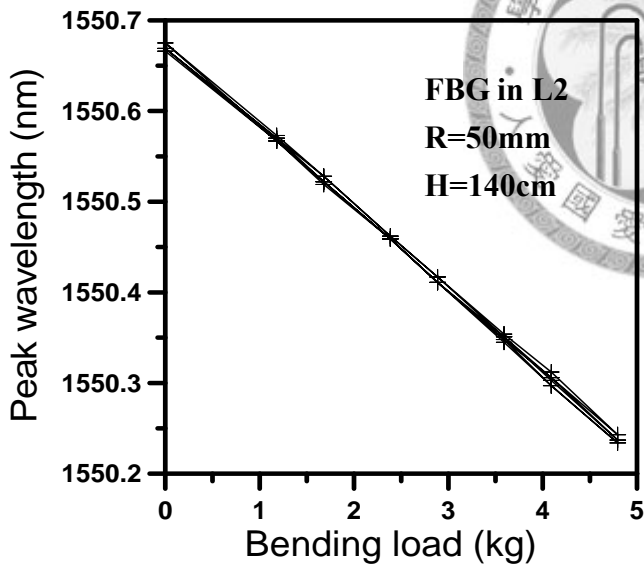
Before impact

After impact at A0, A45, and A90

Fig. 4-16 (a): Comparison of wavelength shifts from embedded FBGs in L1 and
L2 before and after impact under a 140cm drop height and a distance
50mm away from FBG sensors.
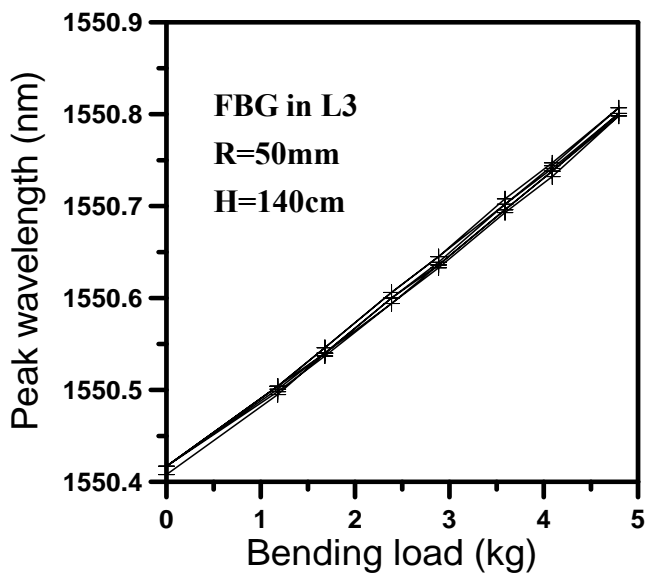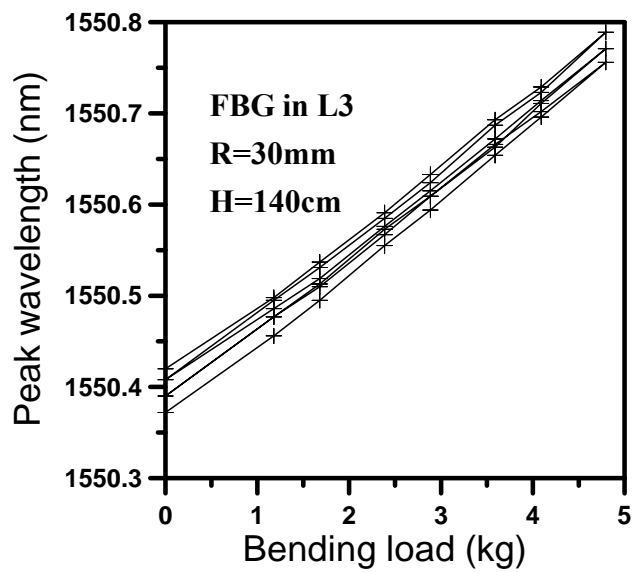
Before impact   **After impact at A0, A45 and A90**
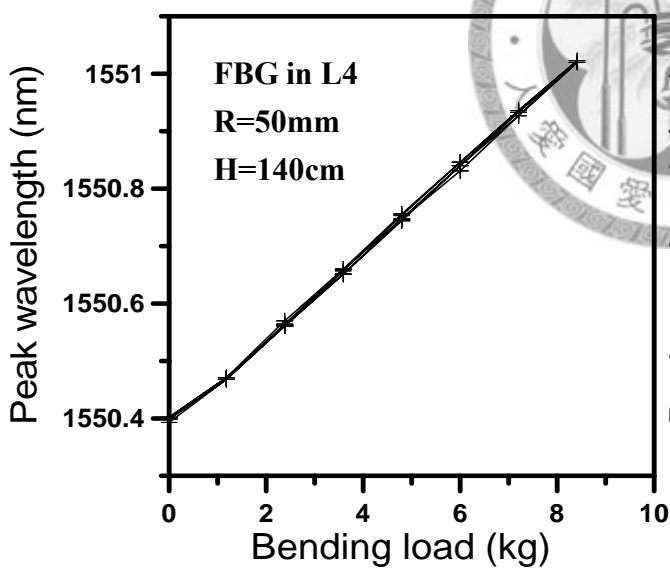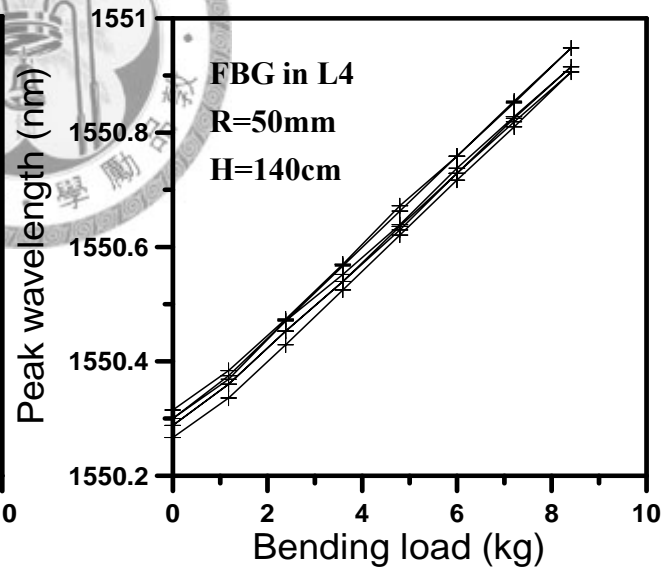
Before impact   **After impact at A0, A45 and A90**

**Fig. 4-16 (b): Comparison of wavelength shifts from embedded FBGs in L3 and
L4 before and after impact under a 140cm drop height and a distance
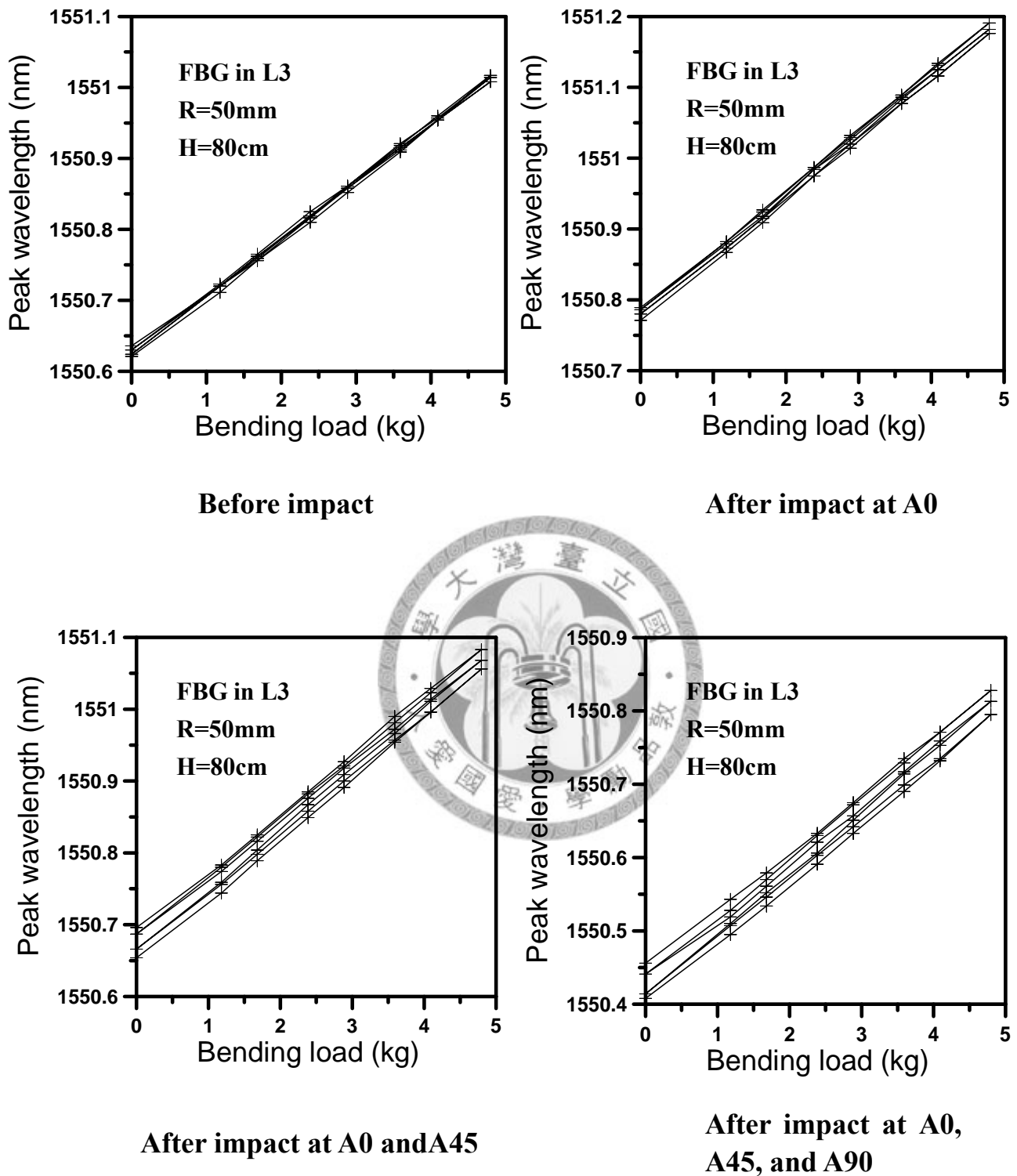50mm away from FBG sensors.**
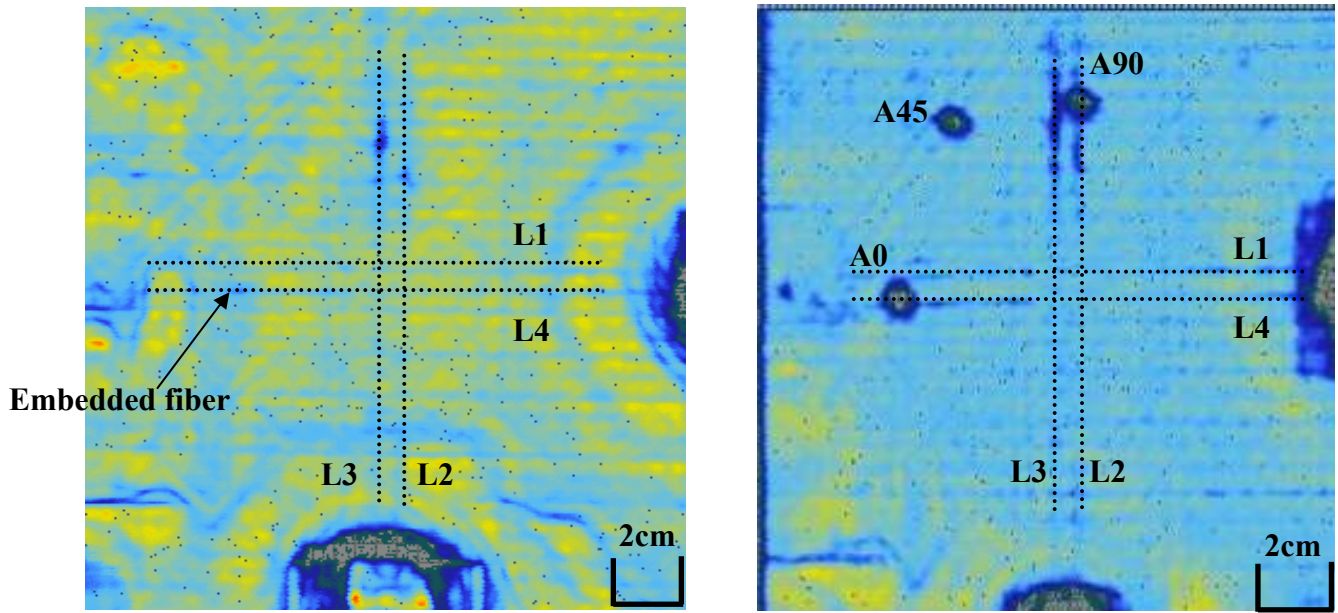
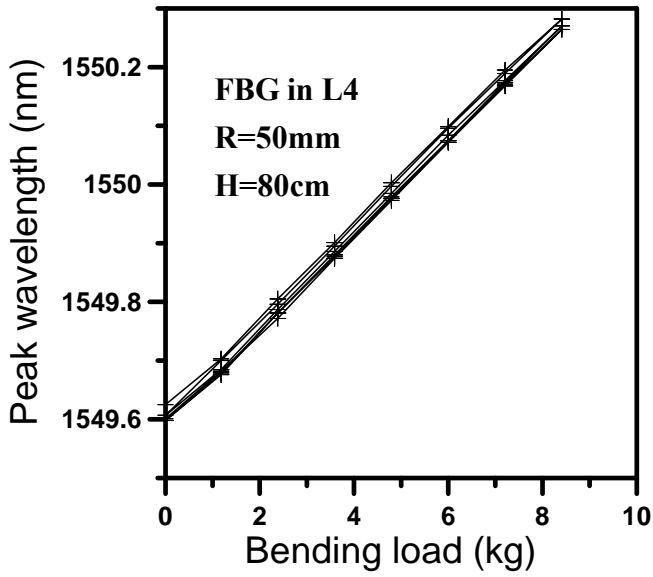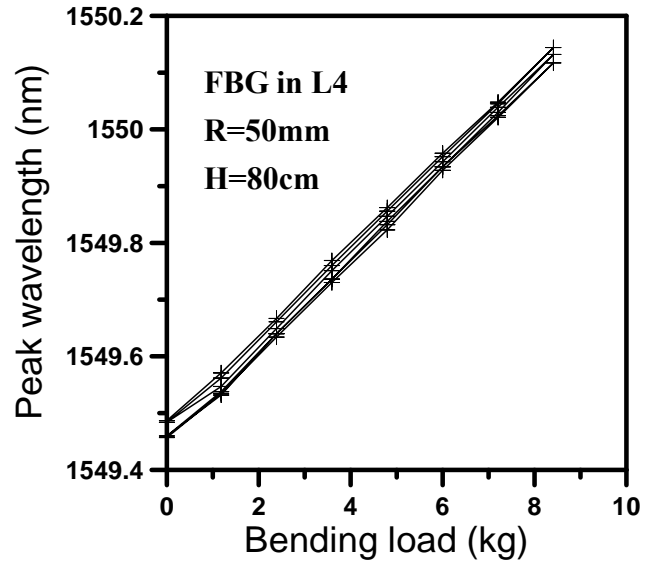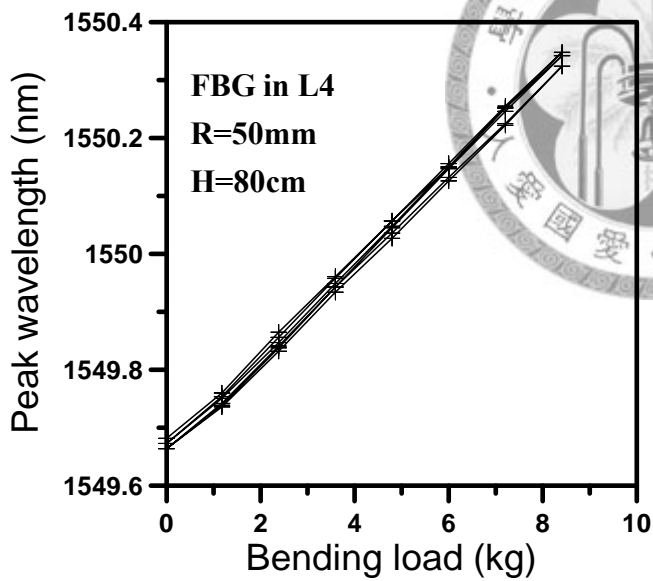**(a) Before impact**　　　　　　　**(b) After impact**

Fig. 4-17: Comparison of Ultrasonic C-scan images between before and after impact under an 80cm drop-height and a distance 50mm from the FBG sensors. (a) Before impact (b) After impact at A0, A45, and A90
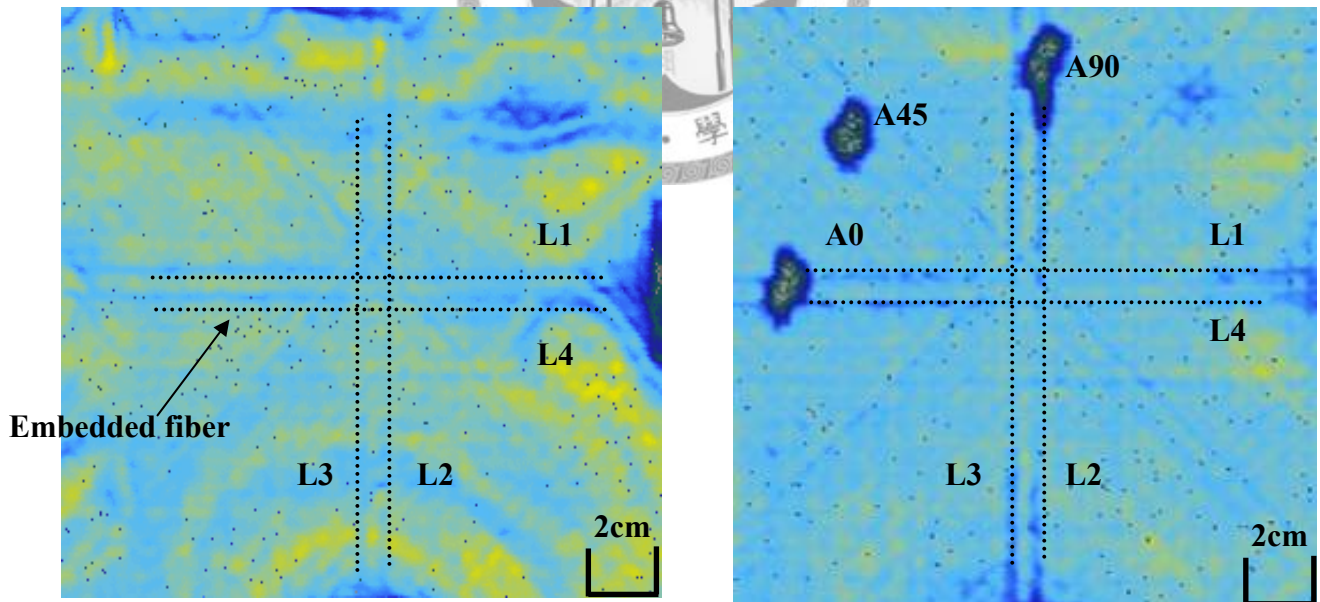
(a) Before impact　　　　　　　**(b) After impact**

Fig. 4-18: Comparison of Ultrasonic C-scan images between before and after impact under a 140cm drop-height and a distance 50mm from the FBG sensors. (a) Before impact (b) After impact at A0, A45, and A90

$$RMSD(\lambda_1, \lambda_2) = \sqrt{\frac{\sum\limits_{i=1}^{n}(\lambda_{2,i} - \lambda_{1,i})^2}{n}}$$
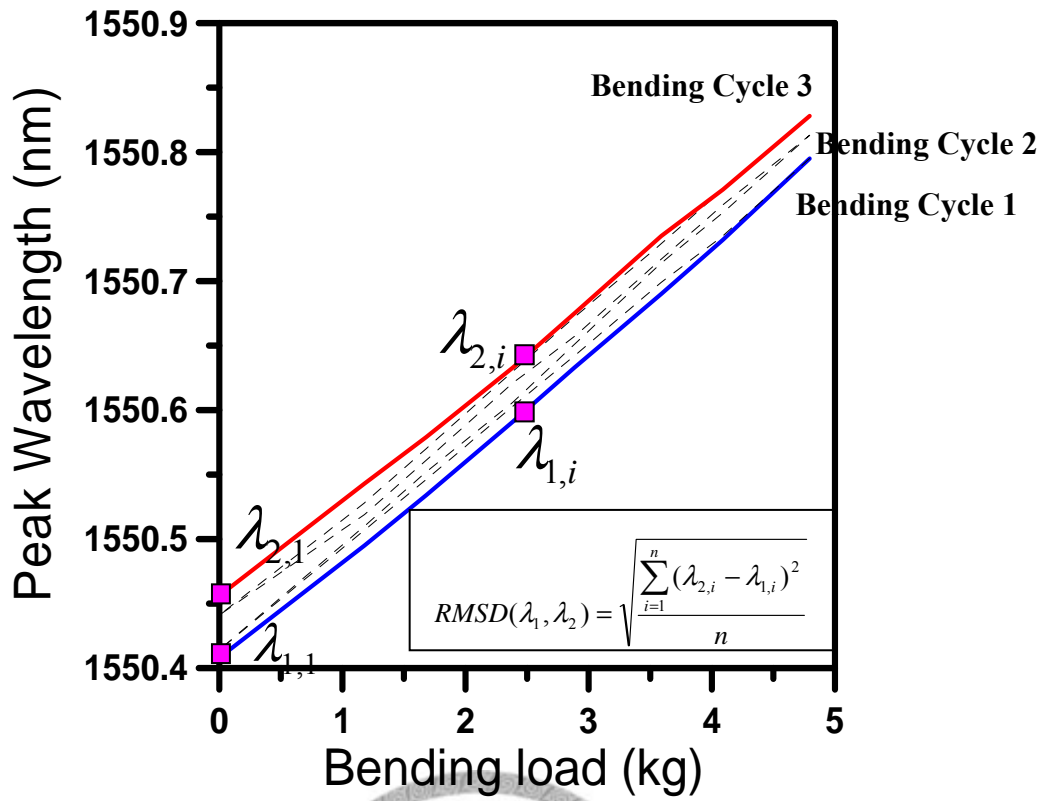
Fig. 4-19: Quantitative evaluation of the average drift distance of peak wavelength lines by RMSD.
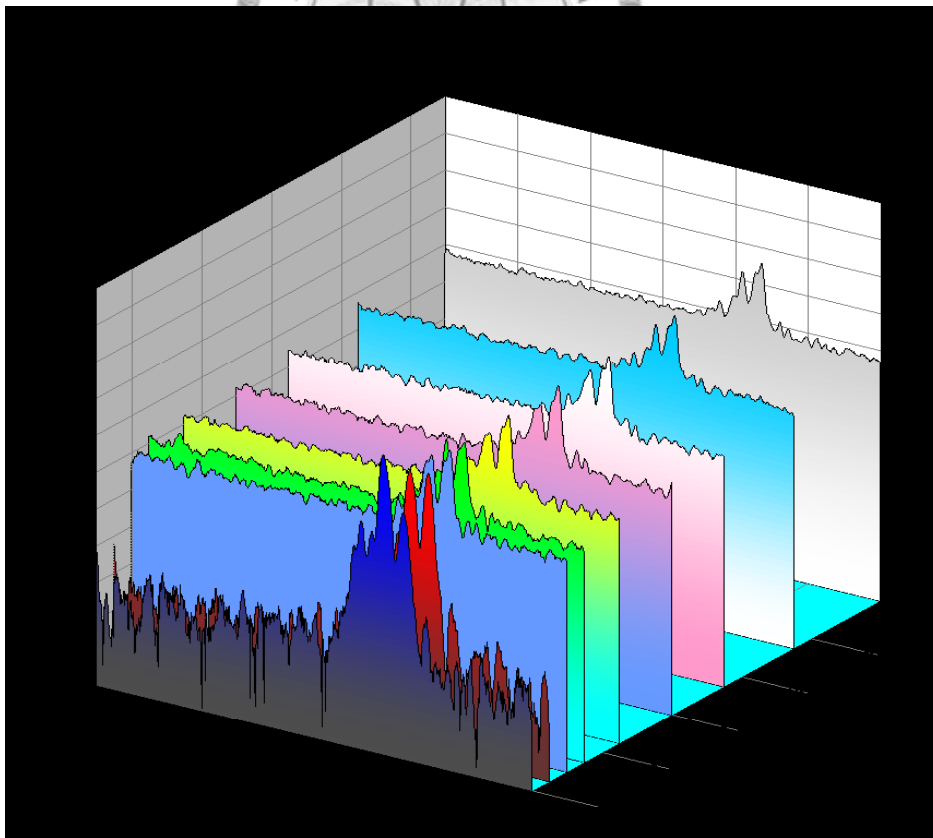
Fig. 4-20: Spectra changes from embedded FBG in L1 with various fatigue cycles under an 80cm drop height and impact at position B
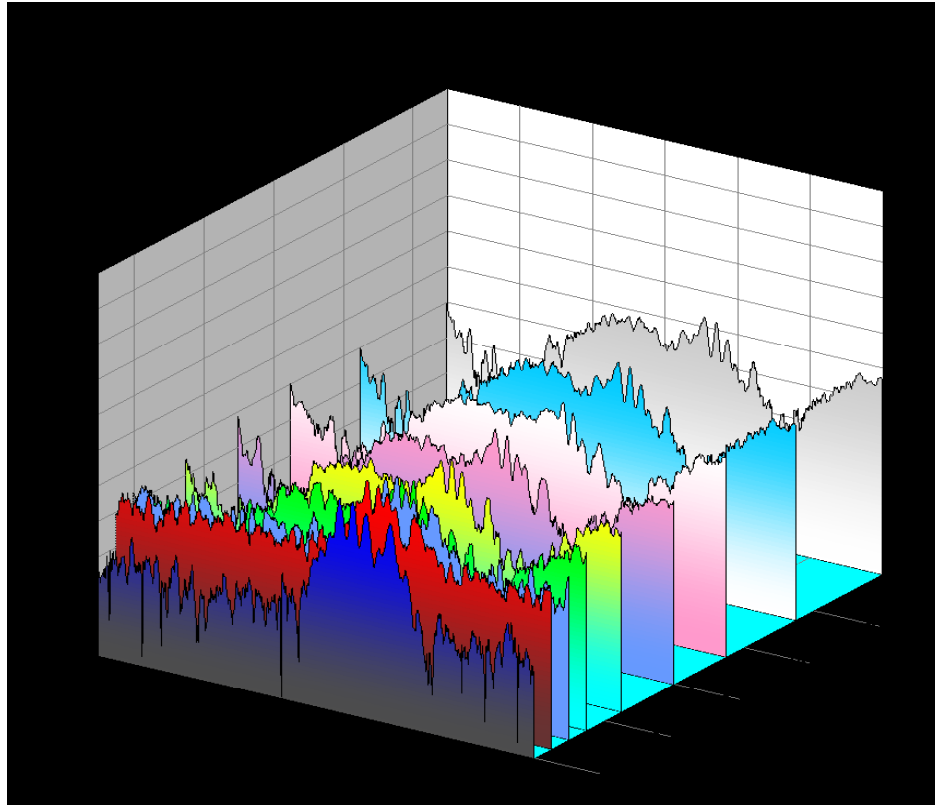
Fig. 4-21: Spectra changes from embedded FBG in L4 with various fatigue cycles under an 80cm drop height and impact at position B
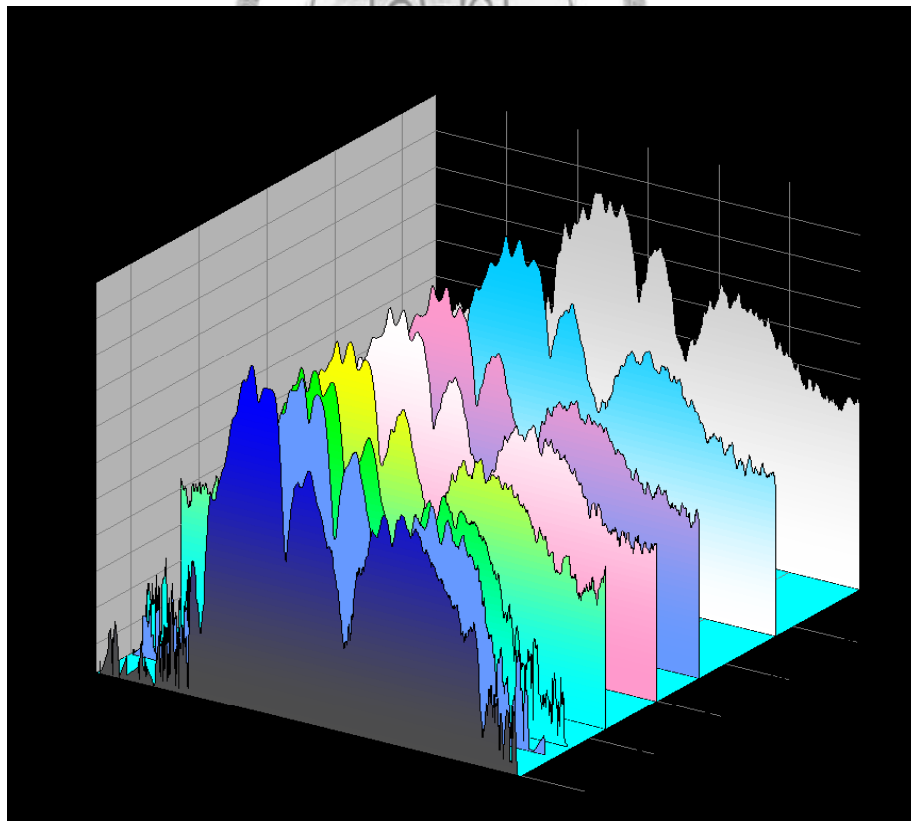
Fig. 4-22: Spectra changes from embedded FBG in L1 with various fatigue cycles under a 140cm drop height and impact at position B
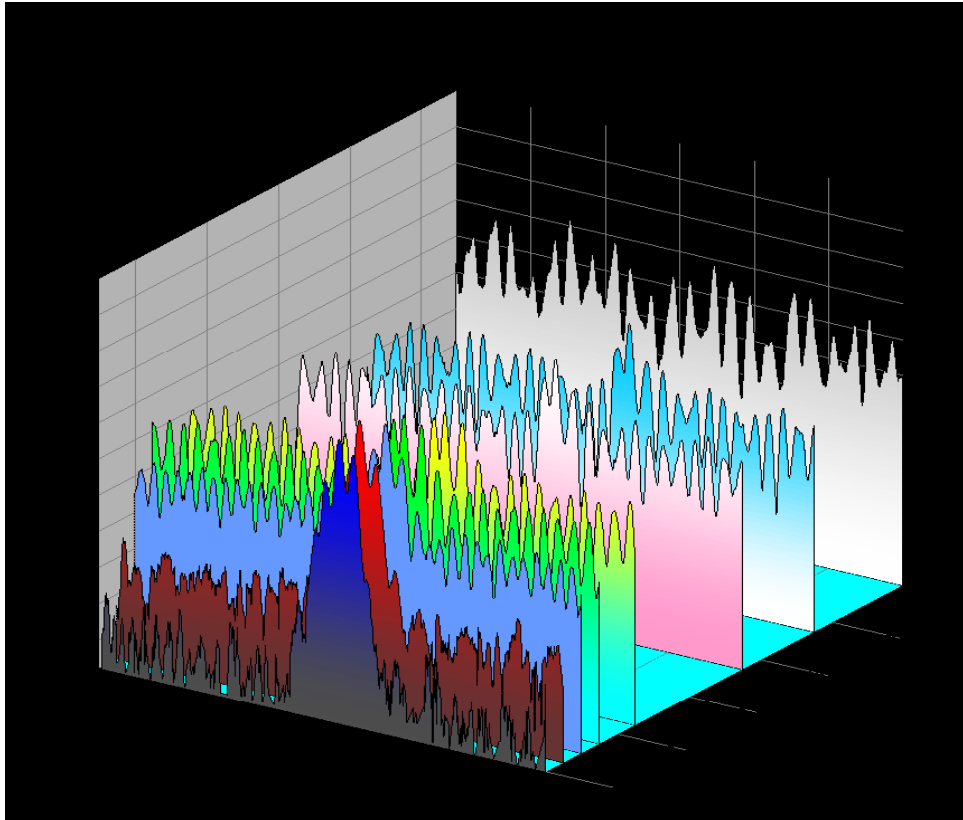
Fig. 4-23: Spectra changes from embedded FBG in L4 with various fatigue cycles under a 140cm drop height and impact at position B

(a)

Optical fiber

Just after impact　　　　　　　**200000 cycles**

(b)

Just after impact　　　　　　　**200000 cycles**
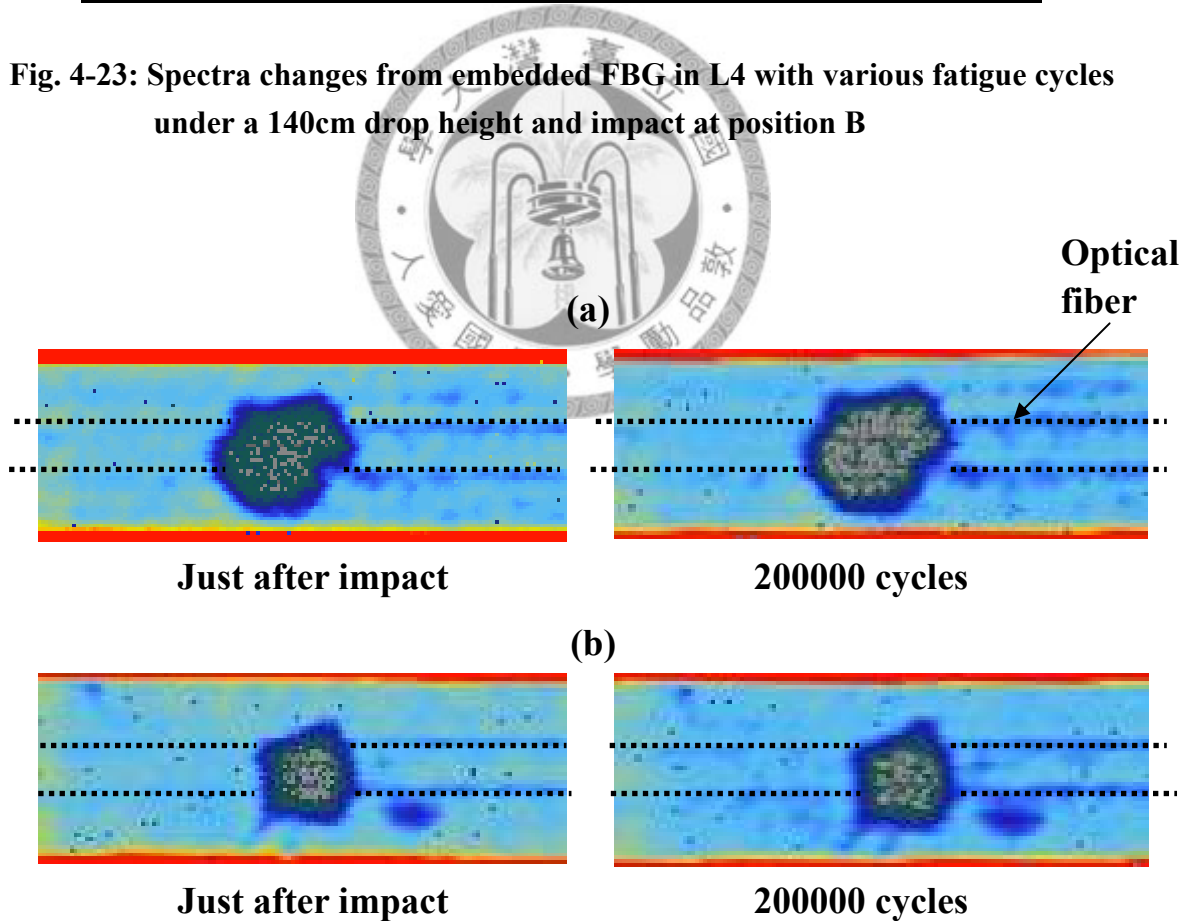
Fig. 4-24: Comparison of Ultrasonic C-scan images between 0 fatigue cycle and 200000 fatigue cycles after impact at the center of specimen (position B):(a) 140cm drop-height (b) 80cm drop-height
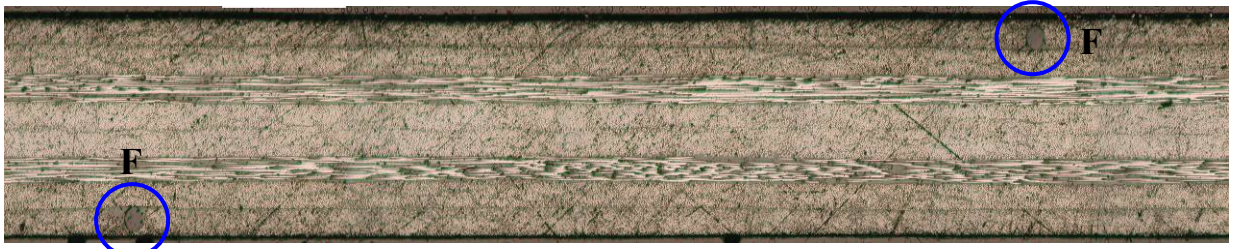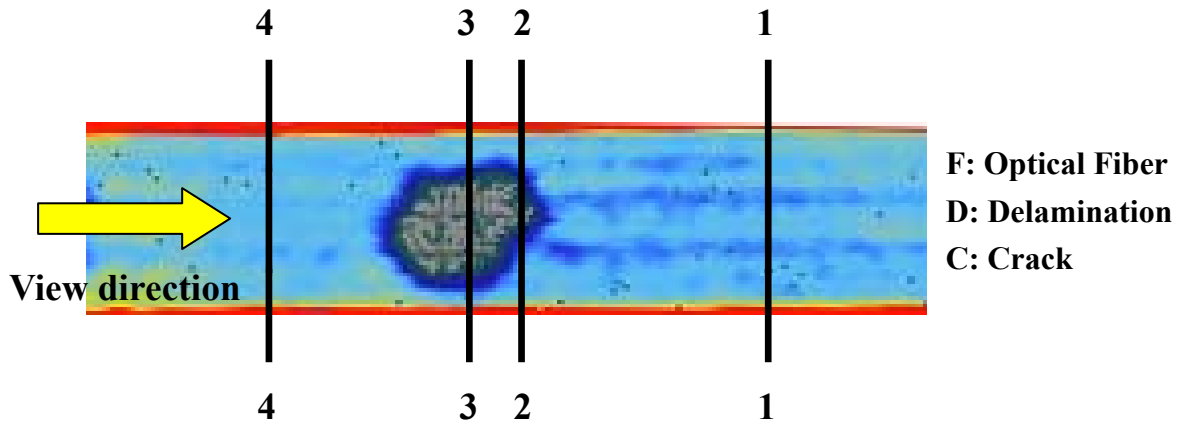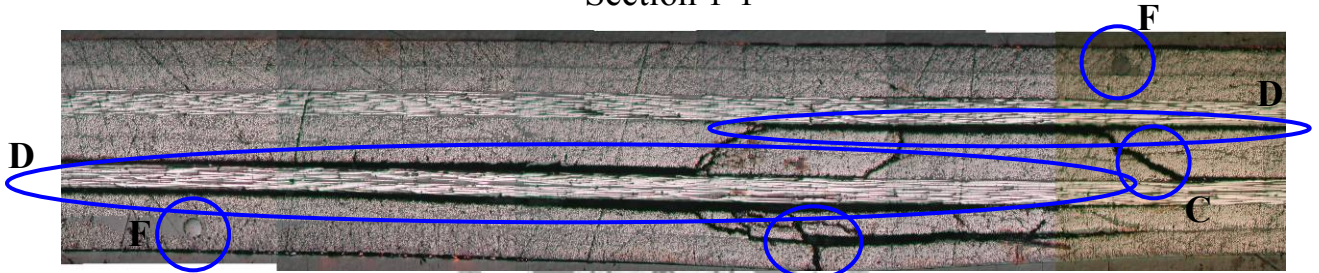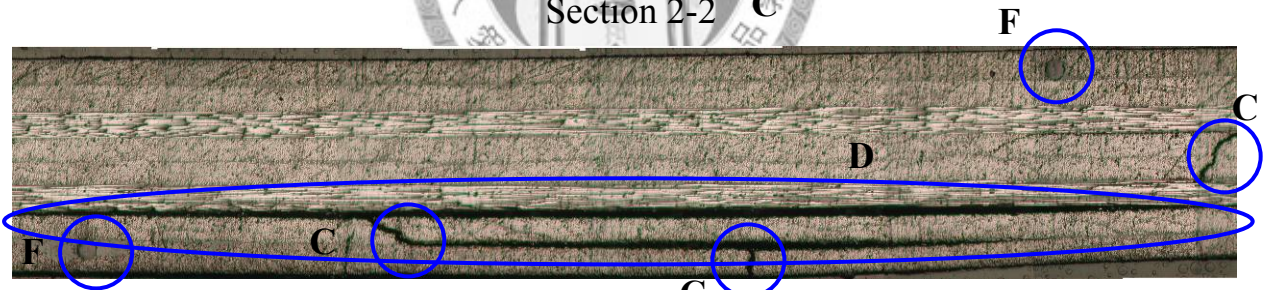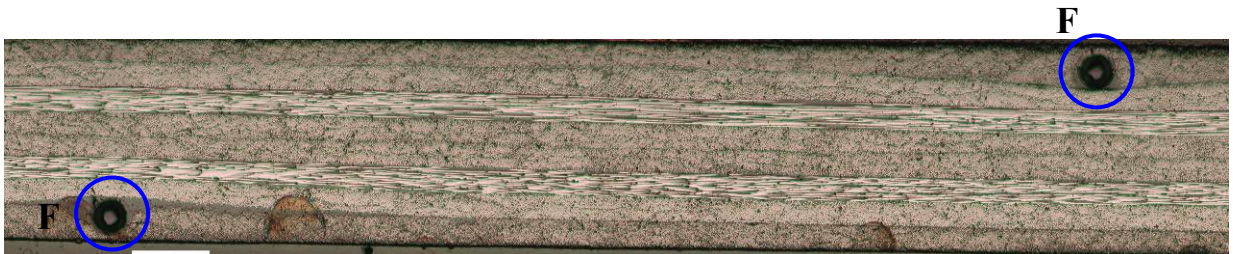
Fig. 4-25: Optical micrographs on the sectional view of the post-impact fatigued specimen (H=140cm, impact position B, 200000 cycles).
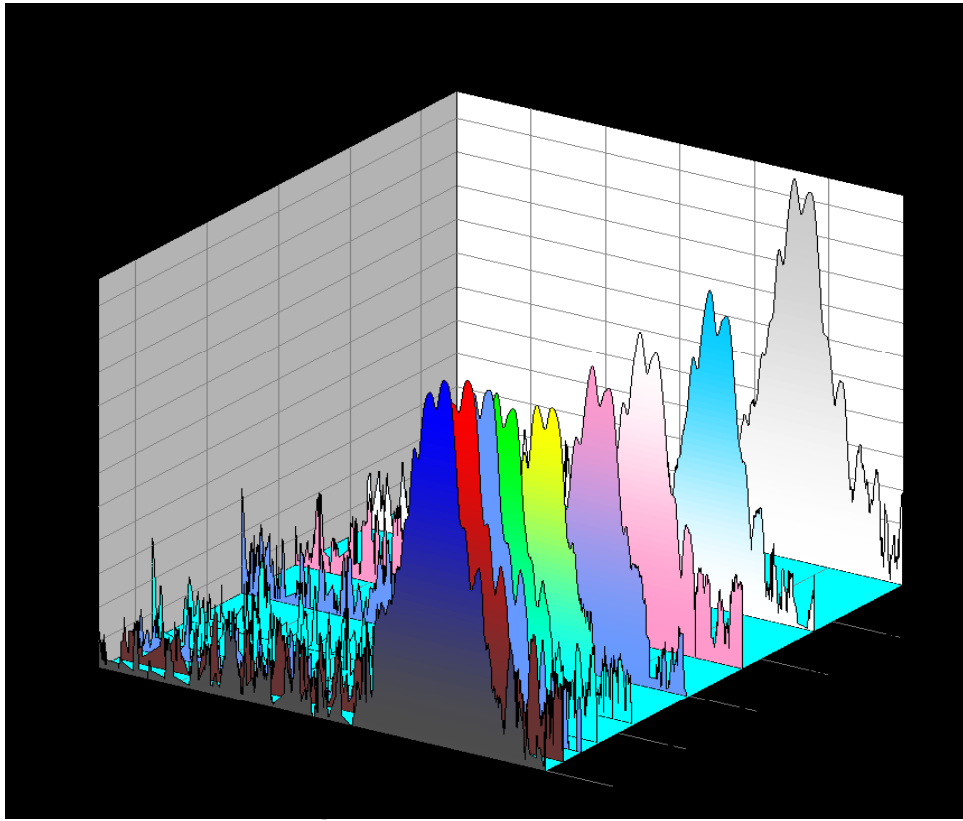
Fig. 4-26: Spectra changes from embedded FBG in L1 with various fatigue cycles under a 140cm drop-height and impact at position A
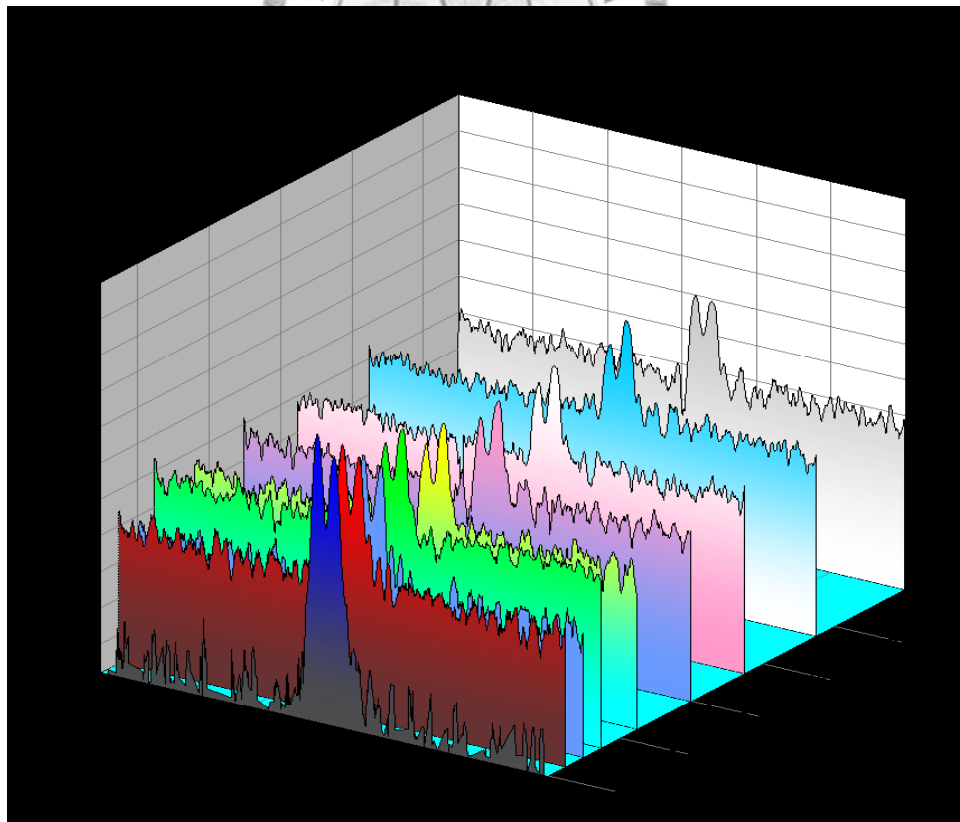
Fig. 4-27: Spectra changes from embedded FBG in L4 with various fatigue cycles under a 140cm drop-height and impact at position A
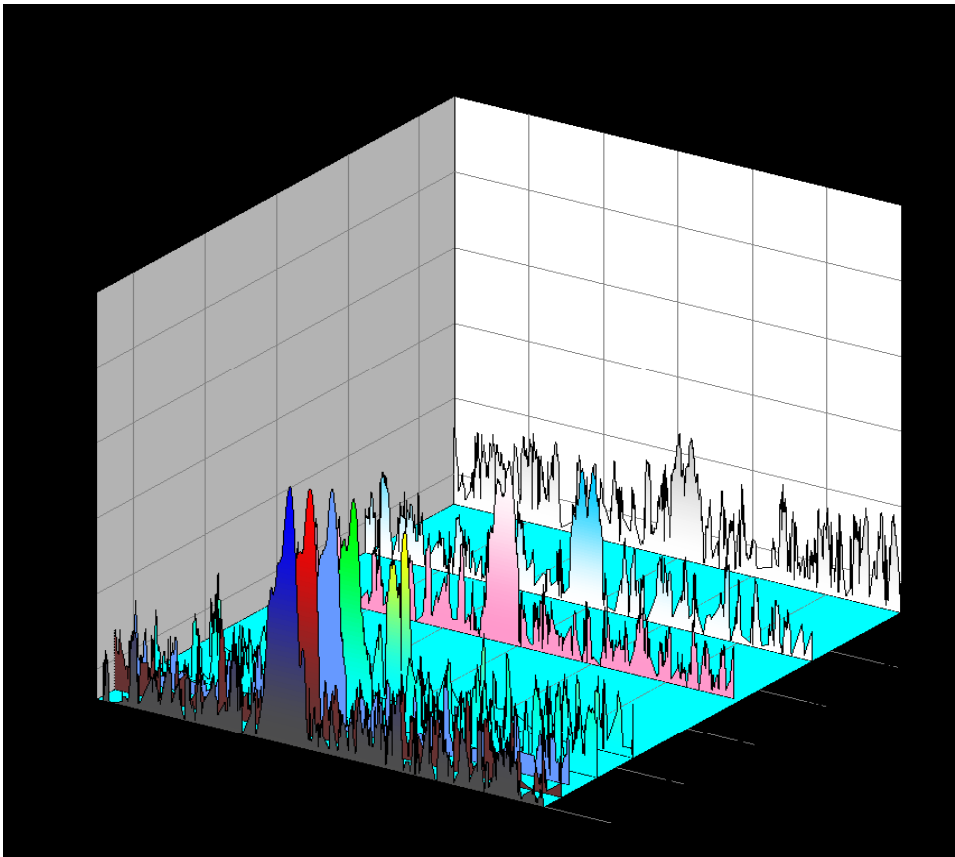
Fig. 4-28: Spectra changes from embedded FBG in L1 with various fatigue cycles under a 140cm drop-height and impact at position C
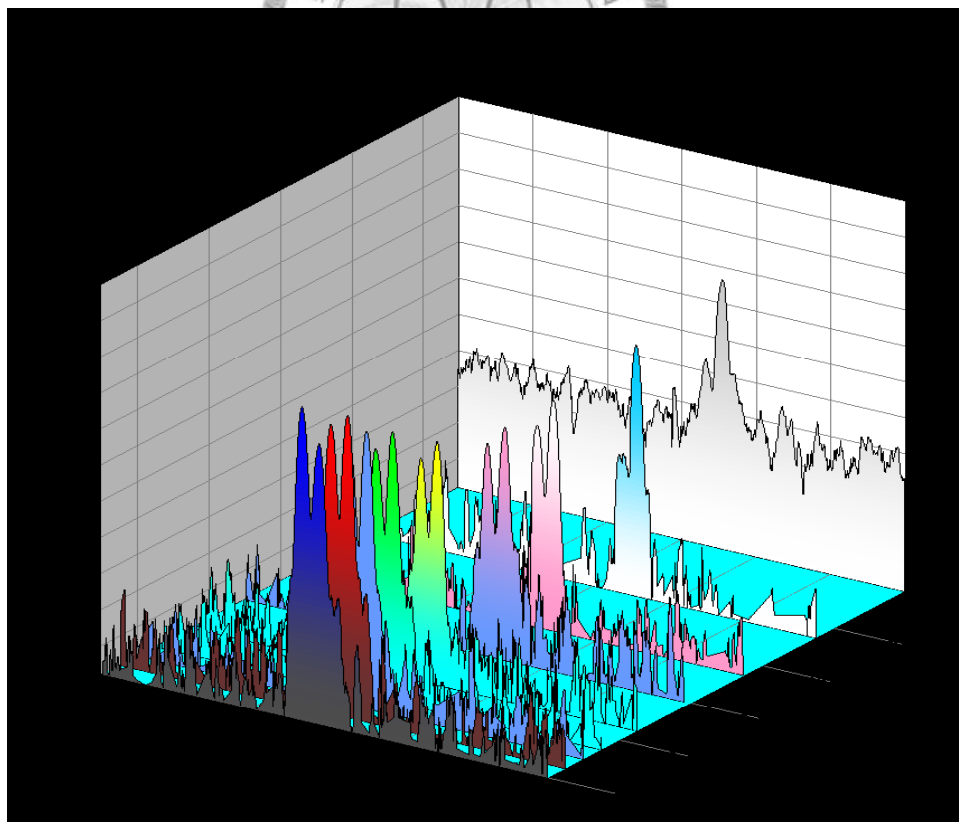
Fig. 4-29: Spectra changes from embedded FBG in L4 with various fatigue cycles under a 140cm drop-height and impact at position C

(a)

FBG

Optical fiber

Just after impact

200000 cycles

Light propagation

(b)

Just after impact
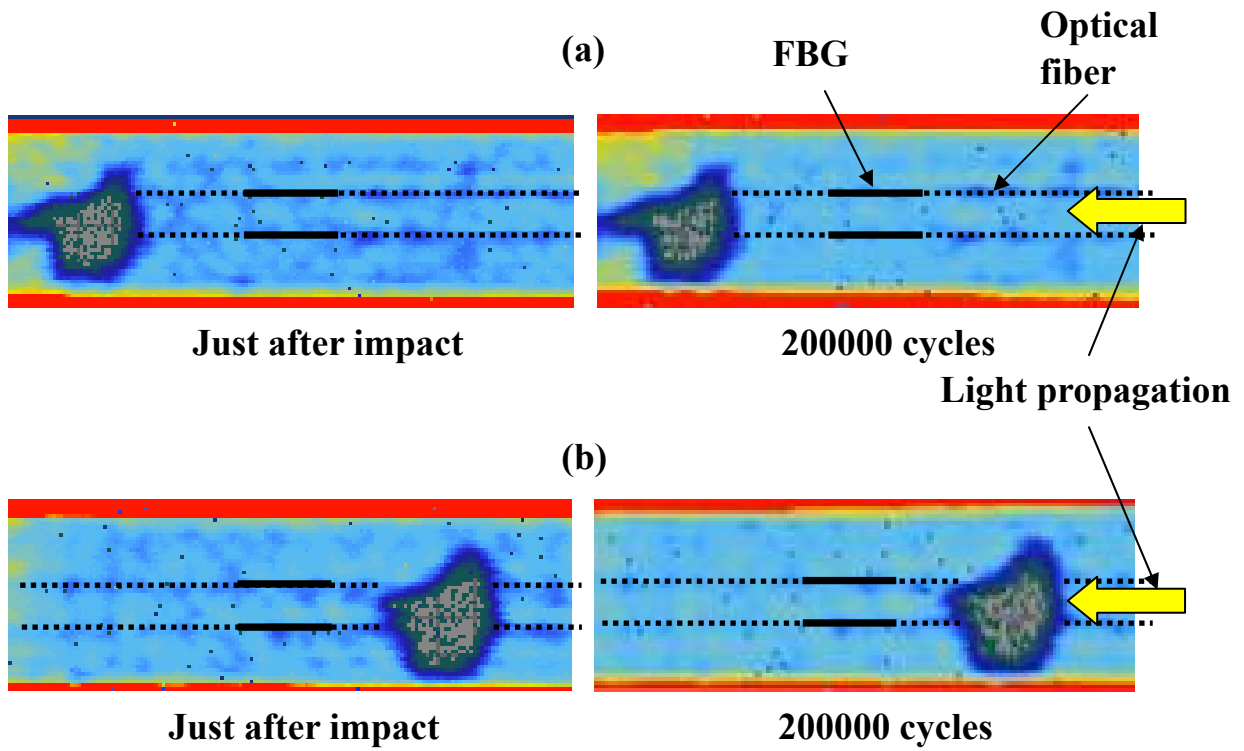
200000 cycles

Fig. 4-30: Comparison of Ultrasonic C-scan images between 0 fatigue cycle and 200000 fatigue cycles after impact under a 140cm drop-height and impact at position A and B: (a) Impact position C (downstream of the gratings) (b) Impact position A (upstream of the gratings)
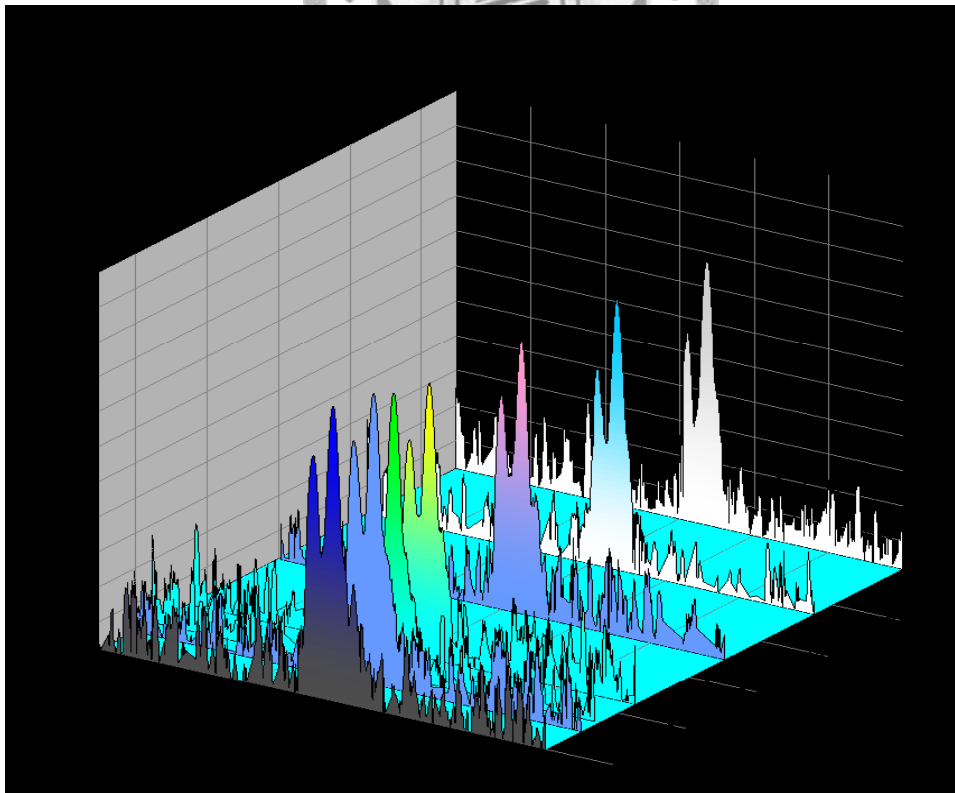
Fig. 4-31: Spectra changes from embedded FBG in L1 with various fatigue cycles without impact.
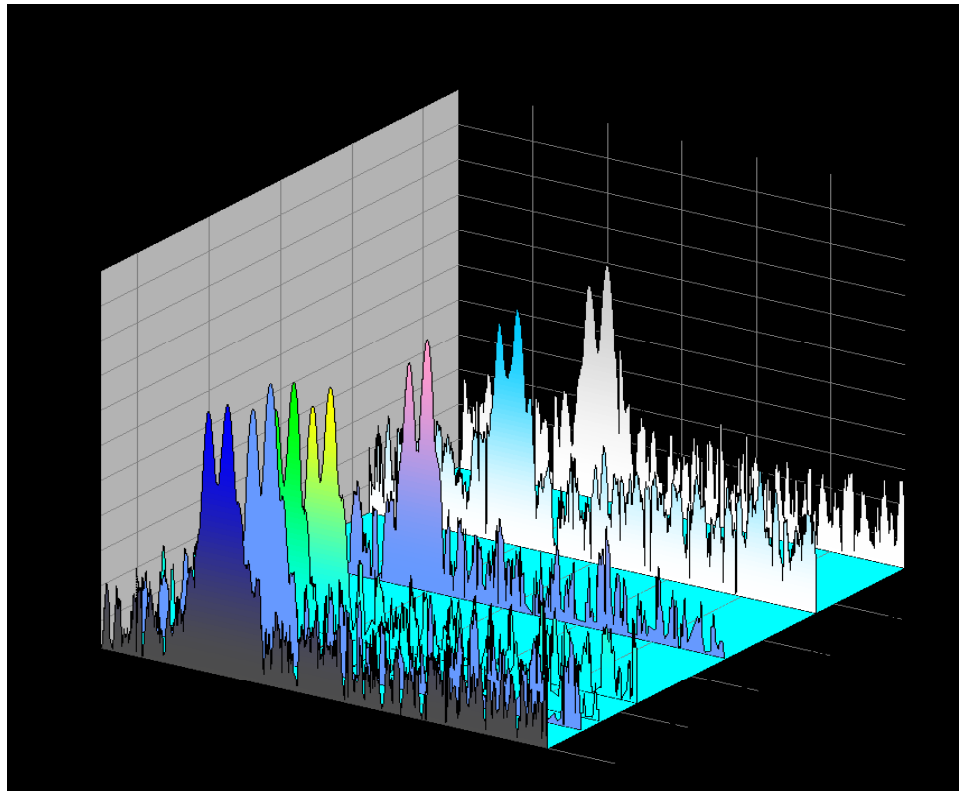
Fig. 4-32: Spectra changes from embedded FBG in L4 with various fatigue cycles without impact.

(a) Fiber surface

Residual resin

(b) Cladding

0.12mm
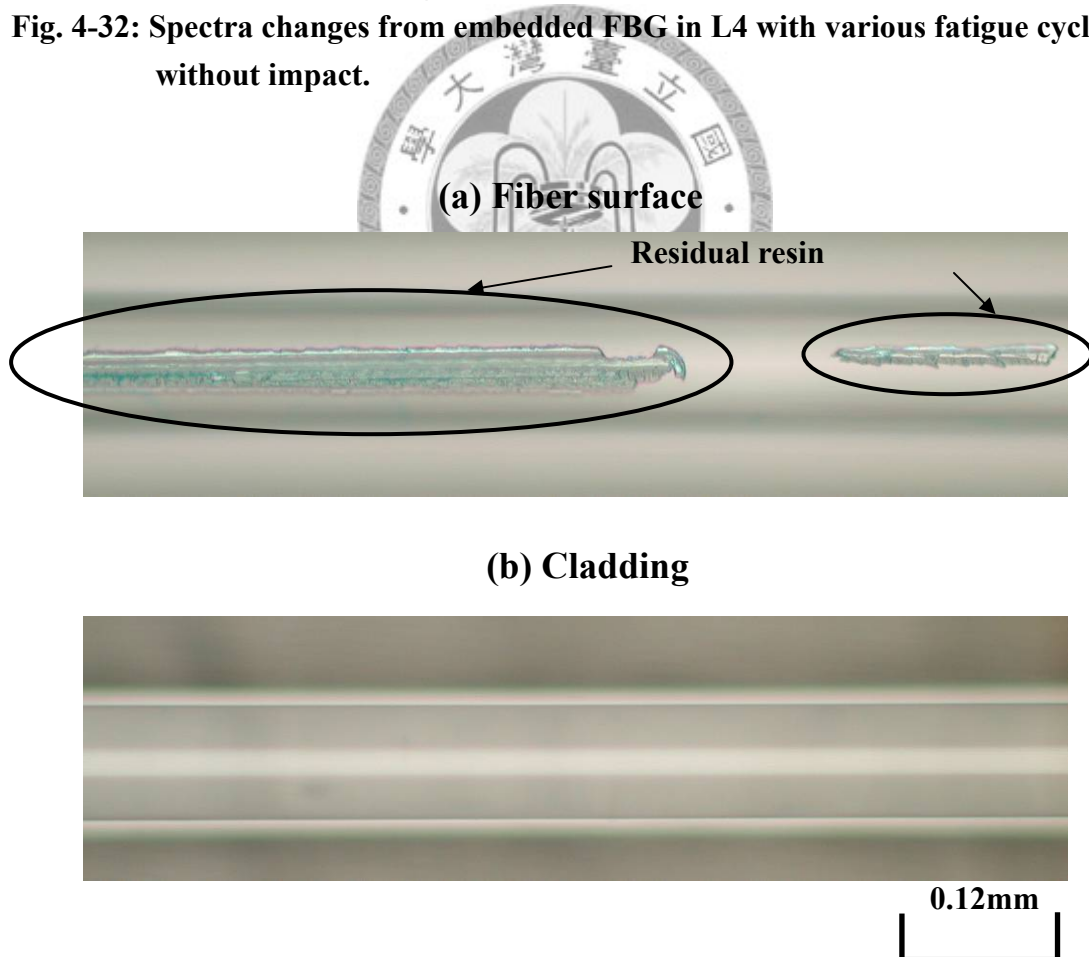
Fig. 4-33: Optical micrographs of the same FBG in L1 as the one whose spectra are shown in Fig 4-20. (a) Focus on fiber surface (b) Focus on cladding

(a) Fiber surface

Residual resin

(b) Cladding

0.12mm
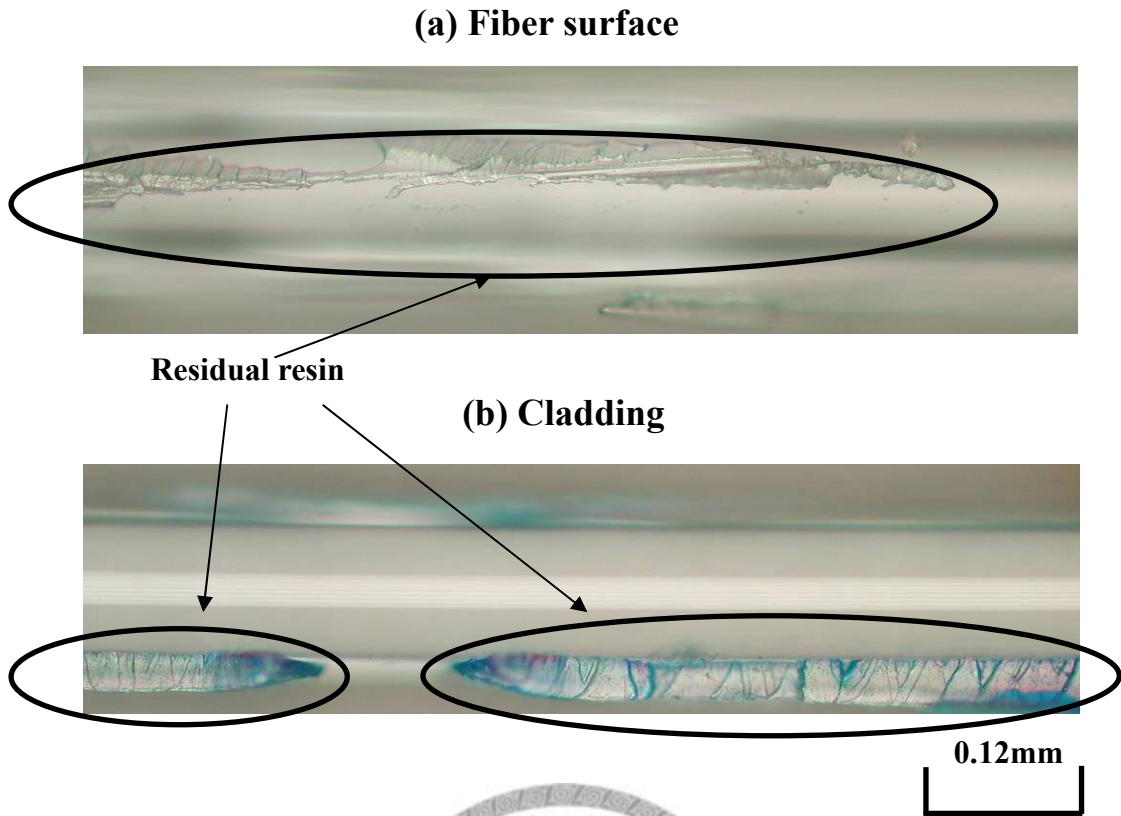
Fig. 4-34: Optical micrographs of the same FBG in L2 as the one whose spectra are shown in Fig 4-21. (a) Focus on fiber surface (b) Focus on cladding
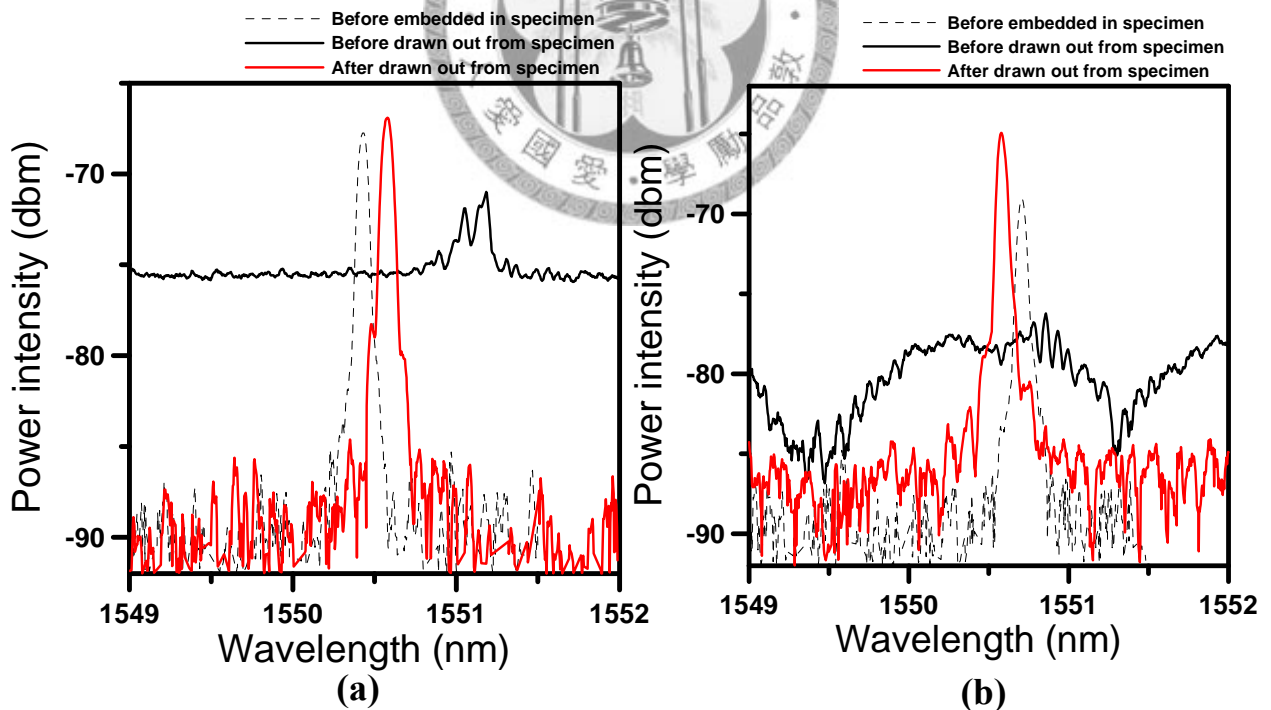
Fig. 4-35: Comparisons of spectra before and after the FBG was drawn out from the specimens, conducted the post-impact fatigue test. (a) The FBG is the same as the one whose spectra is shown in Fig 4-20 (b) The FBG the same as the one whose spectra is shown in Fig 4-21
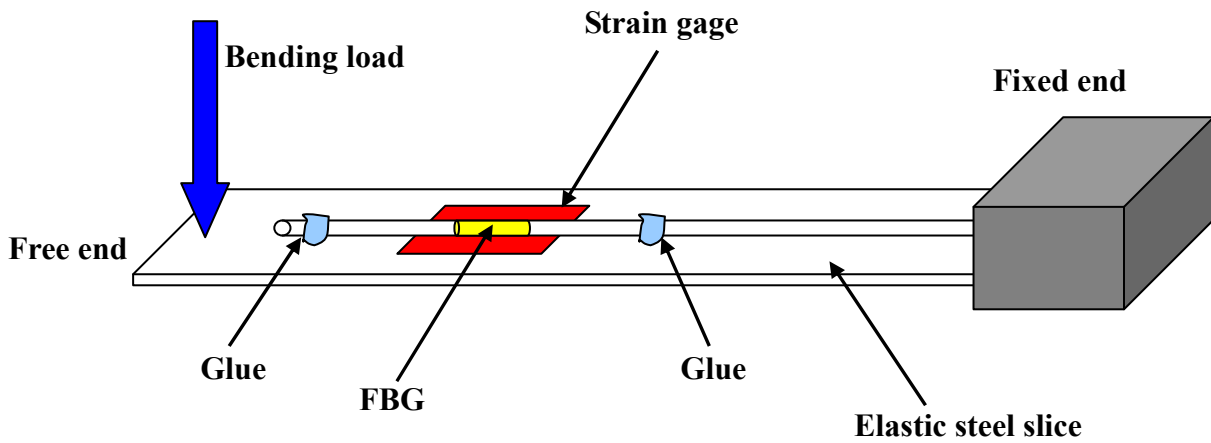
Fig. 4-36: Schematic of experimental set-up in bending test for the FBG drawn out from CFRP specimen.
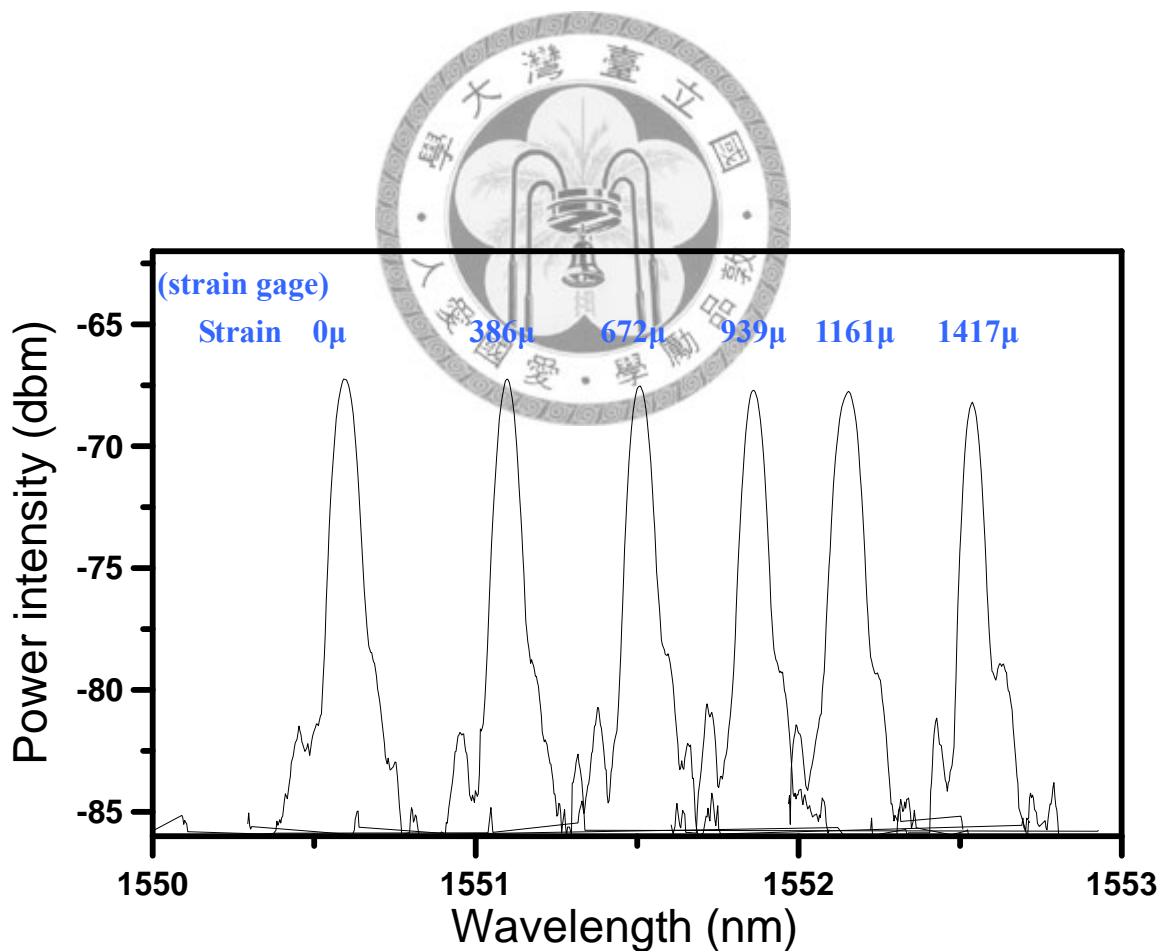
Fig. 4-37: Reflection spectra from the FBG, which is the same as the one whose spectra shown in Fig 4-20, after drawn out from CFRP specimen at various strains
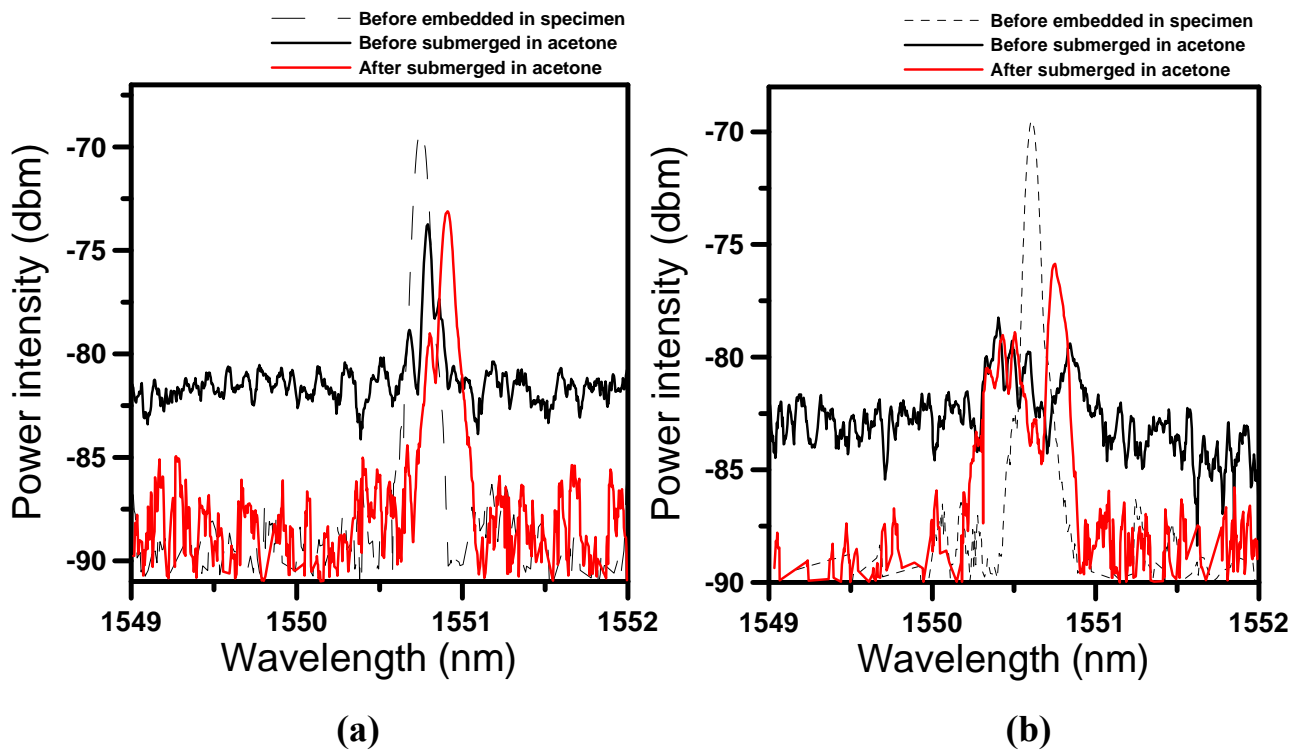
Fig. 4-38: Comparisons of spectra before and after submerging the specimen which had been conducted post-impact test in acetone. (a) Spectra from the FBG embedded in L1 (b) Spectra from the FBG embedded in L4
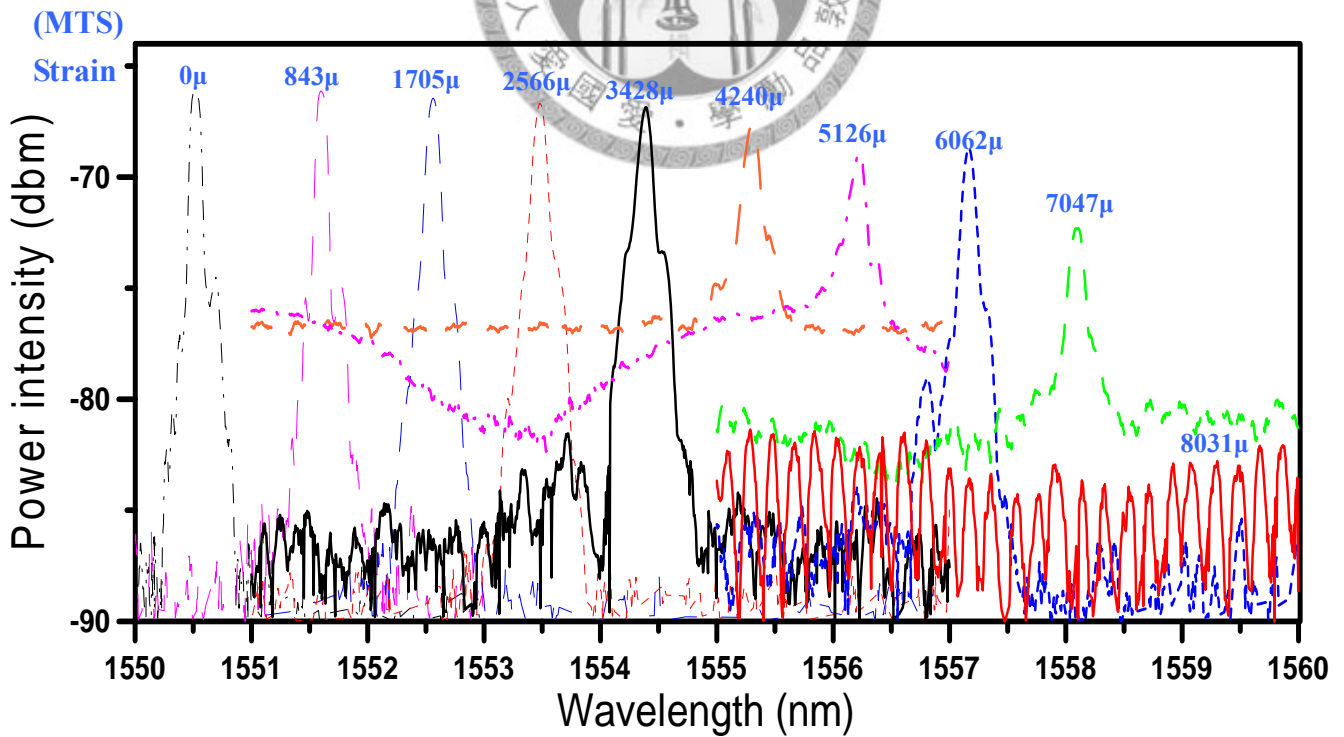
Fig. 4-39: Reflection spectra from the FBG embedded in CFRP specimen along the tensile test at various strains.
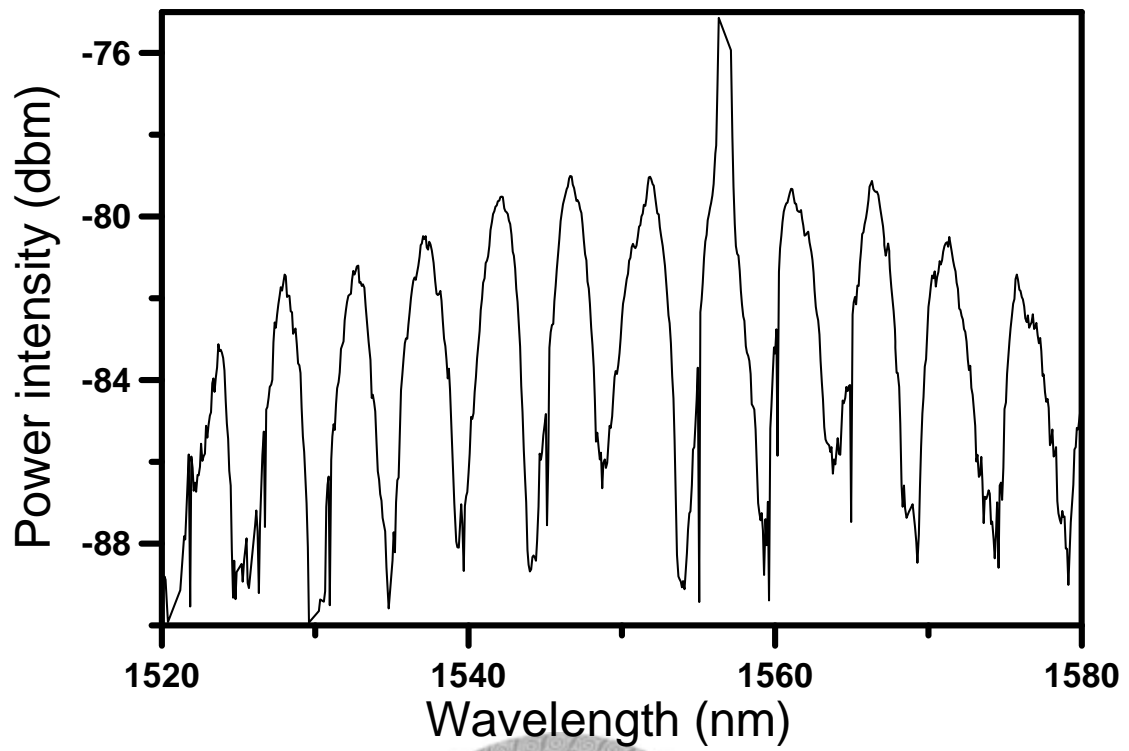
Fig. 4-40: Reflection spectrum at the strain 5126μ in Fig. 4-38 in the wavelength span from 1520nm to 1580nm
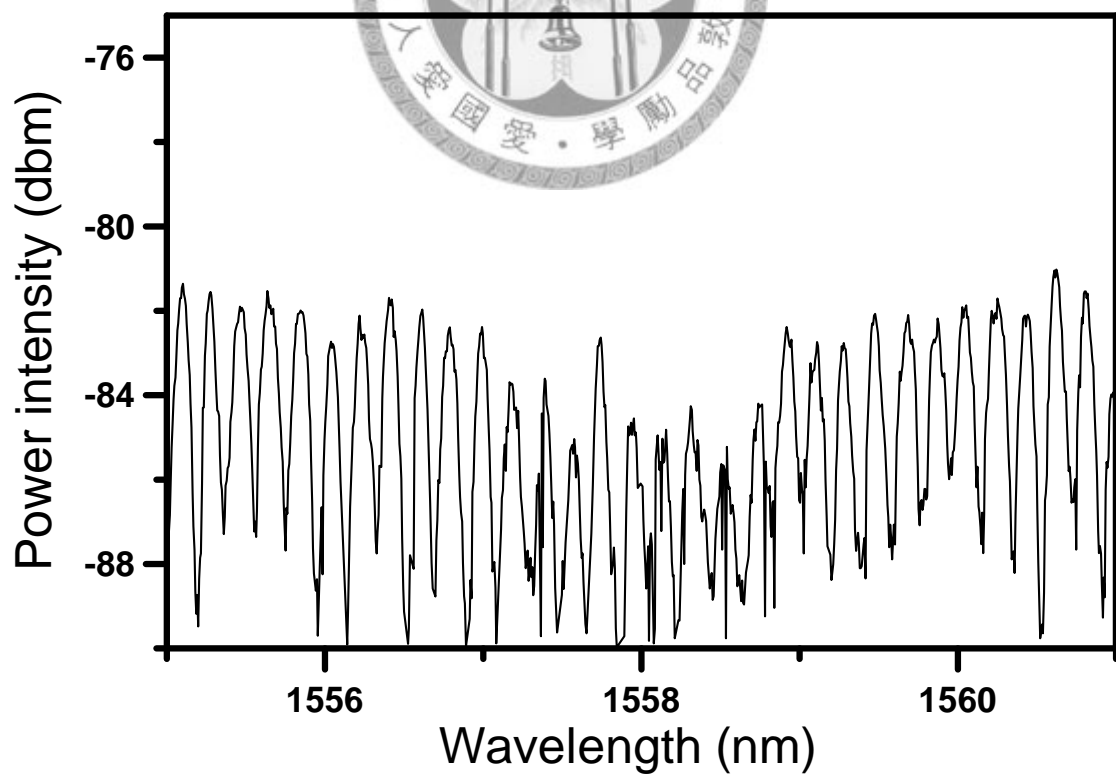
Fig. 4-41: Reflection spectrum at the strain 8031μ in Fig. 4-38 in the wavelength span from 1555nm to 1561nm
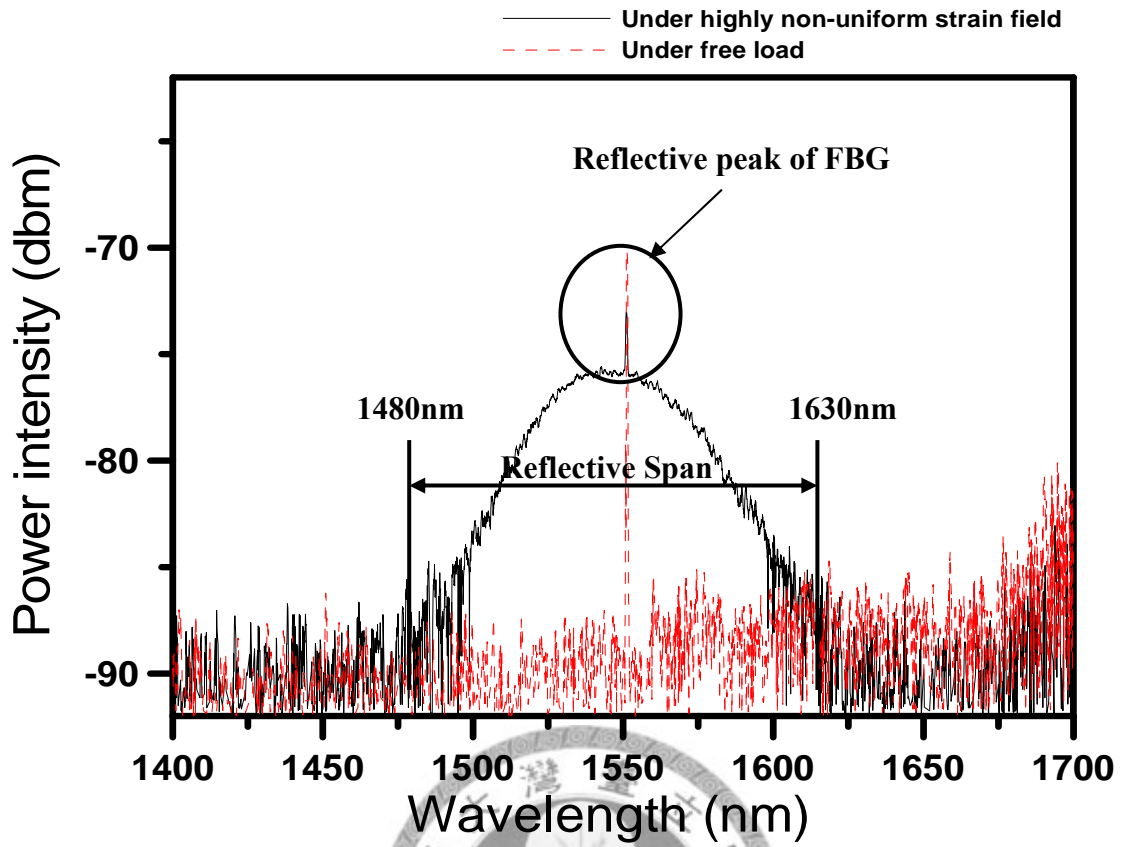
Fig. 4-42: Spectrum of intensity increasing in other wavelength in the span from 1400nm to 1700nm.

Impact distance	Drop height	Impact position	Peak wavelength drift
R=30mm	H=80cm	Before impact	0.011nm
		After impact at A0	0.041nm
		After impact at A0 and A45	0.038nm
		After impact at A0, A45, and A90	0.054nm
	H=140cm	Before impact	0.006nm
		After impact at A0, A45, and A90	**0.019nm (fractured)**
R=50mm	H=80cm	Before impact	0.016nm
		After impact at A0	0.030nm
		After impact at A0 and A45	0.024nm
		After impact at A0, A45, and A90	0.040nm
	H=140cm	Before impact	0.010nm
		After impact at A0, A45, and A90	0.051nm

Table 4.1: Average drift distance in peak wavelength from the FBG in L1 under experimental parameters of different impact distances and drop heights.

Impact distance	Drop height	Impact position	Peak wavelength drift
R=30mm	H=80cm	Before impact	0.007nm
		After impact at A0	0.016nm
		After impact at A0 and A45	0.023nm
		After impact at A0, A45, and A90	0.030nm
	H=140cm	Before impact	0.010nm
		After impact at A0, A45, and A90	0.040nm
R=50mm	H=80cm	Before impact	0.009nm
		After impact at A0	0.016nm
		After impact at A0 and A45	0.031nm
		After impact at A0, A45, and A90	0.042nm
	H=140cm	Before impact	0.004nm
		After impact at A0, A45, and A90	0.043nm

Table 4.2: Average drift distance in peak wavelength from the FBG in L2 under experimental parameters of different impact distances and drop heights.

Impact distance	Drop height	Impact position	Peak wavelength drift
R=30mm	H=80cm	Before impact	0.008nm
		After impact at A0	0.027nm
		After impact at A0 and A45	0.034nm
		After impact at A0, A45, and A90	0.041nm
	H=140cm	Before impact	0.011nm
		After impact at A0, A45, and A90	0.042nm
R=50mm	H=80cm	Before impact	0.009nm
		After impact at A0	0.015nm
		After impact at A0 and A45	0.036nm
		After impact at A0, A45, and A90	0.040nm
	H=140cm	Before impact	0.009nm
		After impact at A0, A45, and A90	0.039nm

Table 4.3: Average drift distance in peak wavelength from the FBG in L3 under experimental parameters of different impact distances and drop heights.

Impact distance	Drop height	Impact position	Peak wavelength drift
R=30mm	H=80cm	Before impact	0.008nm
		After impact at A0	0.023nm
		After impact at A0 and A45	0.026nm
		After impact at A0, A45, and A90	0.049nm
	H=140cm	Before impact	0.005nm
		After impact at A0, A45, and A90	0.050nm
R=50mm	H=80cm	Before impact	0.026nm
		After impact at A0	0.033nm
		After impact at A0 and A45	0.029nm
		After impact at A0, A45, and A90	0.041nm
	H=140cm	Before impact	0.005nm
		After impact at A0, A45, and A90	0.046nm

Table 4.4: Average drift distance in peak wavelength from the FBG in L4 under experimental parameters of different impact distances and drop heights
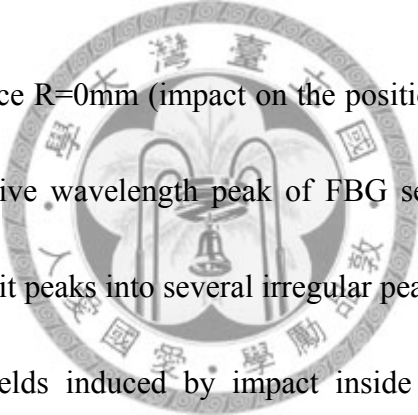
FBG	Impact distance (R)	Drop height (H)	Difference of drift distance between before impact and after impact at A0, A45, and A90
L1	30mm	80cm	0.043nm
		140cm	**0.013nm (fractured)**
	50mm	80cm	0.024nm
		140cm	0.041nm
L2	30mm	80cm	0.024nm
		140cm	0.030nm
	50mm	80cm	0.033nm
		140cm	0.039nm
L3	30mm	80cm	0.033nm
		140cm	0.031nm
	50mm	80cm	0.031nm
		140cm	0.030nm
L4	30mm	80cm	0.041nm
		140cm	0.045nm
	50mm	80cm	0.015nm
		140cm	0.041nm

Table 4.5: Differences of drift distances in peak wavelength between before impact and after impact at all positions.

Chapter 5 Conclusions and future work

5.1 Impact damage monitoring

We have demonstrated the use of embedded FBG sensors in composite materials for investigating the impact damage. When applying impact the location where the FBG sensors were embedded, the FBG sensors did not fracture and could still function. It indicates that the FBG sensors was protected very well as they are embedded in the CFRP structure, even if the impact directly stroke on the position of embedded FBG sensors.

For the impact distance R=0mm (impact on the position of embedded FBG), the results showed the reflective wavelength peak of FBG sensors was broadened and deformed from the two split peaks into several irregular peaks. This was resulted from the non-uniform strain fields induced by impact inside the CFRP structure. The alteration of waveform was relatively slight in L1 and there were significant changes in the spectra in L2 and L3. The change in spectra from the FBG in L4 was more evident than L1 FBG, but it was not as evident as the FBG in L2 and L3. These results indicate that the impact-induced damage in L2 and L3 were much more serious, and relatively slight in L1. This agrees with the damage distribution due to impact.

For the impact at distances R=30mm and R=50mm from FBG, the FBG sensor was less sensitive. However, the damage caused by impact can still be revealed by the

hysteresis shift in wavelength during bending. Generally, the FBG sensors responded larger drift distances during bending test under higher impact energy and closer impact distance to embedded FBGs. The drift distance before impact was about under 0.015nm. After impact at A0, A45, and A90, it was about 0.040 to 0.050nm.

5.2 post-impact fatigue damage monitoring

In post-impact fatigue test, it could be observed that the intensity of characteristic peak gradually decreased as the fatigue cycle increased, and the intensity of other wavelengths dramatically increased. In this case, the reflective peak of the FBG sensor was almost surmounted, and the reflective waveform was difficult to be distinguished. In other words, the FBG sensor lost its capability to act as a sensor. For this reason, we changed our objective to find out the factor causing the FBG sensor to reflect the light in a wide wavelength span.
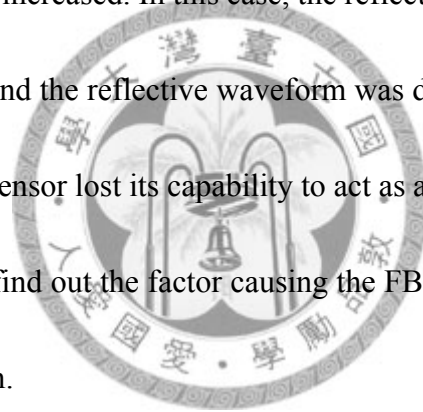
We originally assumed that this reflection in other wavelengths was caused by the water corrosion of the optical fiber and impact-induced microcracks. By carrying out a number of tests, we have proven that this phenomenon is attributed to the highly non-uniform strain inside the CFRP specimen near the impact position induced by a combination of fatigue and impact damages. Due to this restriction, it is necessary to reduce the effect of strain to avoid the occurrence of the intensity increasing in other wavelengths when monitoring the damage development.

5.3 Future works

1. Other fabricating method

To reduce the influence of internal thermal residual stress in the CFRP structure, the embedded method and the laminates stacking method could be rearranged to prevent the birefringence effect. If the FBG sensors could be embedded without the thermal residual stress, the strain or crack density in laminates will be evaluated more accurately using the FBG sensors.

2. Using the small-diameter and recoated FBG sensors

One previous study has suggested that using the recoated FBG sensors with small diameter could efficiently reduced the effect of thermal residual stress on the reflective spectrum [36]. The recoated FBG sensors might have greater impact endurance and reduce the effect of thermal stress. Moreover, the small diameter FBG sensors for embedded in composite laminate will enhance the compatibility with the carbon fiber laminate.

3. Further detecting distance

Due to the dimension limitation of the specimen, the designed damage detecting distance in this study is not practicable for measuring the interior damage in large-scale structure. To clarify the sensibility of embedded FBG sensor, the larger size specimen and further impact distance were recommended in future work.

4. Clarify the correlation between the strain inside the CFRP structure and the intensity increasing in other wavelengths

Although we have discovered that the phenomenon of intensity increasing in other wavelength would occur under a certain strain in the CFRP structure, we were yet unable to find out the real value of this strain. We may reproduce the similar strain fields which could result in this phenomenon by other experiments, in order to facilitate with the analysis.

References

[1] Alan D. Kersey, "Fiber grating sensors" Journal of lightwave technology, Vol 15, No. 8, (1997)

[2] Lin C.L., "Opto-mechanical applications of Microstructured Materials" PhD thesis, Joseph Fourier University /National Taiwan University, (2004)

[3] Bass M., Eric W. Van Stryland, "Fiber optics handbook: fiber, devices, and systems for optical communications," New York: McGraw-Hill, (2002)

[4] Whitten L. Schulz, "Advanced fiber grating strain sensor systems for bridges, structures, and highways," *Proc. SPIE,* Vol. 3325, pp. 212-221, (1998)

[5] Nye J.F., "Physical properties crystal: their representation by tensor and matrices," Oxford University Press, (1957)

[6] Bertholda A., Dändliker R., "Determination of the individual strain-optic coefficients in single-mode optical fibres," *Journal of lightwave Technology*, Vol. 6, No. 1, pp. 17-20, (1988)

[7] Tao X., Tang L., "Internal strain measurement by fiber Bragg grating sensors in textile composites," *Composites Science and Technology*, Vol. 60, pp. 657-669, (2000)

[8] Menendez J. M., Guemes, J.A., "Bragg-grating-based multiaxial strain sensing: its application to residual strain measure ment in composite laminates," *Proceedings of SPIE*, Vol. 3986, pp. 271-281, (2000)

[9] Hill P.C., Eggleton, B.J., "Strain gradient chirp of fibre Bragg gratings," *Electronic Letters*, vol.30, no.14, pp.1172-1174, (1994)

[10] Kashyap R. "Fiber Bragg gratings," San Diego, CA : Academic Press, (1999)

[11] Shin C.S., Chiang C.C., "Temperature compensated fiber Bragg grating using fiber reinforced polymeric composites," *Journal of the Chinese institute of Engineers*, Vol. 29, No.3, pp. 519-526, (2006)

[12] Hill K.O., Fujii Y., "Photosensitivity in optical waveguides: Application to reflection filter fabrication," Appl. Phys. Lett. 32(10), pp. 647, (1978)

[13] Meltz, G., "Formation of Bragg gratings in optical fibres by a Transverse Holographic Method," *Optics Letters*, vol.14, no.15, pp.823-825, (1989)

[14] Hill, K.O., Malo B., "Bragg gratings fabricated in monomode photosensitive optical fiber by UV exposure through a phase mask," *Applied Physics Letters*, vol.62, no.10, pp.1035-1037, (1993)

[15] Wagreich R.B., "Effects of diametric load on fibre Bragg gratings fabricated in low birefringent fibre," Electron Lett 32(13), pp.1223–4, (1996)

[16] Okabe Y, Yashiro S., "Effect of thermal residual stress on the reflection spectrum from fiber Bragg grating sensors embedded in CFRP laminates" *Elsevier Composites*, Part A 33, pp. 991–999, (2002)

[17] Rachid G., Mahmoud A, El-sherif, "Analysis of induced-birefringence effects on Fiber Bragg Gratings" *Optical Fiber Technology* 6, pp. 299-323, (2000)

[18] Vieira A., "Effect of the recoating and the length on fiber Bragg grating sensors embedded in polymer composites" *Elsevier Materials and Design* 30, pp. 1818–1821, (2009)

[19] Chambers A.R., "Evaluating impact damage in CFRP using fibre optic sensors," *Elsevier Composites Science and Technology* 67, pp. 1235-1242, (2007)

[20] Takeda S., "Delamination monitoring of laminated composites subjected to low-velocity impact using small-diameter FBG sensors," *Elsevier Composites*, Part A 36, pp. 903-908, (2005)

[21] Wang C.M. "Damage behaviors of notched composite laminates" *PhD thesis*, National Taiwan University, (2001)

[22] Liu D., "Impact-induced delamination- a review of bending stiffness mismatching," *Journal of Composite Materials*, Vol.22, Pages 674-692, (1988)

[23] Besant T., "Finite element modeling of low velocity impact of composite sandwich panels," *Elsevier Composites*, Part A 32, pp. 1189-1196, (2001)

[24] Abrate S., "Impact on laminated composites: recent advances," *ppl. Mech. Rev.* 41, pp. 517-539, (1994)

[25] Mahinfalah M., Skordahl R., "The effects of hail damage on the fatigue strength of graphite/epoxy composite laminate," *Elsevier Composites Structures,* 42, pp. 101-106, (1998)

[26] He Y.R., "Comparison and analysis between non-destructive and destructive microscopic testing for investigation of damage in composite laminates" *Master thesis,* National Taiwan University, (2007)

[27] Chiang C.C., "Investigation of the fatigue damage in polymeric composite by using optic fiber grating sensors," *PhD thesis,* National Taiwan University, (2004)

[28] Cantwell W. J., J Morton, "Detection of impact damage in CFRP laminates," *Composite Structures*, 3, pp. 241-257, (1985)

[29] Digby D.S., Graham D., "Fatigue testing of impact-damaged T300/914 carbon-fibre-reinforced plastic," *Elsevier Composites Science and Technology*, 60, pp. 379-389 (2000)

Appendix

台電工程月刊

A Comparison Between Different Examination Techniques for Impact, Torsional and Adhesive Joint Failures in Polymeric Composite Materials
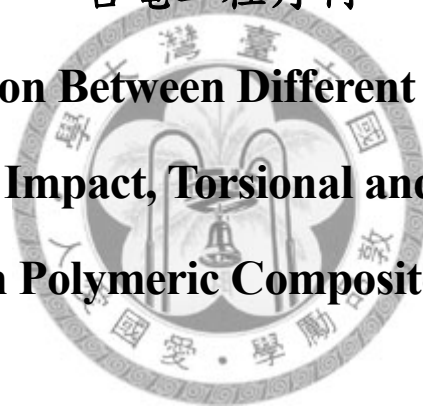
複合材料衝擊、扭轉及膠合破壞檢測技術之比較

A Comparison Between Different Examination Techniques for Impact, Torsional and Adhesive Joint

Failures in Polymeric Composite Materials

單秋成*　　　　　　何彥儒*　　　　　　楊仕偉*　　　　　　鄭錦榮**

Shin, Chow-Shing　　　He, Yan-Ru　　　Yang, Shi-Wei　　　Cheng, Jinn-Rong

~96 年度研究計畫論文~

摘要

　　風力發電是眾多再生式能源中優先的選擇。風機安裝在海邊，面臨各種嚴酷的環境，葉片可能受到鳥類，冰雹或其他異物撞擊，也受到各種劣化作用，膠合接頭處可能產生局部脫層，這些損傷在表面無法以肉眼看出，但材料的完整性已有所減損，這些早期的微損傷可成為進一步破壞之誘導因數，在長期受循環負載的作用下，可能造成突發且災難性的破壞！在損傷大幅發展以前，如能對這些內部缺陷或破壞及早發現，對於提高風力機組使用的安全性及堪用率相當重要。

　　本研究針對非破壞檢查葉片內部缺陷/破壞的較為可行的超音波及 X 光技術，比較其在檢測包括衝擊破壞，扭轉破壞及膠合處破壞的檢測方法及能力，以供作為對風機葉片定期檢查的重點及程序的訂立所參考。

Abstract

　　If natural resources allowed, wind power might be the most competitive of different renewable energy options.

　　Wind turbine blades are subjected to cyclic loading due to gravity, vibration and variation of wind loads. Turbines are installed along the coast and face harsh environmental attack such as extreme temperature, solar radiation, hailstorm, snow and bird strike. These may cause small internal damages. Under the action of the above named cyclic loading, these minor internal damages may develop into large structural defects and eventually cause catastrophic failure of the blades. The current project compared different non-destructive examination techniques with the aim of establishing useful inspection guideline and procedures for the wind turbine blades. Ultrasonic and X-ray radiography techniques will be looked into detail in their capability of revealing and monitoring internal damage caused by impact, torsion and adhesive failures.

壹、前言

再生能源中，風力發電是較具成本競爭力。風機的能量輸出，與葉片的長度的平方成正比，所以不同的製造商，均盡量在結構安全性容許的範圍內增加葉片的長度，從上世紀80年代的5公尺到今天的50公尺以上。然而，葉片的重量基本與葉片的長度的三次方成正比，葉片越長，其旋轉時的重力變動量、重力所造成的彎矩、離心力以及振動也越大；另一方面，在相同轉速下其靠近末端的線速度也因長度增加而變高，一旦受到異物撞擊如鳥擊，其損傷的可能性也越高。

丹麥統計2001年第四季風機組件破壞的情形「1」，葉片破壞所佔的件數比例雖不高，但所引起維修或更換的成本卻相當可觀，因此如何預防，監測，檢測以避免風機葉片意外破壞對於降低風力發電的成本有很大的幫助。

除了上述各種引起葉片疲勞破壞的直接施力因素外，尚有很多間接的環境因素會導致或加速葉片的破壞：風機很多時是安裝在海邊或甚至在海上，面臨各種嚴酷的環境諸如日曬雨淋，早晚與冬夏季極端溫度的變化，鹽霧，高濕度，異物撞擊如鳥擊、下雪或冰雹的撞擊，雷殛等損傷「2-5」。

因為風機葉片趨向大型化，為了降低重量以及製造與運輸成本，大型風機葉片主要採用高分子基複合材料製造，在使用過程中，如前所述，複材葉片受到各種環境劣化因素與反覆作用力破壞的作用，這些作用的結果可能在表面造成明顯的缺陷或裂縫，也可能僅在內部產生表面無法以肉眼看出的缺陷，這些缺陷包括基材裂縫(matrix cracking)，強化纖維斷裂(fiber fracture)，纖維與基材局部脫鍵(debonding)，或三明治結構中複材與填充多孔材間脫鍵，以及層板之間產生脫層 (delamination)的現象，因風機葉片幾何構造的複雜性，除了一般的積層板內部可能出現上述缺陷外，對於不同材料/不同結構接縫膠合之處及積層板層數降低 (ply-drop)之處，也有可能出現膠合失效的情形。這些損傷在開始時可能只是一些細微局部的內部缺陷，但一旦這些微損傷出現，結構的完整性已有所減損；這些早期的微損傷將成為進一步破壞之誘導因數，在前述各種循環負載長期不斷反覆作用下，可以導致損傷大規模擴展，最後造成突發且災難性的破壞！在損傷大幅發展以前，如能在定期維修時即檢測到並對之進行修補，對於提高風力機組使用的安全性及堪用率相當重要，為此掌握適當的非破壞檢查技術顯然相當重要。

本研究的目標，擬比較目前的非破壞檢查技術，瞭解在複合材料結構中，不同之非破壞檢測方法如 X-ray 照相，超音波，以及破壞性顯微觀察對於衝擊，扭力與膠合脫層偵測的優點與侷限，以期為日後發生葉片破壞時，可資依循來進行相關的破損情況分析，以及為日後在維修線上建立或引進大型監測技術能力時，對不同技術的優缺點與取捨提供參考。
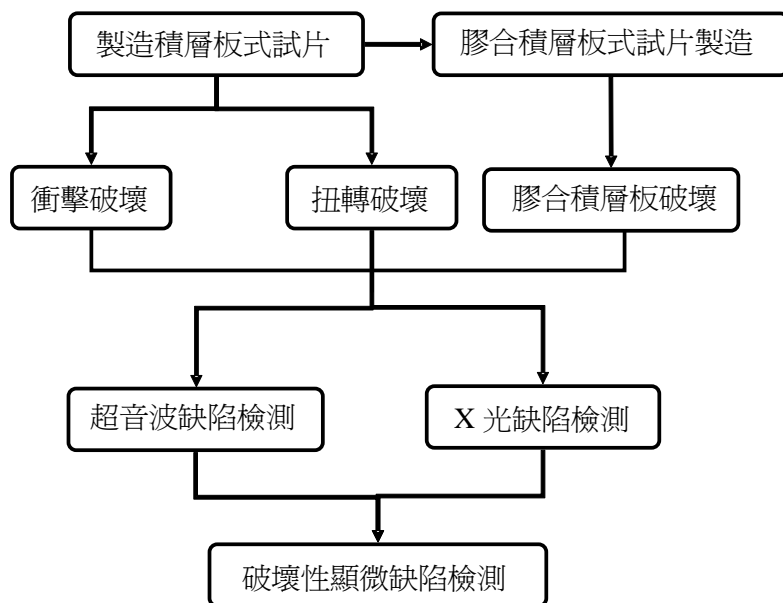
```
┌─────────────────┐      ┌──────────────────┐
│  製造積層板式試片  │─────▶│  膠合積層板式試片製造 │
└─────────────────┘      └──────────────────┘
     │         │                  │
     ▼         ▼                  ▼
┌────────┐ ┌────────┐      ┌──────────────┐
│ 衝擊破壞 │ │ 扭轉破壞 │      │  膠合積層板破壞 │
└────────┘ └────────┘      └──────────────┘
     │         │                  │
     ▼         ▼                  ▼
┌──────────────┐    ┌──────────────┐
│  超音波缺陷檢測  │    │  X 光缺陷檢測   │
└──────────────┘    └──────────────┘
         │              │
         ▼              ▼
      ┌──────────────────┐
      │  破壞性顯微缺陷檢測   │
      └──────────────────┘
```

表1　研究步驟流程。

貳、實驗方法與步驟

風機葉片所採用的材料基本為高分子基複合材料，但如文獻回顧所述，同一葉片上不同部位因結構性能所需，會採用不同疊層、厚度甚至不同材質的複材，因此本研究使用了 8 層之碳纖維/環氧樹脂複合材料及 16 層之玻璃纖維/環氧樹脂複合材料，另有關膠合破壞之檢測，除上述材料外，另從高雄先進複材科技股份有限公司收集到的遊艇船壁結構用玻璃纖維樹脂層板。

破壞測試的主要目的為使用不同破壞方式對複材產生程度不等的內部損傷，再利用利用超音波掃描檢測設備，X 光照相探傷設備與破壞性顯微觀察，來比較不同之非破壞檢測方法對衝擊損傷的檢測能力和其限制。破壞測試包括單純衝擊及衝擊後扭轉，衝擊測試利用依 ASTM-D3029 規範設計的一個落槌衝擊試驗機進行，藉由調整落槌重量與落下高度來控制衝擊能量的大小，衝擊試驗分別使用的 6 種不同高度落下所產生的能量來衝擊試片，碳纖維層板較薄，採落槌重量 70g 以及 40cm 到 140cm 不等的高度，已可造成從幾乎沒有破壞到肉眼都可看到明顯程度不等的破壞，玻璃纖維層板因厚度較厚，經初步測試發現必須採用重量為 110g 的落槌，不同落槌重量與高度所造成的衝擊能量如表 2。

表2　落錘高度與衝擊能量的關係。

落下高度	衝擊能量	
	70g 衝頭，碳纖維複材用	110g 衝頭，玻璃纖維複材用
140cm	0.961J	1.511J
120cm	0.824J	1.294J
100cm	0.687J	1.079J
80cm	0.550J	0.863J
60cm	0.412J	0.647J
40cm	0.274J	0.432J

在衝擊試驗前，先以超音波掃描檢測，觀察是否試片中存在有缺陷並剔除品質較差的試片。

考慮及風機葉片在受到局部衝擊破壞或脫膠破壞後，其運轉時所經受的扭轉施力可能使原

來的局部破壞進一步發展，所以在衝擊破壞後，另進行扭轉破壞。

經破壞的試片，先經過超音波掃描檢測，再進行 X-ray 照相檢測。為使得照相顯影效果更顯著，在 X-ray 拍照前，需先將試片浸泡於碘化鋅 (Zinc Iodine，ZI_2) 溶液中，並放置於超音波震盪機中隔水震盪 20 分鐘，使碘化鋅滲入試片的缺陷處，採用碘化鋅，是由於碘化鋅屬於無機化合物，較其他常用的有機化合物毒性較低，對 X-ray 有良好的吸收能力，在 X-ray 照相時能促使內部缺陷在底片上留下明顯的影像。

破壞性光學顯微檢測利用光學顯微鏡進行觀察之前，先在試片上規劃欲取樣之部分，再以深切緩給鑽石砂輪機切取所需之部分，在予以冷鑲埋處理，將其埋入一高分子基座中，以方便後續的研磨作業，研磨過程與金屬材料金相觀察的準備過程類似。

叁、結果與討論

一、衝擊破壞之檢測

（一）碳纖維複材衝擊破壞之超音波 C-scan 與 X-ray 檢測

碳纖維複材試片衝擊破壞的衝擊高度分兩種：以 140cm、120cm、100cm 為一組，80cm、60cm、40cm 為另一組。

在超音波 C-scan 檢測中，反射回波能量越低，代表內部有介面使超音波散射，顯示有內部破壞的存在。

圖 1 比較以 40cm 至 80cm 高度衝擊前後的超音波 C-Scan 掃描，掃描結果可以很清楚的看到衝擊前後的明顯差異，如衝擊能量在到 0.274J(高度 40cm)以下，超音波掃描便顯示不出

明顯的破壞。圖 2 為同一試片利用 X-ray 照相的檢測結果，衝擊高度為 40cm 之衝擊點於 C-scan 能夠檢查出來，X-ray 卻無法發現，主因應為衝擊裂縫太小，或沒有從外表面連通到破壞層，導致顯影劑難以滲入內部缺陷，無法成像所致。

為以 40~80cm 高度進行衝擊破壞後，試片表面肉眼觀察沒有看到明顯破壞或凹陷的現象，但衝擊高度增加為 100~140cm 時，試片受衝擊之表面出現輕微的凹陷，但在背面則看不到衝擊破壞的痕跡。圖 3 為以 100cm 至 140cm 高度衝擊前後的超音波 C-Scan 掃描，破壞範圍明顯較衝擊高度 40~80cm 者為嚴重，同一試片在 X-Ray 照相的檢測下（圖 4），在辨識衝擊破壞範圍上相對於較低能量的衝擊較為清晰，破壞細節上也增加了不少，除了原本超音波所掃描出來的破壞範圍以外，X-Ray 成像尚具超音波 C-Scan 掃描所沒有的許多細節，這些細節推測可能是基層(matrix)的裂縫破壞，沿 ±45˚與 90˚方向發生的纖維分離(fiber splitting)等，其確實的破壞機制，有待利用破壞性的顯微觀察來加以證實。

破壞範圍有偏向往 45˚方向延伸的傾向，推測為衝擊負載造成的彎曲，使得對彎曲破壞抵抗力較低的 45˚層造成較多的脫層與纖維斷裂破壞。

在衝擊點上會有較高的超音波反射能量出現的情況，X-ray 也顯示落槌的落點處較無破壞的情形，推測為落槌撞擊處的積層較平整且衝擊處複材整體因為衝擊力影響造成層與層之間的密度上升，音波或 X-ray 穿透的情形較其他有脫層的部分理想，因此能量會比破壞延伸的地方還高一些。
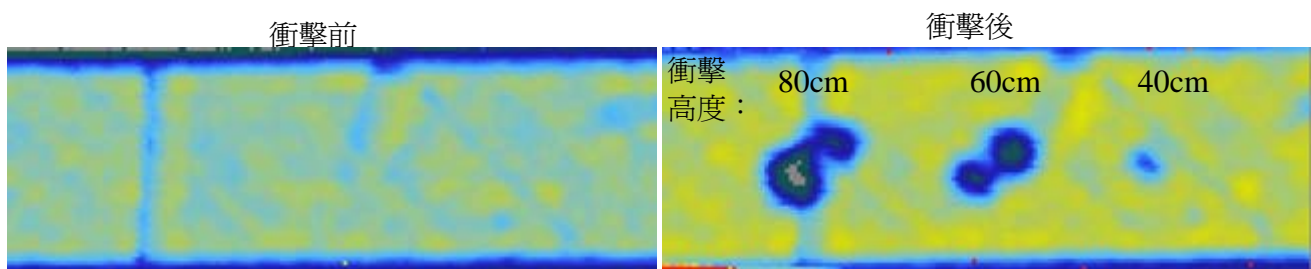
衝擊前

衝擊後

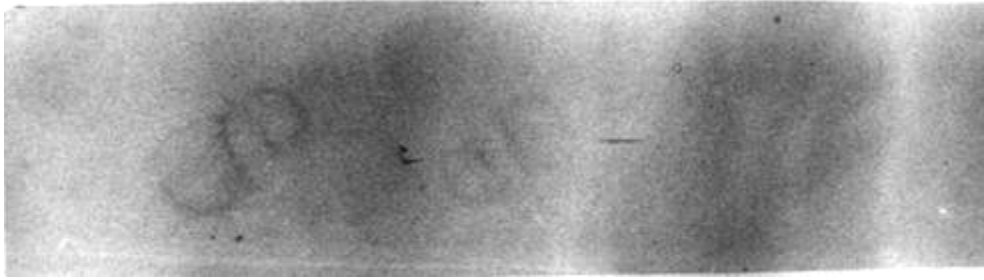圖 1　衝擊高度為 40~80cm 試片之衝擊前後 C-Scan 掃描檢測結果。

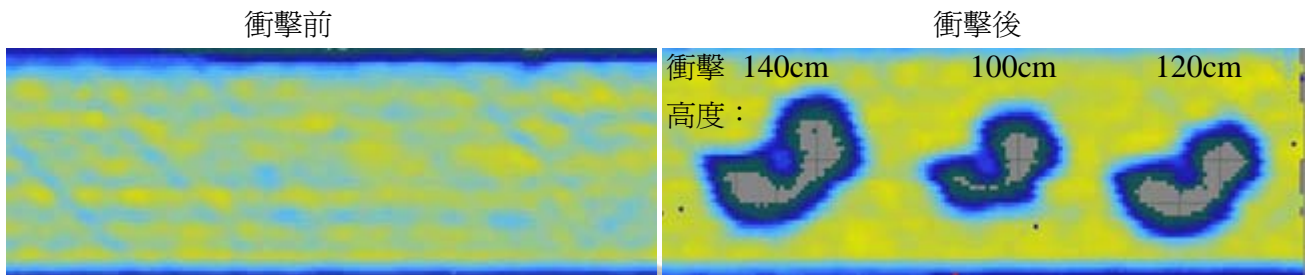圖 2　衝擊高度為 40~80cm 試片之 X-Ray 照相檢測結果。


圖 3　衝擊高度為 100~140cm 之試片衝擊前後 C-Scan 振幅色標圖

圖 4　衝擊高度為 100~140cm 之試片 X-Ray 照相檢測結果。

（二）　碳纖維複材衝擊破壞顯微觀察分析

　　在顯微觀察之前，利用 C-scan 與 X-ray 照相結果來仔細規劃欲裁切之區域與各截面之間的間距，以深切緩給鑽石砂輪機來進行初步裁切，再漸次研磨，過程中小心掌握試片的尺寸，以確保所觀察的位置與 C-scan 或 X-ray 破壞成像的對應。顯微觀察發現不同衝擊高度所造成的內部破壞除程度上的差異外，破壞機制基本類似，以下謹以衝擊高度為 40cm 及 140cm 兩個條件來加以說明。

　　圖 5 為衝擊高度 40cm 破壞的觀察截面 H-H 至 I-I 與 C-scan 破壞顯示區域的位置對應，，圖 6 與 7 分別為兩個截面的光學顯微觀察。截面 H-H(圖 7)在±45°之兩個疊層發生基層(matrix)裂縫破壞(箭頭處)，並在與 90°疊層間有脫層破壞(橢圓處)。截面 I-I(圖 7) 則因位于破壞的邊緣，故僅在背面的疊層中有一些垂直與表面的基材裂縫。
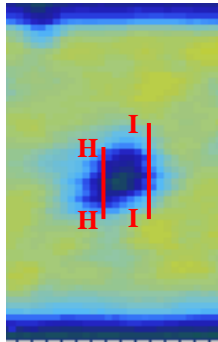
C-scan 成像與各截面長度示意圖

圖 5　非破壞檢測成像與各截面長度示意圖(衝擊高度 40cm)。

砂紙刮痕
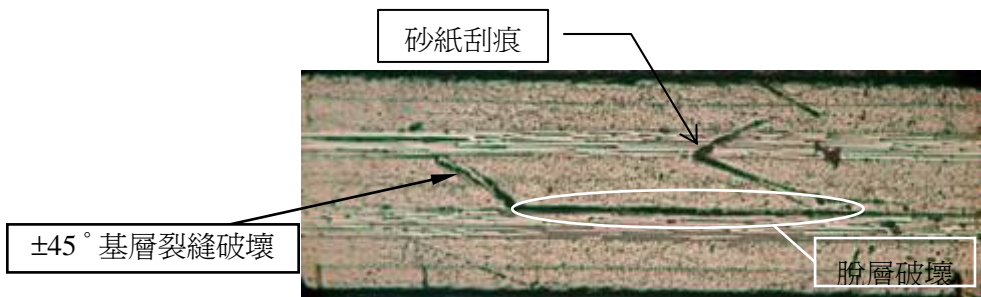
±45°基層裂縫破壞

脫層破壞

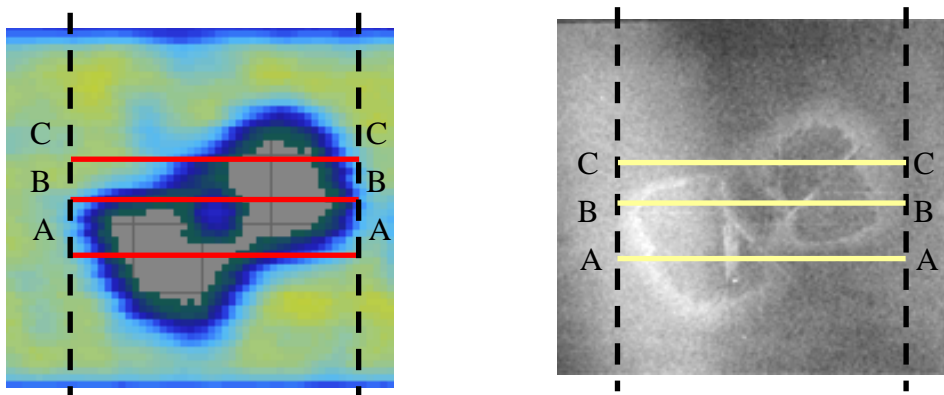圖 6　衝擊高度 40cm 截面 H-H。　　0.6mm

0.6mm

圖 7　衝擊高度 40cm 截面 I-I。

圖 8　衝擊高度 140cm 顯微斷面裁切示意圖。

圖 8 為衝擊高度 140cm 破壞的觀察截面 A-A 至 C-C 與 C-scan 及 X-ray 的破壞顯示區域的位置對應，相較於衝擊較低之衝擊，在脫層破壞中層與層間的距離及脫層破壞規模都嚴重許多，圖 9 中截面 A-A 在串聯不同脫層的基層裂縫破壞之處(圖中圈圈處)，會在 X-ray 的成像中出現較明顯的白色條紋，應為此處的裂縫方向垂直於拍攝的方向之關係，在此顯影劑的含量與厚度也較高，使 X-ray 能量的吸收較明顯所致，此一細節在 C-scan 的檢測是無法辨識的。相同的現象亦出現在圖 10 及 11 兩個截面上。截面 B-B 正好通過衝擊點，圖 11 顯示衝擊點下沒有看到脫層破壞，此與超音波及 X-ray 檢測的顯示吻合。
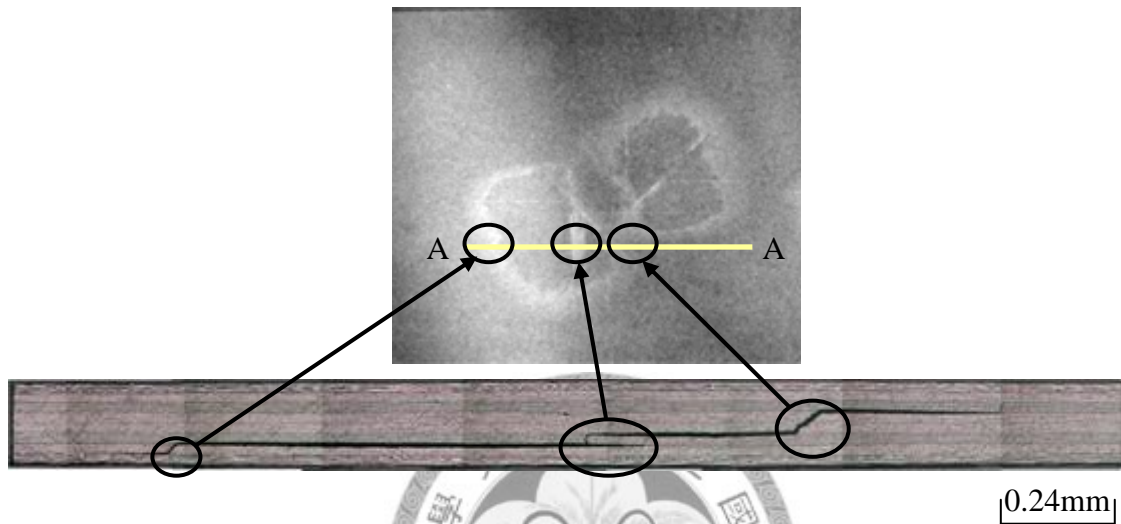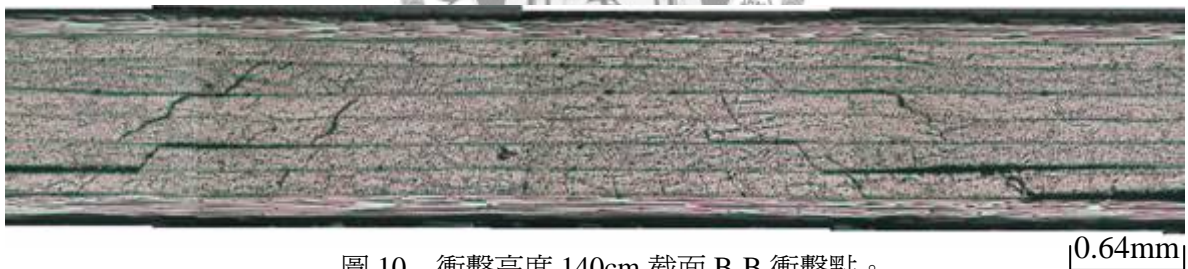

0.24mm

圖 9　衝擊高度 140cm 截面 A-A 破壞機制相對位置圖。
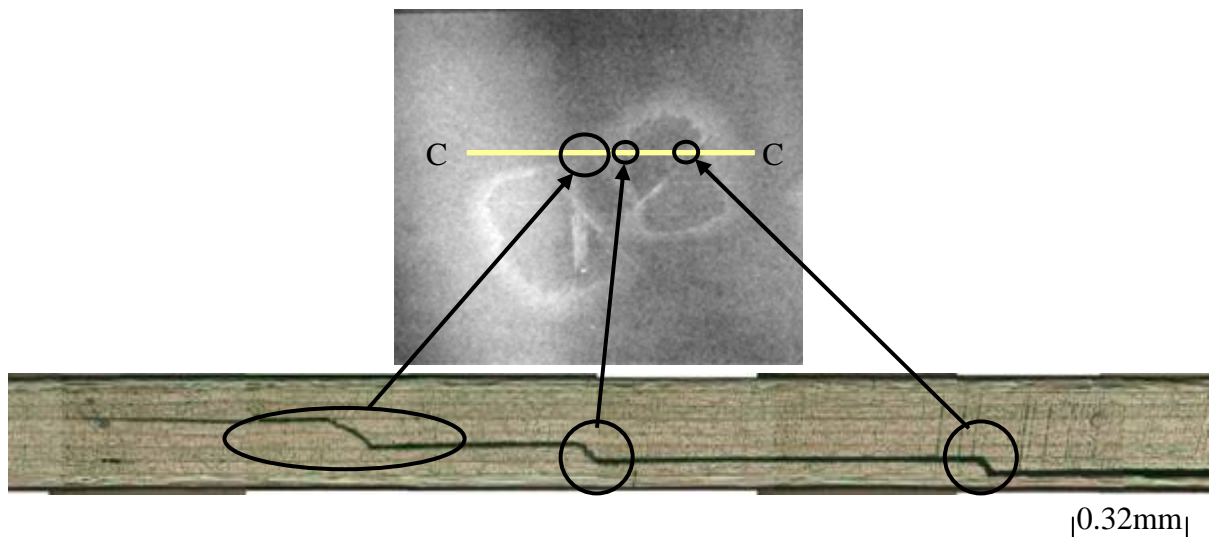

0.64mm

圖 10　衝擊高度 140cm 截面 B-B 衝擊點。

0.32mm

圖 11　衝擊高度 140cm 截面 C-C 破壞機制相對位置圖。

（三）玻纖複材衝擊破壞超音波與 X-ray 檢測

　　圖 12 為衝擊高度 40~80cm 之玻纖複材試片衝擊前後 C-scan 掃描檢測及衝擊後背面照片。衝擊點正面肉眼觀察沒有明顯損傷，但背面則有較明顯的損傷痕跡，但此複材有一定的透明度，所以正面也可隱約看到表面的破壞。衝擊前之 C-scan 掃描圖，明顯可以看到一些 0°, 90°, ±45° 的線條，這些線條為玻璃纖維束。由衝擊前後之 C-scan 掃描圖比較可知，60cm 以及 80cm 的衝擊破壞較容易經由超音波掃描呈現出來，而 40cm 的衝擊破壞幾乎很難觀察到有明顯的能量散失。

　　圖 13 則為衝擊高度 100~140cm 衝擊後背面的照片以及 C-scan 掃描圖，與上一系列衝擊能量較輕的相比，此系列試片的背面可以更清楚看到破壞的痕跡。由試片衝擊前後的 C-scan 掃描檢測比較結果可知，隨著衝擊高度增加衝擊能量增加，試片受到破壞而使超音波掃描時能量的散失越大，故在掃描圖上呈現出較大的破壞範圍。

　　觀察試片上各衝擊點呈現白色之部份，其位置與超音波掃描圖者大致吻合，但範圍則較超音波能量散失之範圍大，故推論衝擊能量雖能使玻璃纖維在肉眼下觀察出破壞痕跡，但還不足以造成內部結構有脫層等較大的破壞缺陷，而使的超音波能夠掃描的出這些些微的破壞缺陷。
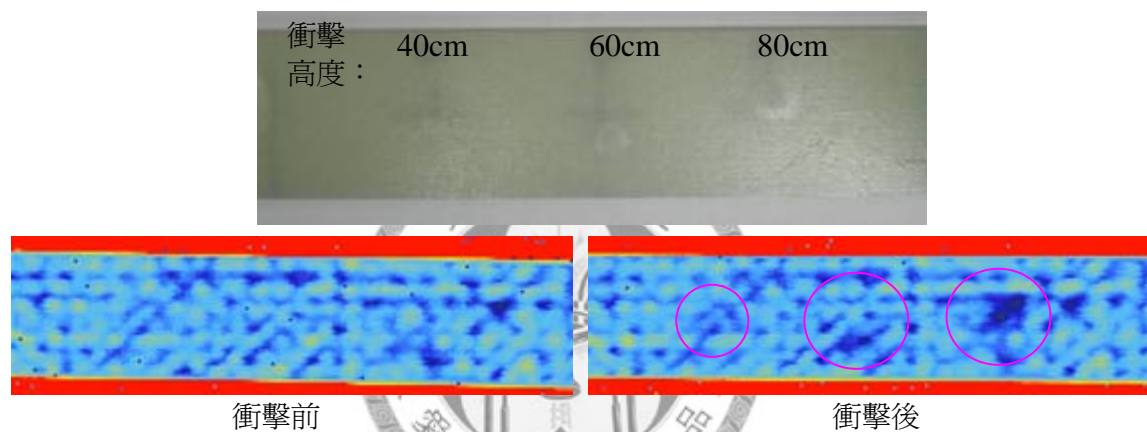

圖 12　衝擊高度為 40~80cm 試片之衝擊前後 C-Scan 掃描檢測結果及衝擊後背面的照片。

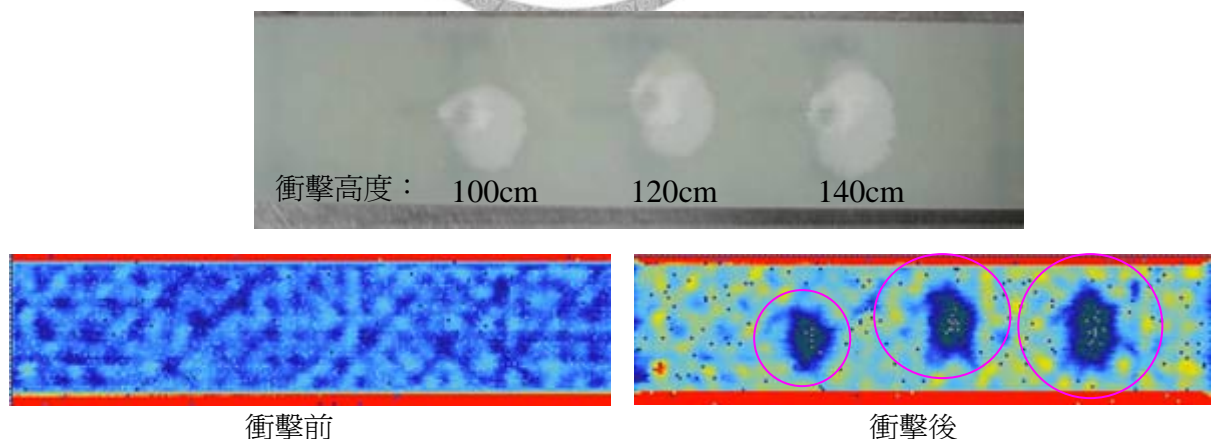
圖 13　衝擊高度為 100~140cm 試片之衝擊前後 C-Scan 掃描檢測結果及衝擊後背面的照片。

　　試片在經過超音波掃描檢測後，先以碘化鋅顯影液滲透處理，之後進行 X-ray 照相檢測，然而檢測結果均未能在 X-ray 底片上分辨到任何破壞的痕跡，推測其原因為試片較厚，衝擊所造成的破壞主要在內部，沒有連通到外表面的裂痕，以致碘化鋅顯影液無法滲透進入缺陷位置所致，另一方面，玻璃纖維束因吸收 X-ray 的能力高於樹脂，所以 X-ray 照片中可以頗為清晰地看

到各種走向的玻璃纖維束。

（四）玻璃纖維複材衝擊破壞性顯微觀察分析

與碳纖維複材一樣，不同衝擊高度所造成的內部破壞除程度上的差異外，破壞機制基本類似，茲以衝擊高度為 40cm 及 120cm 兩個情形來說明玻璃纖維複材衝擊破壞的顯微觀察。圖 14 為衝擊高度 40cm 破壞的觀察截面 A-A 至 C-C 與 C-scan 掃描的位置對應，在此衝擊高度，C-scan 掃描雖未顯示破壞，但顯微觀察則顯示在衝擊範圍內並沒有發現脫層，靠近試片背面處有垂直於試片表面之微小裂縫（見圖 15），微裂縫其數量有限，長度也侷限在最外一層到兩層。這些微裂縫方向，不會導致超音波能量有顯著的散射現

象，又與 X-ray 的方向平行，因此，在超音波檢查及 X-ray 照相中，均沒有明確的破壞顯示。
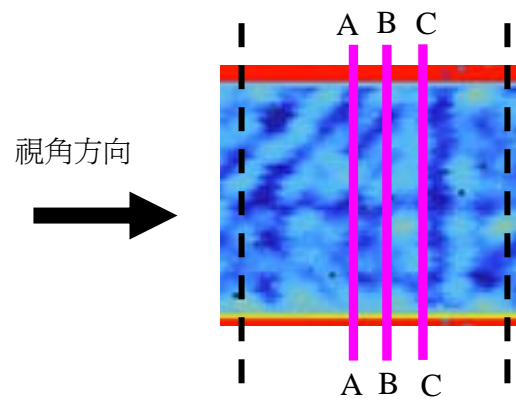

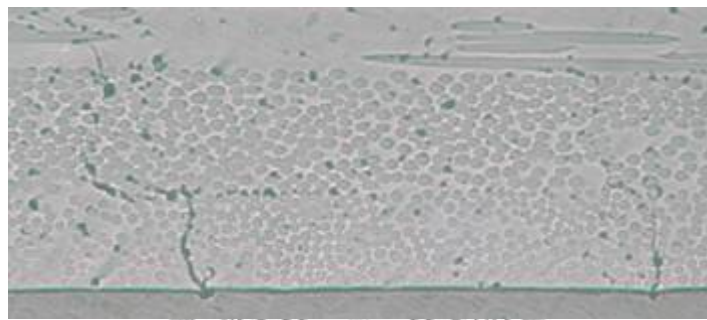圖 14　衝擊高度 40cm 顯微斷面裁切與超音波檢查結果關系示意圖。
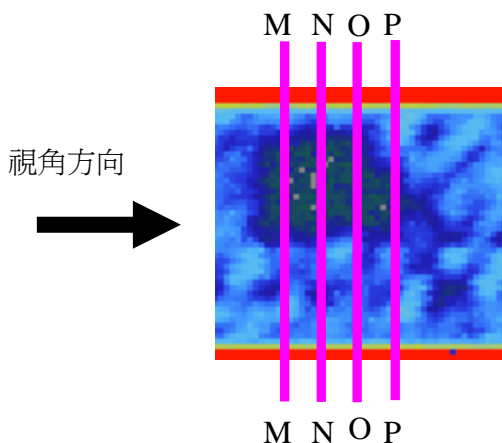

圖 15　衝擊高度 40cm 截面 A-A 至 C-C 底部典型之基材微裂縫。

圖 16　衝擊高度 120cm 顯微斷面裁切與超音波檢查結果關系示意圖。

圖 16 為衝擊高度 120cm 破壞的觀察截面 M-M 至 P-P 與 C-scan 掃描的位置對應，圖 17 至 20 為這些截面的顯微觀察。在較高的衝擊能

量下，脫層的開裂情況有顯著的增加，隨著衝擊能量漸次增加，脫層蔓延的範圍也跟著擴大，不同層間也有同時發展出脫層的情形，而且脫層除沿 90°層介面出現外，也漸次有沿其他層間出現的情況，不同厚度位置的脫層會由穿透層內的基材裂縫串聯起來，即使沒有在串接脫層，內部也有基材裂縫自脫層區域分叉出來的現象，衝擊的背面垂直於表面的微裂縫也廣泛地出現，而且裂縫開口度也較大，背面的微裂縫與從脫層分叉出來的裂縫常沿著纖維與基材的介面發展，不過，即使在衝擊高度 140cm，表面的微裂縫與內部脫層基本沒有連接，因此碘化鋅顯影液無法滲透入內，故 X-ray 照相沒有看到破壞的顯示。
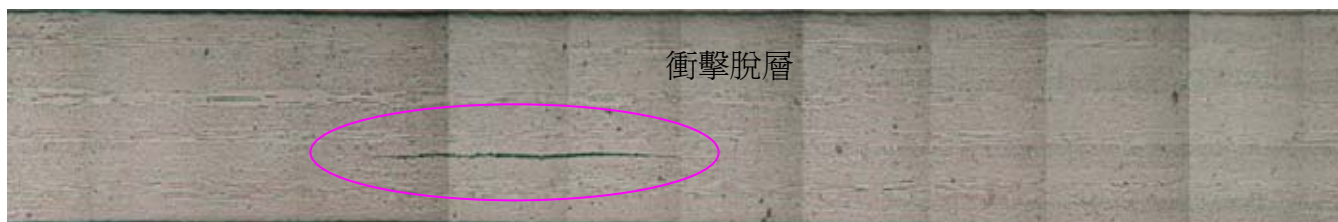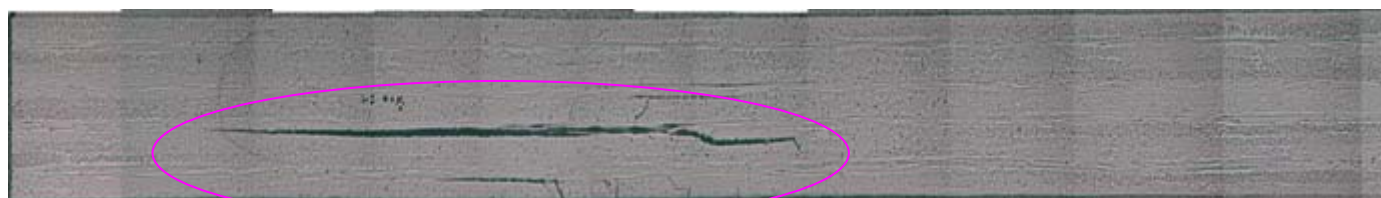
衝擊脫層

圖 17　截面 M-M 顯微金相圖。
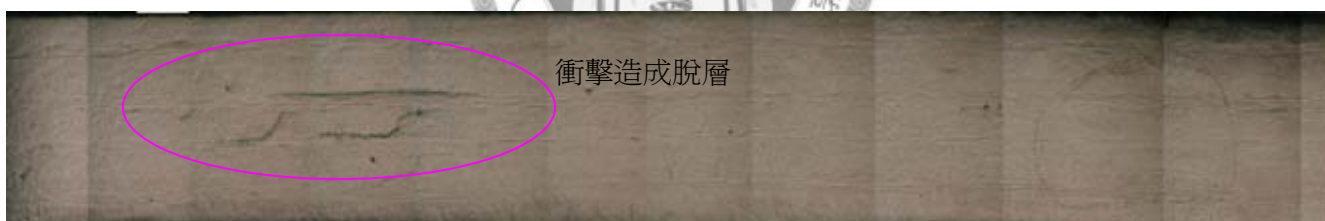

衝擊造成脫層以及底部龜裂

圖 18　截面 N-N 顯微金相圖。
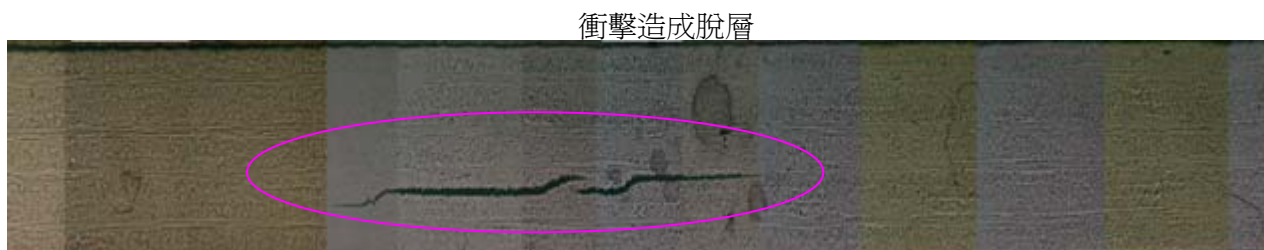

衝擊造成脫層

圖 19　截面 O-O 顯微金相圖。

衝擊造成脫層

圖 20　截面 P-P 顯微金相圖。

綜合上述觀察，光學顯微觀察的操作程序遠較超音波或 X-ray 非破壞檢測複雜，但其對於掌握複材內部破壞機制卻遠較非破壞檢測方法來得具體而精確，非破壞檢測有許多的盲點，如超音波或 X-ray 無法發現平行於音波或光波行進方向的缺陷，X-ray 檢測對於無法將顯影液滲透進內部缺陷時難以成像等，光學顯微觀察皆能有效克服，不過光學顯微觀察為破壞性，而且僅能看到採樣的截面，如採樣位置不對則會有脫漏破壞資訊的問題，因此，也需要其它檢測幫助決定觀察的目標位置。

二、衝擊後扭轉破壞之檢測

（一）碳纖維複材試片衝擊後扭轉破壞之 C-scan 及 X-ray 檢測

此試驗先以衝擊高度 80cm 打擊試片後，再給予扭轉，圖 21 為先以衝擊高度 80cm 的能量做衝擊再施以扭轉破壞的 C-scan 掃瞄比較，在扭轉至 60°時 C-scan 掃描顯示原衝擊點的破壞範圍沒有任何變化，但在扭轉角度增加到 75°~80°時便瞬間斷裂，圖 22 為斷裂試片的背面觀察。

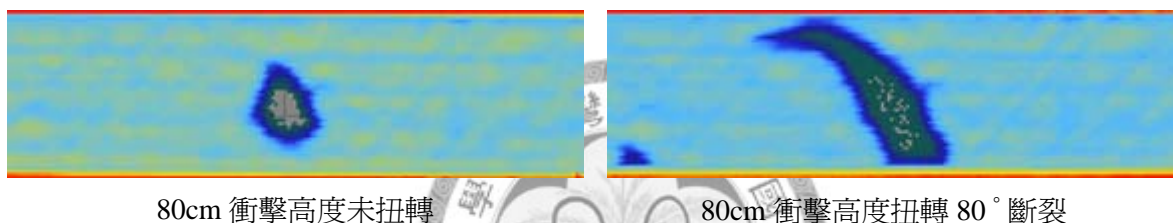80cm 衝擊高度未扭轉　　　　　　　80cm 衝擊高度扭轉 80°斷裂

圖 21　炭纖維複材試片經 80cm 高度衝擊之扭轉破壞前後 C-Scan 掃瞄檢測。

斷裂試片背面扭轉破壞

圖 22　炭纖維複材試片經 80cm 高度衝擊之扭轉破壞後試片表面觀察。

試片在無顯影劑輔助之情況下，依然無法呈現出破壞的情形，而另一方面有加入顯影劑輔助後則有不錯的顯影效果，破壞顯影區域經放大後（圖 23），其中可以清楚的看見較亮的白色條紋為主要的裂縫(表面裂縫)，次要的裂縫(基材裂縫)則為較黯淡白色條紋。
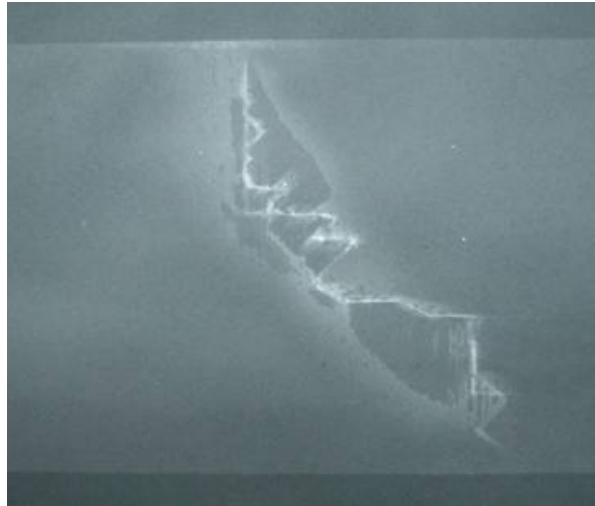
X-ray 檢測所顯示的破壞規模與 C-scan 的相差不遠，但 X-ray 於細節的顯示上依然略勝一籌。

圖 23　炭纖維複材試片經 80cm 高度衝擊之扭轉破壞 X-ray 照相結果。

（二）　碳纖維複材衝擊後施以扭轉破壞之顯微觀察分析

　　衝擊高度 80cm 之扭轉破壞所造成的破壞規模較大，因此估計可以觀察到的裂縫發展模式將會較低能量衝擊的試片明顯，圖 24 為裁切之規劃示意圖，由於破壞範圍較大所以欲觀察之截面分為 A-A（圖 25）與 B-B(圖 26)，A-A 截面由於破壞程度較嚴重以致於裁切試片時便有部分試片剝落，圖 25 的圈圈處顯示出部分試片丟失之情形。

　　圖 25 與圖 26 中可以發現因扭轉所產生之通往表面裂縫其裂縫面皆相當不平整，除此之外其裂縫之發展方向較不規律，可以推測扭轉角度在達到一定程度時，裂縫將會由原本衝擊破壞處迅速地往最靠近的試片表面做延伸。在試片因扭轉角度過大達到極限而破壞時，除了出現大量的表面裂縫以外，試片內部亦可以觀察到平行於截面之疊層受扭轉產生破壞(圖 27 右上角附近)。
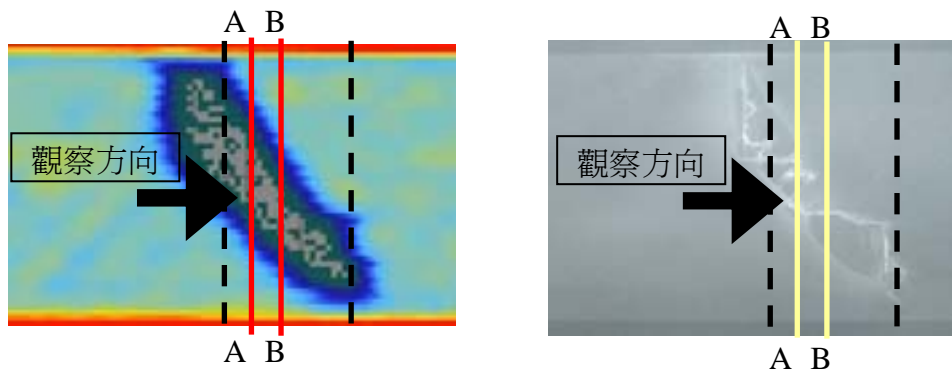

圖 24　炭纖維複材試片經 80cm 高度衝擊之扭轉破壞顯微觀察截面裁切示意圖。

0.4mm

圖 25　炭纖維複材試片經 80cm 高度衝擊之扭轉破壞顯微觀察 A-A 截面。

圖 26　炭纖維複材試片經 80cm 高度衝擊之扭轉破壞顯微觀察 B-B 截面。
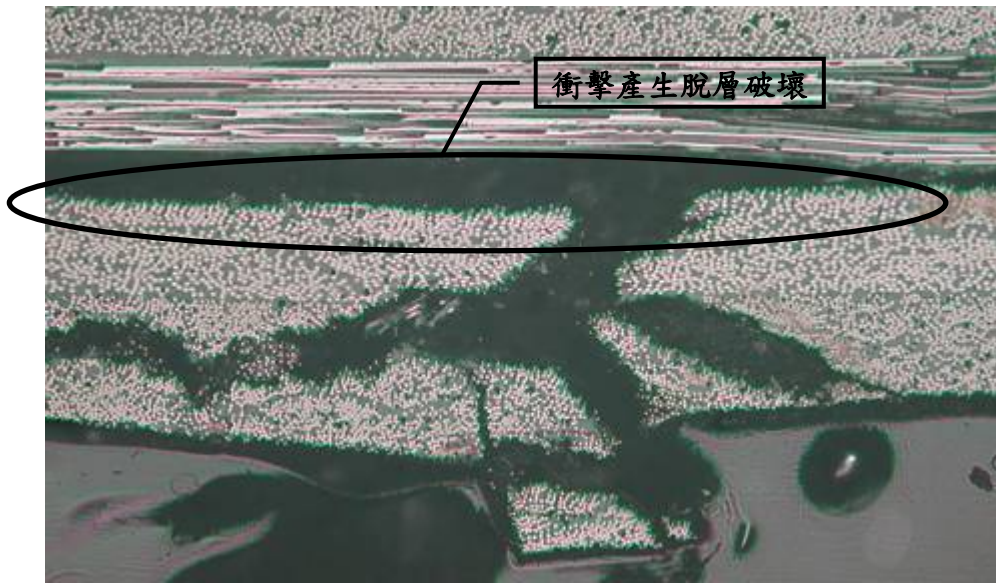
圖 27　炭纖維複材試片經 80cm 高度衝擊之扭轉破壞顯微觀察 A-A 截面右側表面裂縫放大圖。

（三）　玻纖複材衝擊後扭轉破壞之 C-scan 及 X-ray 檢測

　　玻璃纖維複材試片先以 110g 鐵製落槌於 100cm 高度衝擊能量打擊試片後，再分別以 100°、110°、120°各種角度進行扭轉，並以超音波掃描 C-scan 進行檢測。圖 28 為衝擊及扭轉前後的 C-scan 掃描圖，不論 100°、110°、120°之扭轉，衝擊點之缺陷皆沒有顯示出擴大之跡象。當扭轉角超過 120°時，試片開始在夾具夾持部位破壞，另一方面，X-ray 照相亦如衝擊破壞的情形，沒有顯示出破壞的痕跡，推測是衝擊破壞所產生的表面微裂縫在受到扭轉後仍沒有成長至連通到內部破壞，顯影劑無法滲透，故內部缺陷部分仍無法成像。

　　此與碳纖維衝擊後扭轉破壞相較，有相當大的差異，推論是玻璃纖維試片疊層為 16 層較碳纖維 8 層厚度較厚，試片本身結構強度較高，而扭轉本身本來即不容易使試片產生破壞，即使扭轉至試片破壞，亦是從夾具夾持部位受到應力集中處先行破壞。

未破壞

衝擊 100cm
未扭轉

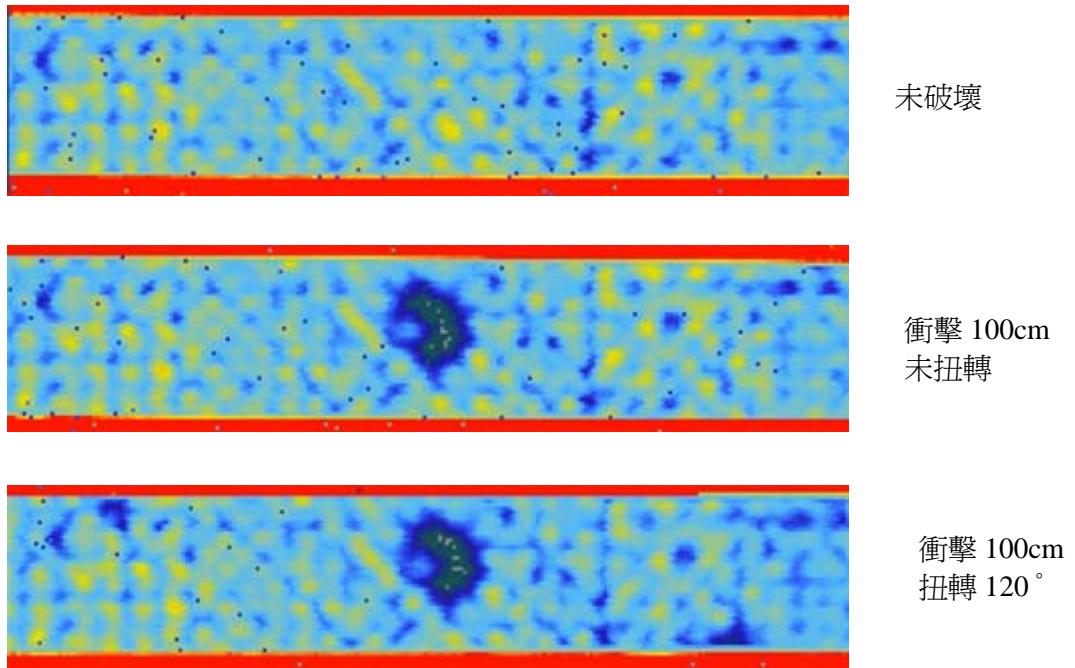衝擊 100cm
扭轉 120˚

圖 28　玻璃纖維複材試片經 100cm 高度衝擊再扭轉 120˚之超音波 C-scan 掃描圖。

一般而言，複材層板抗扭轉破壞的能力相當高，此點從兩種材料的扭轉破壞實驗中皆可清楚看到，對於風機葉片而言，綜合前二章與本章以上的觀察比較，可以推論扭轉對風機葉片比較有可能導致破壞的情形：為層板上有膠合接點，扭轉較有可能會導致脫膠破壞。

（四）玻璃纖維複材衝擊後施以扭轉破壞之顯微觀察分析

圖 29 為玻璃纖維複材試片經 100cm 高度衝擊再扭轉 120˚之顯微觀察截面裁切示意圖發，

其中 F-F 為落錘衝擊點，G-G 為落槌衝擊點附近所產生之缺陷，圖 30 及圖 31 為此二截面的觀察結果。

C-scan 檢查顯示在衝擊後，扭轉前或扭轉後的破壞範圍沒有明顯變化的情形，但如觀察本試驗各剖面，則可發現內部脫層裂縫的情形較純粹衝擊之裂縫為嚴重，不過脫層裂縫主要在往上下疊層發展，以致超音波 C-scan 看到的破壞範圍沒有擴大，此一結果，也凸顯出破壞性的顯微觀察較非破壞檢測優越的地方。
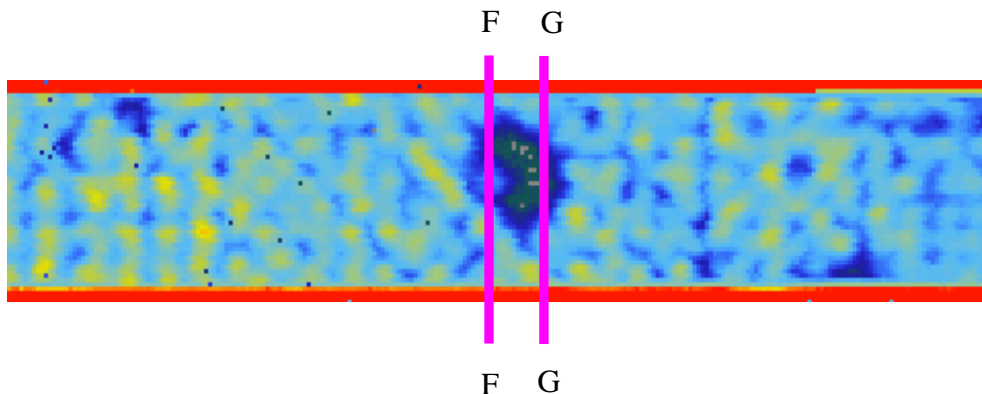
F　G

F　G

圖 29　玻璃纖維複材試片經 100cm 高度衝擊再扭轉 120˚顯微斷面裁切位置示意圖。
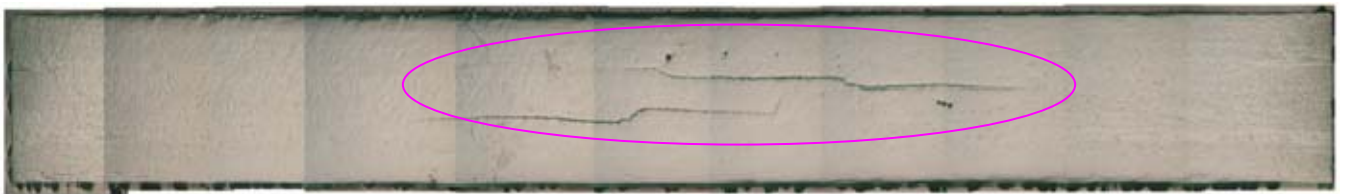
衝擊脫層破壞

圖 30　截面 F-F 顯微觀察圖。

衝擊脫層破壞

圖 31　截面 G-G 顯微觀察圖。

三、膠合破壞之檢測

　　膠合破壞利用從先進科技收集到的遊艇船壁結構的玻璃纖維複材層板試片進行，則因收集到的搭接黏合試片很多已經彎曲或拉伸測試而致非常明顯的局部脫膠破壞，其脫膠的情形與風機葉片可能發生脫膠的狀況應有頗高的相似度，因此我們就直接利用這些破壞。玻璃纖維強化複合材料在超音波檢測方面，由於成型硬化條件較差，疊層分佈較不均勻且試片表面不平整，導致超音波打入試片時會被其不平整的疊層界面給散射開來，因此難以利用超音波檢測的方式來檢測其內部結構損壞情況。

　　圖 32 為脫膠試片正面與側面 X-Ray 成像與試片外觀，此次試驗中皆不加入碘化鋅作為顯影劑，圖右方可以發現，膠合破壞可直接觀察得到，但 X-ray 若由垂直試片表面的方向拍照，卻無法得到任何與膠合破壞相關之資訊，若由試片側面以 X-ray 照相檢測則會有較佳的效果(圖 32 左下)，因此，在利用 X-ray 照相檢查風機葉片脫膠情形時，建議應採用不同角度拍攝，以利增加其偵測/解讀的可能性。

　　另考慮到風機葉片結構脫膠可能發生在內部，外面還有複材層板遮蓋，所以此部分檢查，也利用了厚薄不同的遮罩來比較 X-ray 照相檢測的差異，較薄的碳纖維強化複合材料遮罩板，疊層材料為 T300/3501 x 4，疊層方向為 [0/45/90/-45]2S，厚度約為 1mm；另一塊為較厚的玻璃纖維強化複合材料遮罩板，疊層材料為 DBLT1900 x 6，厚度約為 10mm 遮罩距離也有較遠的 300mm 與較短的 10mm 兩種參數，結果各種遮罩的情形，均不影響試片側面 X-ray 照相明確顯示脫膠破壞。
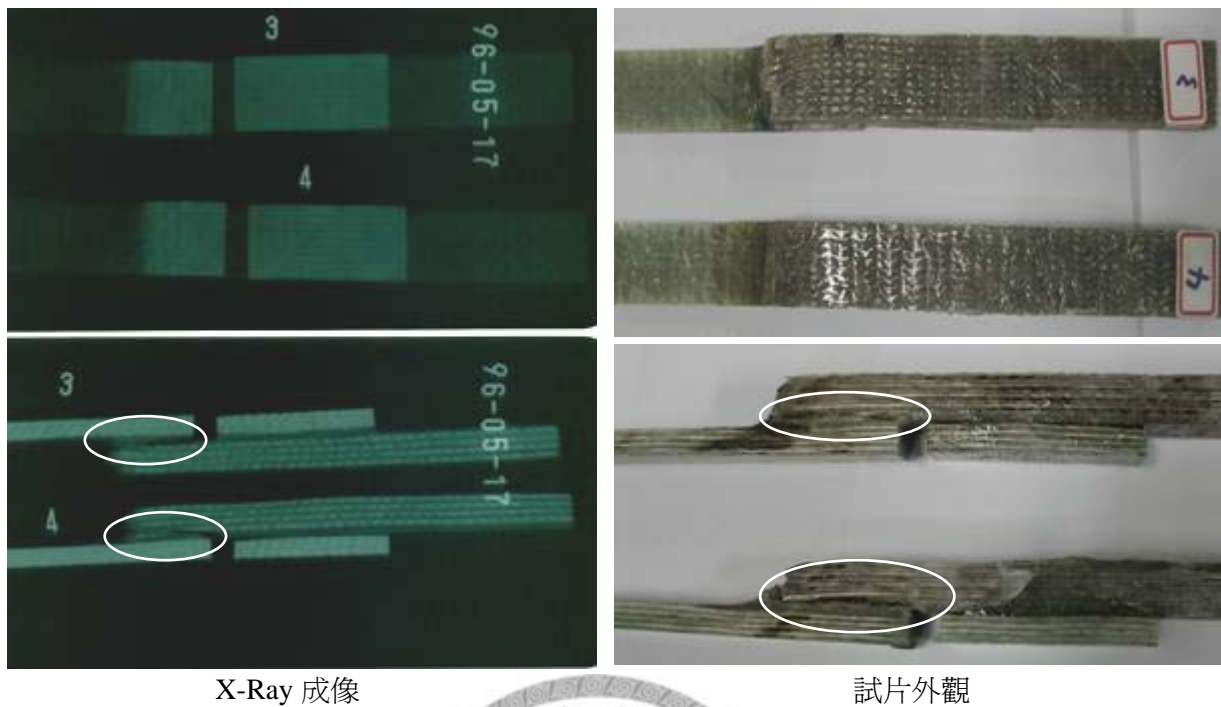
140

| X-Ray 成像 | 試片外觀 |

圖 32　膠合破壞試片正面與側面 X-Ray 成像與試片外觀。

肆、結論

　　本研究利用碳纖維環氧樹脂複合材料積層板，玻璃纖維/環氧樹脂複合材料積層板，以及向一家遊艇製造廠收集到的遊艇結構用玻璃纖維樹脂層板複材來模擬風力機組葉片的衝擊破壞、衝擊-扭轉破壞與膠合破壞，並以超音波檢測與 X-ray 照相檢測配合破壞性光學顯微檢測進行檢驗的工作，由前述的實驗可獲得以下結論：

一、衝擊破壞檢測

　　超音波檢測與 X-ray 在檢測衝擊破壞之範圍的能力相若，但 X-ray 照相檢測對於寬度較狹小的缺陷，若無顯影劑的輔助便會造成成像效果不佳甚至觀察不到缺陷的情況發生；而超音波檢測則是需要較均勻厚實的材質方可傳遞音波，遭遇到內部緻密度不佳，或是多孔的材質時，音波的反射便會變的微弱甚至消失，無法成功檢測。

　　在顯示衝擊破壞上，如能成功滲入顯影劑，

X-ray 可提供較多有關破壞機制的細節，可以簡單判斷出較為嚴重的基層裂縫與脫層範圍較寬與較窄的區域。但如缺陷較小，或沒有表面裂縫聯通到缺陷位置，使顯影劑無法滲入缺陷區域，將會相當難以判斷出缺陷所在與規模。

　　衝擊破壞造成的複材損傷大多為基層裂縫破壞與脫層破壞，由於試驗用複合材料厚度較薄的關係，受到衝擊時所造成的彎曲(bending)應力，因此這兩種主要損傷模式皆集中於衝擊點背面的幾個疊層。

　　藉由光學顯微觀察可以證實顯示於 X-ray 底片上的各方向的條紋所代表的破壞機制，C-scan 便無法判別其缺陷內部有何種破壞機制。

二、衝擊後扭轉破壞檢測

　　衝擊後再扭轉，試片會產生進一步破壞，但這些進一步破壞開始時往往發生在原來的衝擊脫層下面，所以超音波往往無法檢測，如試片抗扭轉能力不夠高，則在瀕臨最終破壞時，原來衝擊破壞有蔓延的趨勢，此時超音波則可以輕易檢

出，但以本計劃中玻璃纖維複材層板為例，因厚度足夠，結果在試片夾持處引起扭轉斷裂時，原衝擊破壞的範圍仍未在試片平面方向蔓延，則超音波無法檢出。

於扭轉破壞上，如顯影液能滲入內部缺陷，則 X-ray 所顯示的細節依然多於 C-scan。

三、膠合破壞檢測

對於材料較厚，材質不夠緻密/平整，又或相關的脫膠位置在其它層板/結構的後面，則超音波 C-scan 派不上用場，而 X-ray 照相會比較適合。

如脫膠接點沒有通道可供顯影液滲透進去，而脫膠接點的開口度有相當的大小，則照相 X-ray 的入射角平行於脫膠面，則脫膠的開口度可以被明確的呈現。因此，在利用 X-ray 照相檢查風機葉片脫膠情形時，建議應採用不同角度拍攝，以利增加其偵測/解讀的可能性。

在上述 X-ray 照相檢測中，外層複合材料的障蔽不會妨礙檢測。

伍、致謝

陸、參考文獻

[1]　Paul Veers, "Research Directions in Wind Turbine Blades: Materials and Fatigue,"　Wind Energy Technology Department, Sandia National Laboratories, http://gcep.stanford.edu/pdfs/energy_workshops_04_04/wind_veers.pdf.

[2]　C. W. Kensche, "Fatigue of composites for wind turbines," Third International Conference on Fatigue of Composites, 13 – 15 September, 2004, Kyoto, Japan.

[3]　M. Megnis, P. Brøndsted, "Life predictions of long fiber composites in extreme environmental conditions using damage evolution approach," Proceedings 11. European conference on composite materials (ECCM-11), Rhodes (GR), 31 May - 3 Jun 2004. (European Society for Composite Materials, London, 2004)

[4]　M. Megnis, P. Brondsted, K. P. Eriksen, "Effects of extreme conditions on properties of the reference material," OPTIMAT BLADES, OB_TG3_R015 rev. 002, http://www.kc-wmc.nl/optimat_blades/public_docs/10167_002.pdf

[5]　M. Megnis, P. Brondsted, L. P. Mikkelsen, "Damage evolution in laminated composite materials," Materialeopførsel og skadesanalyse. Dansk Metallurgisk Selskabs vintermøde, Kolding (DK), 7-9 Jan, 2004. Somers, M.A.J. (eds.), (DMS, Lyngby, 2004) p. 33-42. http://www.kc-wmc.nl/optimat_blades/public_docs/10247_000.pdf